

Computational Modeling

of

Steady, Compressible, Viscous Flow

for

The F-16XL Fighter Aircraft

by Justin Whitt

Departmental Honors Thesis

The University of Tennessee at Chattanooga

Department of Mechanical Engineering

Computational Modeling
of
Steady, Compressible, Viscous Flow
for
The F-16XL Fighter Aircraft

by Justin Whitt

Project Director: James Hiestand, PhD.

Examination Date: November 05, 2006

Examining Committee Members:

James Hiestand, PhD.

Michael H. Jones, PhD., P.E.

Steve Karman, PhD.

Stephen W. Kuhn, PhD.

Examining Committee Signatures:

Project Director

Department Examiner

Department Examiner

Liaison, Departmental Honors Committee

Chairperson, University Departmental Honors Committee

Summary

The purpose of this study is to examine the viscous, compressible flow over the F-16 XL fighter aircraft through the use of computer modeling and to compare the modeled results to experimental results obtained by the National Aeronautics and Space Administration (NASA) during test flights.

This paper outlines the development of a computational model through creation of a finite computational domain, segmentation of this domain into discrete intervals, application of a solution algorithm to determine fluid properties throughout the domain, and interpretation of the resulting data.

These data are then compared to those obtained empirically by NASA during the test flights. This study examines three distinct test flights (two subsonic flights and one transonic flight).

The data obtained from the computational model show very good overall agreement with that obtained experimentally. The model proved slightly deficient in predicting the minimum pressures experienced by the aircraft during actual flight, but reasonably predicted the maximum pressures. The variance between the

experimental and model data for the subsonic cases is thought to be primarily due to the lack of mesh resolution, which allows premature dissipation of vortices in these regions. While mesh coarseness again contributes to the variance for the transonic case, the absence of leading edge deflectors used for stability in the test flights is also a contributing factor.

Acknowledgments

This research would not have been possible without the inexhaustible patience and subject knowledge provided by Dr. Steve Karman and Brent Mitchell; both of whom tirelessly answered a seemingly endless string of questions and provided invaluable understanding. I would also like to thank Dr. Jim Hiestand without whose guidance, experience, and friendship this would have been an even more arduous and daunting process. In addition, I would like to thank all my committee members each of whom has supplied experienced advice at different stages of my academic career as well as having served diligently as the critical review for this work.

Most importantly I would like to thank my beautiful wife, Maggie, for her patience with my distraction and extended absences during this research. You as always have been my team mate, my coach, and my biggest cheerleader, but now I must add anchor. I love you.

For Greta, an ember from my soul and the keeper of my heart...

Contents

Summary	i
Acknowledgments.....	ii
Contents.....	iv
List of Tables.....	vi
List of Figures	vii
Nomenclature.....	xii
Prologue.....	xviii
1 .0 Introduction	1
1.1 The Aircraft.....	2
1.2 Methodology	5
2 .0 Computational Modeling.....	11
2.1 Aircraft Geometry File.....	13
2.2 Surface Mesh	15
2.2.1 Structured Meshes.....	18
2.2.2 Unstructured Meshes	21
2.3 Volume Mesh.....	26
2.4 Viscous Layering	29
2.5 Adaptive Meshing.....	34
2.6 Boundary Conditions	41
2.7 Unstructured Solver	44
2.7.1 Governing Equations	44
2.7.2 Finite Volume Method.....	49
2.7.3 User Defined Variables.....	51
2.7.4 Turbulence Modeling.....	55
2.7.5 Parallelization	62
2.8 Post Processing	64
3 .0 Experimental Data.....	65
4 .0 Comparison of Results.....	67

4.1 Flight Condition: 07	69
4.2 Flight Condition: 25	74
4.3 Flight Condition: 70	82
5 .0 Conclusions.....	89

APPENDICES

References	A-1
-------------------------	------------

Additional Figures	B-1
---------------------------------	------------

List of Tables

Table 1: Summary of conditions at the inlet and nozzle faces.....43

Table 2: Summary of flight conditions.....68

List of Figures

Figure 1: F-16XL-1 and F-16XL-2 in test flight.....	3
Figure 2: Design schematic of F-16XL-1.	4
Figure 3: Rubik's cube.	6
Figure 4: Further partitioning of cube.....	6
Figure 5: Structured surface mesh for flat plate.....	7
Figure 6: Cross-sectional cut of computational domain for flat plate.....	8
Figure 7: Unstructured surface mesh for flat plate.....	9
Figure 8: IGES file of F-16XL.....	15
Figure 9: Point distributions on a connector.....	16
Figure 10: Structured domain with equal point spacing.	18
Figure 11: Structured domain with aspect ratios greater than 1.....	19
Figure 12: Skewed structured domain.	20
Figure 13: Skewness in a surface element.....	20
Figure 14: Cross section of wing.....	24
Figure 15: Spanwise view of right wing.....	25
Figure 16: Illustration of point stretching spanwise.....	26

Figure 17: Cross-sectional cut of the volumetric mesh.....	33
Figure 18: Cp versus Distance near wing tip for the original mesh.....	36
Figure 19: Top view of original mesh.....	39
Figure 20: Top view of adapted mesh.....	39
Figure 21: Cp versus Distance near wing tip for the adapted mesh.....	40
Figure 22: Schematic of typical turbofan engine.....	43
Figure 23: Transition to turbulent flow.....	56
Figure 24: Zones of the turbulent boundary layer.....	58
Figure 25: Results from various turbulence models.	61
Figure 26: Pressure port locations along upper wing surface.....	66
Figure 27: Comparison of Cp along varying BL cuts for FC07.....	71
Figure 28: Comparison of Cp along varying FS cuts for FC07.....	72
Figure 29: Visual Representation of Surface Cp for FC07.....	73
Figure 30: Comparison of Cp along varying BL cuts for FC25.....	76
Figure 31: Comparison of Cp along varying FS cuts for FC25.....	79
Figure 32: Visual Representation of Surface Cp for FC25.....	80
Figure 33: Vorticity Magnitude at constant spanwise cuts for FC07.....	81
Figure 34: Vorticity Magnitude at constant spanwise cuts for FC25.....	81

Figure 35: Comparison of Cp along varying BL cuts for FC70.....	84
Figure 36: Comparison of Cp along varying FS cuts for FC70.....	85
Figure 37: Visual Representation of Surface Cp for FC70.....	86
Figure 38: Shock locations for FC70.....	87
Figure 39: Comparison of Cp along BL55 for Flight Case 07.....	B-1
Figure 40: Comparison of Cp along BL70 for Flight Case 07.....	B-2
Figure 41: Comparison of Cp along BL80 for Flight Case 07.....	B-3
Figure 42: Comparison of Cp along BL95 for Flight Case 07.....	B-4
Figure 43: Comparison of Cp along BL153.5 for Flight Case 07.....	B-5
Figure 44: Comparison of Cp along BL184.5 for Flight Case 07.....	B-6
Figure 45: Comparison of Cp along FS300 for Flight Case 07.....	B-7
Figure 46: Comparison of Cp along FS337.5 for Flight Case 07.....	B-8
Figure 47: Comparison of Cp along FS375 for Flight Case 07.....	B-9
Figure 48: Comparison of Cp along FS407.5 for Flight Case 07.....	B-10
Figure 49: Comparison of Cp along FS450 for Flight Case 07.....	B-11
Figure 50: Comparison of Cp along BL55 for Flight Case 25.....	B-12
Figure 51: Comparison of Cp along BL70 for Flight Case 25.....	B-13
Figure 52: Comparison of Cp along BL80 for Flight Case 25.....	B-14

Figure 53: Comparison of Cp along BL95 for Flight Case 25.....	B-15
Figure 54: Comparison of Cp along BL153.5 for Flight Case 25.....	B-16
Figure 55: Comparison of Cp along BL184.5 for Flight Case 25.....	B-17
Figure 56: Comparison of Cp along FS300 for Flight Case 25.....	B-18
Figure 57: Comparison of Cp along FS337.5 for Flight Case 25.....	B-19
Figure 58: Comparison of Cp along FS375 for Flight Case 25.....	B-20
Figure 59: Comparison of Cp along FS407.5 for Flight Case 25.....	B-21
Figure 60: Comparison of Cp along FS450 for Flight Case 25.....	B-22
Figure 61: Comparison of Cp along BL55 for Flight Case 70.....	B-23
Figure 62: Comparison of Cp along BL70 for Flight Case 70.....	B-24
Figure 63: Comparison of Cp along BL80 for Flight Case 70.....	B-25
Figure 64: Comparison of Cp along BL95 for Flight Case 70.....	B-26
Figure 65: Comparison of Cp along BL153.5 for Flight Case 70.....	B-27
Figure 66: Comparison of Cp along BL184.5 for Flight Case 70.....	B-28
Figure 67: Comparison of Cp along FS300 for Flight Case 70.....	B-29
Figure 68: Comparison of Cp along FS337.5 for Flight Case 70.....	B-30
Figure 69: Comparison of Cp along FS375 for Flight Case 70.....	B-31
Figure 70: Comparison of Cp along FS407.5 for Flight Case 70.....	B-32

Figure 71: Comparison of Cp along FS450 for Flight Case 70.....	B-33
Figure 72: Visualization of Surface Cp for Flight Case 07.....	B-34
Figure 73: Visualization of Surface Cp for Flight Case 25.....	B-35
Figure 74: Visualization of Surface Cp for Flight Case 70.....	B-36
Figure 75: Vorticity Magnitude for Flight Case 07.....	B-37
Figure 76: Vorticity Magnitude for Flight Case 25.....	B-38
Figure 77: Location of Shock Formation for Flight Case.....	B-39

Nomenclature

#cpu	Number of Processors to be Employed
#mesh points	Total Number of Mesh Points in the Volumetric Mesh
#volume points	Total Number of Volumetric Mesh Points
#surface points	Total Number of Surface Points
α	Angle of Attack
β	Angle of Side Slip
δ	Thickness of Viscous Sub-Layer
Δm_{sys}	Change In the Amount of Mass Within a System
Δt	Time Step
Δx	Spatial Step
ϵ	Strain
ϵ_a	Axial Strain

ϵ_t	Transverse Strain
ϵ^n	Truncation Error at the Present Time Step
ϵ^{n+1}	Truncation Error at the Future Time Step
γ	Ratio of Specific Heats
ρ	Density
σ	Normal Stress
ν	Poisson's Ratio
BL	Butt Line
CAWAP	Cranked Arrow Wing Aerodynamics Program
CFD	Computational Fluid Dynamics
CFL	Courant, Friedrich, Lewy Number
C_p	Coefficient of Pressure
DNS	Direct Numerical Simulation

E	Young's Modulus
EFD	Experimental Fluid Dynamics
e_T	Total Energy
ETF	Enhanced Tactical Fighter
f	Body Forces
FC	Flight Condition
FS	Fuselage Station
FVM	Finite Volume Method
G	Amplification Factor
HSCT	High Speed Civil Transport
IGES	International Graphics Exchange Specification
L	Length of the Longest Side of Quadrilateral
I	Length of the Shortest Side of Quadrilateral

LES	Large Eddy Simulation
M	Mach Number
m_{IN}	Amount of Mass Entering a System
m_{OUT}	Amount of Mass Leaving a System
n	Vector Normal to the Control Surface
NASA	National Aeronautics and Space Administration
P	Surface Forces
p	Pressure at a Location
p_o	Free Stream Pressure
q	Heat Transfer
R	Radius of Inscribing Circle
r	Radius of Circle Inscribed
RANS	Reynolds Averaged Navier-Stokes

Re	Reynolds Number
SCAMP	Supersonic Cruise and Maneuvering Program
τ_w	Wall Shear
u	Velocity of Fluid
\bar{u}	X-component of velocity
u*	Shear Velocity
u _s	Velocity of a Control Volume
ν	Viscosity
\bar{v}	Y-component of velocity
\bar{w}	Z-component of velocity
X	Characteristic Length
XoC	Distance in X-Direction Divided by Chordlength
y	Distance From the Wall
YoC	Distance in Y-Direction Divided by Chordlength

Prologue

*Big whirls have little whirls,
which feed on their velocity.
Little whirls have lesser whirls,
and so on to viscosity.*

--L.F. Richardson (1925)

1.0 Introduction

The purpose of this study is to examine the viscous, compressible flow over the F-16 XL fighter aircraft through the use of computer modeling and to compare the modeled results to experimental results obtained by the National Aeronautics and Space Administration (NASA) during test flights. The former was accomplished utilizing the extensive computational fluid dynamics (CFD) experience and computational resources of the UT SimCenter at Chattanooga.

The ability to model complex phenomena associated with high speed fluid flow about complex geometries (the geometric shape of surfaces in contact with the fluid) is important. If these types of problems can be modeled accurately, then some prototyping phases may be cut from the design cycle, thereby, greatly shortening the time and cost between inception and production. Prototyping phases are also important for the physical validation of design concepts and will never be eliminated entirely, but can be reduced through the use of CFD. This is particularly important now due to the high fuel prices driving the already expensive cost associated with operating wind tunnels and wave tanks steadily upwards.

The problem of high speed fluid flow over the F-16XL is unique in that it requires a very large computational domain encompassing highly detailed aircraft geometry. Thus, it will serve to test the

limitations of both the hardware and software and is important in validating that the methodologies and tools used are sufficiently robust.

1.1 The Aircraft

The F-16XL began the design process as the F-16 SCAMP (Supersonic Cruise and Maneuvering Program) in the late 1970's at the General Dynamics Fort Worth division (now Lockheed Martin Aeronautics Company). In 1980 after partnering with NASA's Langley Research Center and conducting extensive wind tunnel testing, General Dynamics began to develop the F-16XL. The United States Air Force also became a partner, providing two F-16's for conversion. In March of 1981 the Air Force announced the Enhanced Tactical Fighter (ETF) competition to replace the aging F-111 and to develop a dual role fighter with ground strike capabilities.

The F-16XL's chief competitor was the F-15E designed by McDonnell Douglas. This modified F-15, which eventually became known as the "Strike Eagle", beat the F-16XL in a "fly off" and was awarded the ETF contract.

The two F-16XL's were returned to the Air Force where, after a seven year stint in storage, they were turned over to NASA for use in research probing sonic shock wave characteristics (*Figure 1*).



Figure 1: F-16XL-1 and F-16XL-2 in test flight at Dryden Research Center [2].

Recently the two F-16XLs were used by NASA to investigate supersonic laminar flow induction and most recently employed by the Cranked Arrow Wing Aerodynamics Program (CAWAP) to provide aerodynamic data for the High Speed Civil Transport (HSCT) research program. The former being the source of the test flight data used for this study.

The replacement of the original F-16 wing structure with the “cranked arrow” wing of the F-16XL resulted in doubling the wing size while the use of composites limited the weight gain to 2800 pounds. In addition, the fuselage was lengthened by 54 inches and the tail was canted up 3 degrees (**Figure 2**). The ventral fins were also removed to keep them from striking the pavement during takeoff.

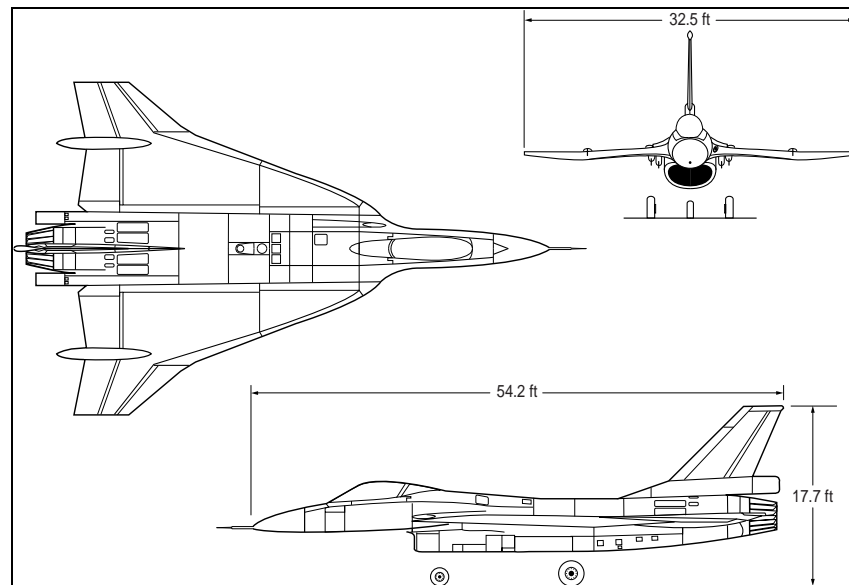


Figure 2: Design schematic of F-16XL-1 [2].

These design changes resulted in greater stability without degrading performance. Additionally these changes resulted in a 25% improvement in the maximum lift-to-drag ratio in supersonic (above the speed of sound) flight and 11% in subsonic (below the speed of sound) flight, smoother

handling at high speeds and low altitudes, an increased fuel capacity, and the ability to carry twice the ordnance of the F-16 while delivering it 40% further [1][2].

1.2 Methodology

The first step in the process of developing a computational model to examine the flow around the F-16XL is to replace the continuous problem domain (i.e., the physical space surrounding the object to be studied) with a discrete computational domain (space segmented into measurable parts). This is accomplished by generating a grid or mesh of points around the aircraft to segment the surrounding space into discrete intervals (a process called discretization).

A simple case is the investigation of air (or any other fluid) flow over a thin rectangular plate. If this plate is enclosed and centered within a box, the top, bottom and sides of the box could be thought of as an outer boundary of the problem.

This creates a cube of some finite volume around the plate.

This cube can then be broken into smaller cubes and visualized as similar in composition to the popular Rubik's Cube (**Figure 3**).

Each of these cubes can be broken into four even smaller cubes (**Figure 4**), and the smaller cubes then further partitioned and so on.

The smallest cubes consist of eight points (one at each corner), and these points serve to discretize, or segment into discrete intervals, the space around the plate. The cubes closest to the surface of the plate would have one side that lay in contact with the plate surface. The cube sides in contact with the surface

make up a "mesh" of squares that cover the surface as if netting had been draped over the plate (**Figure 5**).



Figure 3: Rubik's cube.

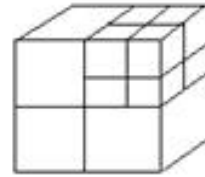


Figure 4: Further partitioning of one cube segment of the above cube.

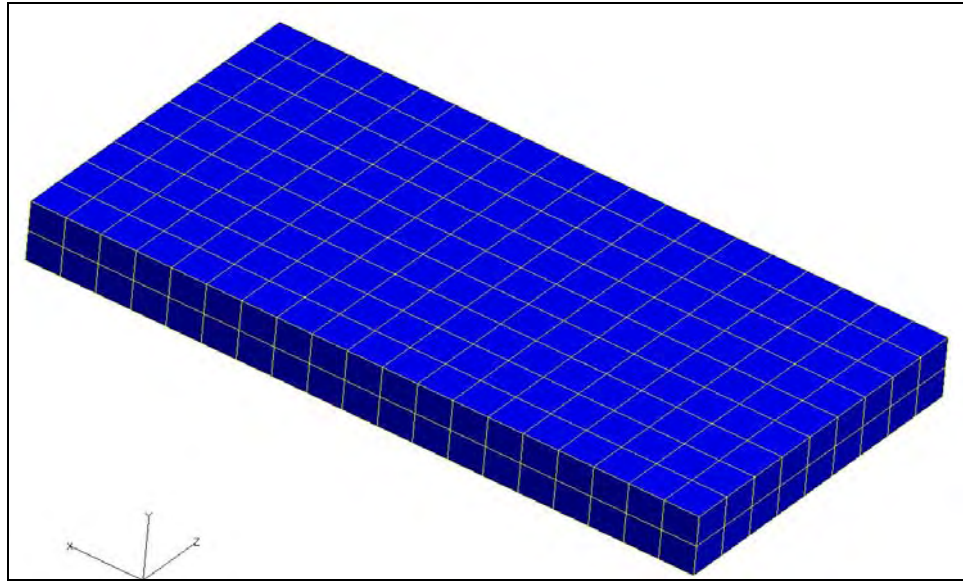


Figure 5: Structured surface mesh covering the plate surface.

This surface mesh of squares now represents the shape of the plate surface for computational purposes. Similarly, the cubes farthest from the surface each have at least one, and as many as three sides (for small cubes that lie in corners), that form the walls of the original outermost cube (the box). This outer box represents the computational boundary of the problem. The surface mesh of squares and the outer boundary serve to close and complete a finite computational volume (**Figure 6**) or domain.

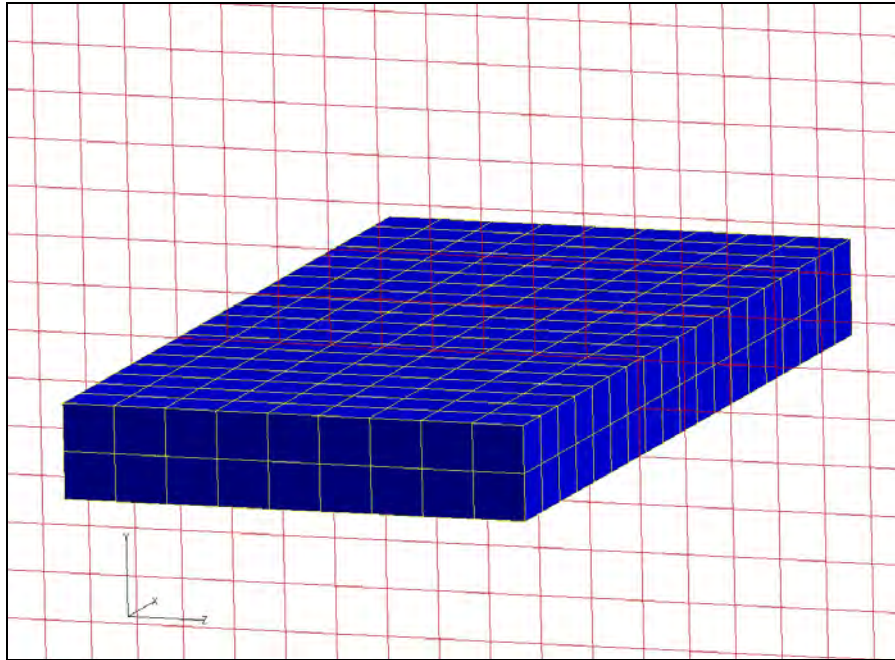


Figure 6: A cross sectional cut of the computational domain for fluid flow over the flat plate.

In reality, the shapes used to discretize are not confined to cubes. Software used to generate these meshes can discretize the surface using quadrilateral (4 sided) shapes as in the structured case above or with triangles (3 sided) for an unstructured surface mesh (**Figure 7**)—the later resulting in a volumetric mesh composed of tetrahedral elements. Each approach has its own advantages as will be discussed later.

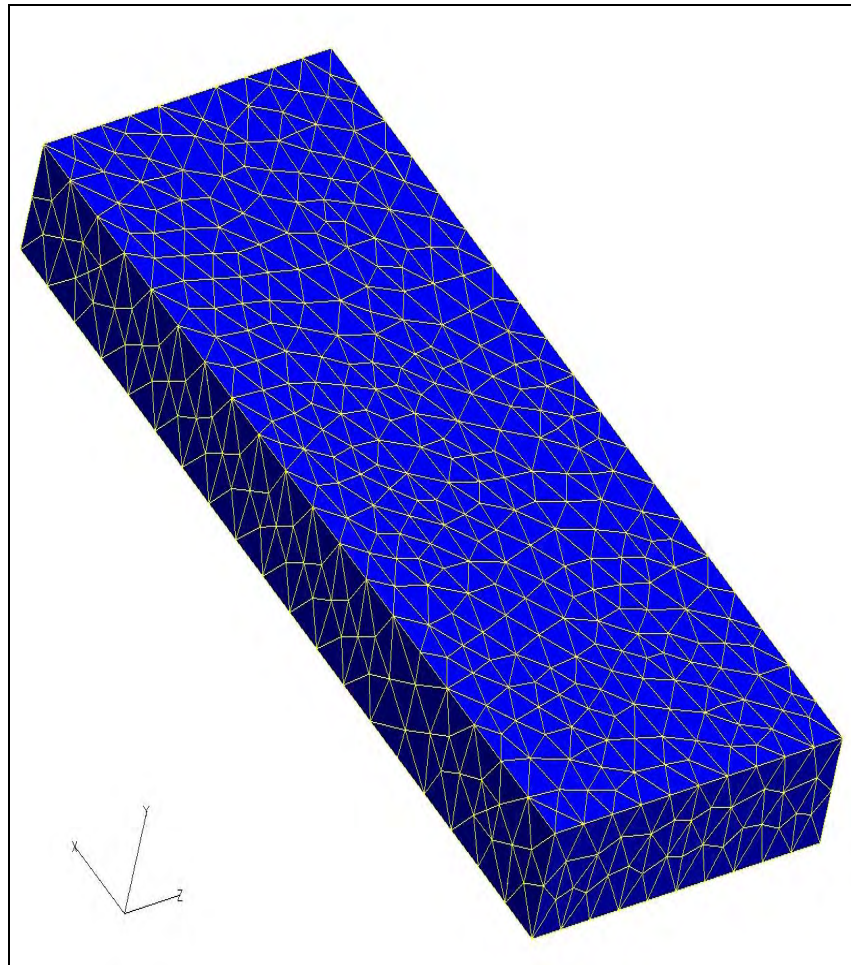


Figure 7: The flat plate discretized with an unstructured mesh of triangles.

For the case of viscous fluid flow over the flat plate above, a very tight spacing would be needed to capture the effects of viscosity near the surface. This fine spacing is commonly referred to as viscous spacing.

Viscosity results from friction between two fluids or between a fluid and a solid. It is similar to the friction between two solids (a resistance to movement due to contact). This necessitates tighter spacing to capture the rapid changes that occur in the fluid at a very small distance from the surface of the plate due to the fluid contact with that surface.

For a few low speed flow cases involving very simple surface geometries, the equations describing the physics of fluid flow over the plate can be solved analytically (exactly) by utilizing methods relating to partial differential and integral-differential equations. For high speeds and more complex geometries the equations become too complicated, and solutions to these equations must be approximated numerically throughout the volumetric mesh of points to allow examination of flow characteristics. This is the primary objective of CFD.

Employing these methods, flow around the aircraft was examined for three sets of unique flight conditions (e.g., three sets of unique values for velocity, angle of attack, angle of sideslip, and fluid properties associated with air).

2.0 Computational Modeling

The computational problem of airflow around the F-16XL aircraft considered in this study is that of a viscous, compressible fluid flow; that is, it considers the “friction like” effects described earlier and takes into account the compressibility or variable density of air.

In general, there are two types of fluids: liquids and gases. Molecules of a liquid, while able to conform to the shape of a container, usually occupy a fixed space or volume. The molecules of a liquid have an essentially constant spacing that only slightly changes in response to changes in temperature or pressure; therefore liquids compress very little and are often assumed incompressible. Water, for instance, is nearly incompressible. This means water cannot be easily squeezed into a smaller space.

Gas molecules in contrast expand to the available space. The spacing between gas molecules is random and easily affected by changes in temperature or pressure. Air, as an example, can be forced into a rubber balloon. The balloon can be squeezed which forces the air into an even smaller space; and when the balloon reaches its elastic limit and bursts, the air expands into a larger container defined by the room. Thus, air is highly compressible as are many gases.

At high speeds (those approaching the speed of sound and termed sonic) air experiences radical

pressure and temperature changes due to the development of shock waves. This means that densities throughout the flow field vary widely and abruptly. Due to these radical changes, fluid energies also vary (specifically the kinetic energies associated with moving fluids) and must be given consideration in this study.

The flow field about the aircraft will be examined at various steady states matching conditions under which experimental flight data were taken. A description of these conditions will be presented with the experimental data in later sections.

The F-16XL computational model will be examined under steady state or time independent conditions.

To understand this concept, consider a garden hose that is attached to a faucet. The faucet is initially in the off position. As the faucet is gradually turned on, visual inspection of the opposite end would show that the flow first begins to trickle and then increases to some full flow. Once reaching full flow the rate of flow leaving the hose remains constant. The time from trickle to a constant flow rate is a non steady period of transients. The time when the flow is at a constant rate is said to be a steady state. The steady state rate of flow is unchanging and therefore independent of time. The flow field around the aircraft will also be examined under steady state conditions.

The process for developing the computational model for the type of fluid flow described above can be broken down into three distinct phases: generation of a discrete volumetric computational domain about a representative surface (a computer generated model of the actual surface), the application of a computational solution algorithm (executed by a computer program) at each point within the domain, and interpretation of the results.

The formation of the discrete computational domain can be further partitioned: generation of the surface mesh, generation of the inviscid volumetric mesh, and insertion of viscous layers within the inviscid volumetric mesh (to capture the friction-like^o effects). In practice this process requires an iterative approach. For instance it may take several attempts to generate the surface and volumetric meshes only to find that they need to be adapted to accommodate the viscous layer insertion. The solution data may also indicate that certain physical phenomena are not being captured by the mesh spacing and require smaller or larger spacing between mesh points within a certain region.

2.1 Aircraft Geometry File

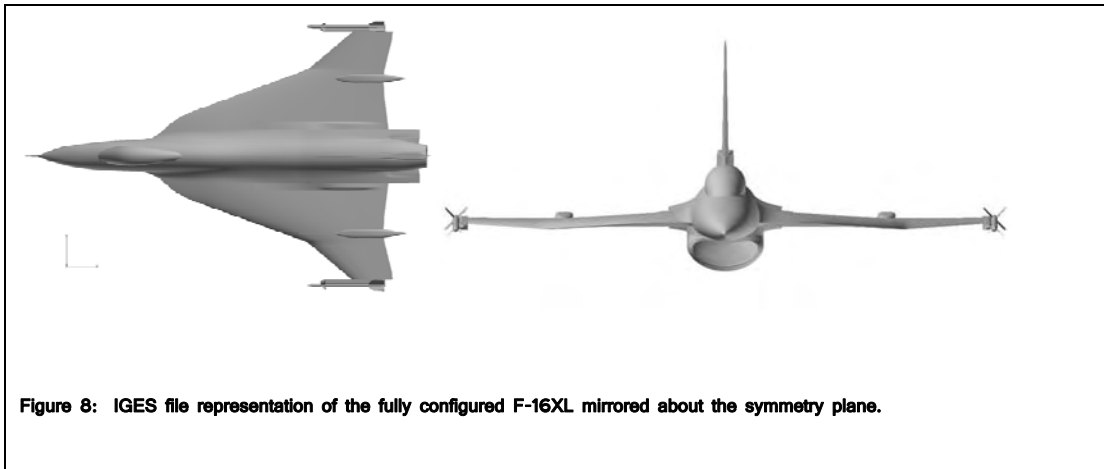
The development of the discrete computational domain begins with a geometry file. This file is a database of points, curves, and surfaces that represent the actual geometric shape of the physical

object about which the fluid flow is to be modeled. The original geometry file for the F16-XL was produced by Lockheed Martin Aeronautics Company (formerly General Dynamics Corporation) as part of the design process. It has been preserved in IGES (International Graphics Exchange Specification) format.

IGES serves as a neutral file format for file exchanges between dissimilar CAD (computer aided design) packages. Because of the aircraft's symmetry, the IGES file only represents $\frac{1}{2}$ the surface of the F-16XL. The half aircraft geometry can be mirrored around a central symmetry plane—bisecting the aircraft from the nose to the vertical tail—to obtain a whole aircraft geometry. This geometry file was compared for consistency by the NASA Langley Research Center with measurements taken using photogrammetry—a method of taking measurements from digital images by measuring the intensity of light received by the camera from the object of interest (See [3] for more information on photogrammetric methods). The upper surface of the geometry file was found to vary no more than 0.002 inch of the actual de-fueled aircraft leveled on jacks [4].

Cleanup work was then performed on the file by the NASA Langley Research Center to repair known inconsistencies (e.g., gaps between adjacent surfaces, etc.) and to prepare the file for mesh generation. The final IGES file contained geometric representations of the following F16-XL

configuration: basic fuselage, tail, and cranked-arrow wing; cockpit canopy; nose air data probe; engine inlet up to compressor face and nozzle aft of the turbine; the actuator pods; the air dam; the wing tip rail and AIM-9 missile; the extended capacity fuel tanks; and the boundary layer diverter (**Figure 8**).

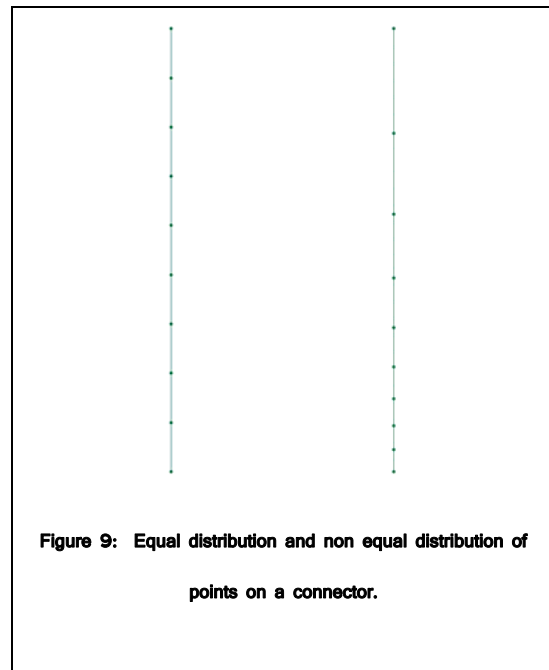


2.2 Surface Mesh

From an accurate and consistent geometry file a surface mesh is generated upon the surface of the half geometry. This mesh generation was performed with the help of a commercial software package called Gridgen [5]. Gridgen segments the surface of the aircraft into regions. These regions, termed domains, are comprised of connectors that can be straight lines or curves and

form a closed boundary containing a mesh of points. These connectors are “dimensioned” with a specified number of points that control the spacing within the domain. Dimensioning refers to the act of allocating a specific number of points to segment the connector into intervals. It is important to note that the spacing between points along a connector does not have to remain constant; in fact, there are many schemes for distributing points along a connector (**Figure 9**).

In general, more points on the connectors lead to tighter spacing within the mesh (more on this later). The mesh domain contains the mesh of points spanning the space enclosed by the connectors. Recalling the flat plate example, each surface of the plate has a separate domain created upon it. These domains are



comprised of straight line connectors forming rectangles with mesh on the interior (**Figure 5**).

Similarly, the surface of the aircraft geometry is subdivided with connectors that are spatially concurrent with the IGES file representation of the aircraft surface. These types of connectors are

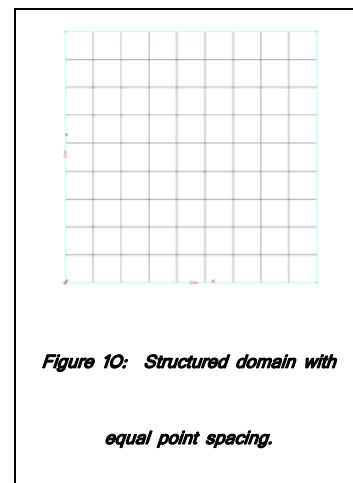
called database connectors because the IGES geometry file (a database of points, curves, and surfaces that represent the aircraft) serves to constrain the possible location and orientation of these connectors. These database connectors always represent the surface of the aircraft and form a series of adjacent domains that are also constrained to the original IGES aircraft surface. These surface domains now represent the computational surface of the aircraft. At this point the IGES file is primarily used to enforce and preserve a spatial concurrence between the surface mesh points and the geometry file representation of the aircraft. It is not part of the computational domain.

2.2.1 Structured Meshes

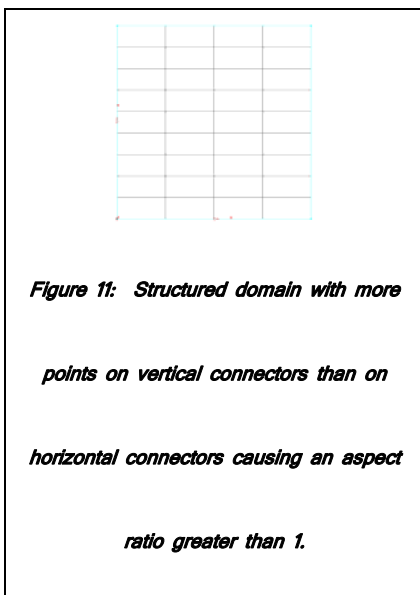
As discussed in the flat plate example, domains can be created as either of two types: structured and unstructured. The primary difference between the two is a matter of connectivity. Structured domains contain meshes that are quadrilateral (4-sided) in nature, and thus, must maintain a one-to-one ratio of the number of points on connectors of opposing sides of the domain. This dictates that structured domains must always have four sides and that the spacing within the domain is tightly controlled by the number of points specified on the confining connectors, that is to say, as the number of points on the connectors grow, the area of each quadrilateral within the domain decreases.

A high quality structured domain contains mesh elements that are perfectly square in an ideal case (*Figure 10*).

Departures from this composition lead to lessening mesh quality within the domain. Consider, for example, a perfectly square domain made up of four connectors of equal length. Recall that the connectors on opposite sides of this square domain must have the same number of



points. If the vertical connectors have 5 points with equal spacing between points and identical spacing on both connectors while the horizontal connectors have 10 points again with equal spacing between points and identical spacing along each connector, the resulting quadrilaterals within the domain mesh will be non-square (rectangles in this case) (*Figure 11*).



is

This cell shape is not necessarily prohibitive.

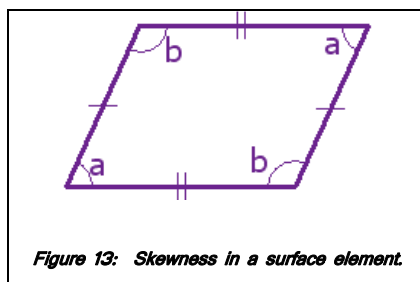
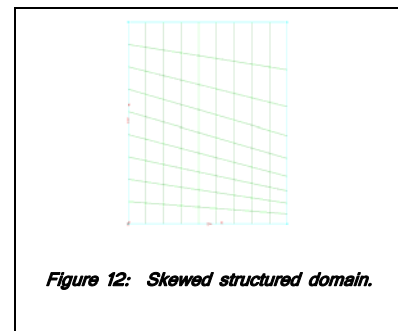
While the quality of a mesh composed of rectangles is less than that composed of squares, there is leeway. The aspect ratio of quadrilaterals defined as the ratio of the length of the longest side (L) to that of its shortest side (l).

$$aspect \cdot ratio = \frac{L}{l} \quad \text{Equation 1}$$

It is generally acceptable (by rule of thumb on a case by case basis) to have rectangles with aspect ratios of up to 5 before seeing detrimental effects, and this stretching may be made even larger in some cases. In fact these non unity aspect ratios can be used as a strategy to reduce the number of points in a mesh by “stretching” the spacing in directions of less interest. The implementation of this strategy will be discussed in detail later.

Another detriment to mesh quality is skewness. Reconsider the square domain above (**Figure 10**). This time let all four connectors have the same number of points. But now allow the spacing between points on the vertical connectors to remain constant while the spacing between points on the horizontal connectors is not constant and varies between each connector. This causes a shearing effect of the elements within the mesh that gives each mesh element the appearance of being squashed (**Figure 12**).

The angles between connectors are no longer all right angles (90°). Two angles are obtuse and have the angular dimension 'b'. Two angles are acute and have the dimension of 'a' (**Figure 13**).



This deviation from 90° alternates from obtuse to acute throughout the mesh in all corners that share a common point and thereby form complementary angles. The mesh is said to be

skewed. This causes problems when orthogonally projecting the quadrilaterals to form volumetric elements. When shearing is extreme, the mesh element can flatten completely

causing a zero volume mesh element. Thus, volumetric fluid properties can not be approximated for the mesh element.

2.2.2 Unstructured Meshes

Unstructured domains within Gridgen are spanned by triangles (**Figure 7**). Any two points on a connector are connected to a third point within the mesh; thus, the one-to-one ratio between sides seen in structured meshes is not preserved. The lack of one-to-one enforcement allows a domain to have any number of sides as long as it is closed (i.e., the point of origin of the first connector is the terminus point of the last connector), and opposing sides of a domain need not have the same number of points. The flexibility allowed by unstructured meshes is very advantageous for applying meshes to complex geometries that require domain shapes other than squares to efficiently subdivide their surfaces, but this loss of structure also results in a loss of control over the spacing within the interior mesh of the domain.

The interior spacing is now controlled by a decay function that is part of the generation process for unstructured domains. The function allows the spacing to progressively grow

away from the connector boundary toward the domain center, resulting in larger triangles in the center of the domain.

A high quality unstructured domain ideally is composed of equilateral triangles. The aspect ratio for triangles is defined as the radius (R) of a circle that inscribes the triangle divided by twice the radius (r) of the circle inscribed by the triangle.

$$aspect \cdot ratio = \frac{R}{2r}$$

Equation 2

Thus, it can be shown that equilateral triangles like squares also have an aspect ratio of 1.

In practice a surprisingly large range of angular dimensions is acceptable for mesh triangles and is best examined case by case.

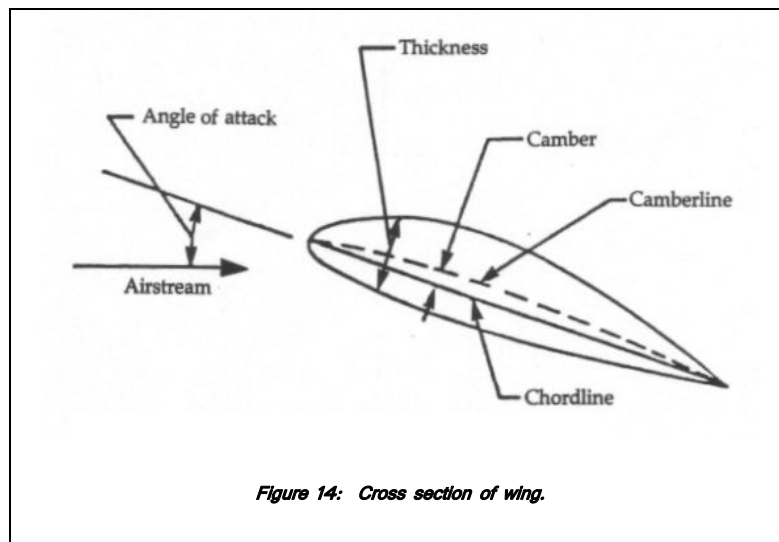
To positively affect the overall mesh quality by enforcing equilateral triangles wherever possible, the spacing between points on adjoining connectors must be equal. This equal spacing does not allow for the stretching of spacing in directions of less interest as with structured meshes. This, coupled with the fact that unstructured domains inherently have

more points than structured meshes, leads to larger volume meshes as a whole which is one disadvantage of unstructured meshes. Also, an extra amount of book-keeping is also involved with storing point locations within unstructured meshes. This is inherent to their lack of structure (i.e., the lack of a definable relationship between mesh points). The larger number of mesh points and additional location information mandate greater computational resources for the use of unstructured meshes, and explain their only recent increase in utility and popularity. Advances in computer technology (storage capacities, data transfer speeds, and computations per second) have changed the computational economy of CFD problems. These advances, coupled with the ease of implementation of unstructured meshes, have made them the mesh of choice.

To continue this discussion of mesh types it is necessary to define several aeronautical terms:

The chord is an imaginary straight line that connects a point on the leading edge (forward most wing surface) to a point on the trailing edge (aft most wing surface). The span is an imaginary straight line that connects a point at one wing tip with a point at the opposite wing tip. Wingspan and chord length are then the lengths of the respective lines while spanwise and chordwise refer to directions that they define.

The final surface mesh created on the F-16XL is a hybrid mesh because it has both structured and unstructured domains. This choice was made to take advantage of the structured mesh ability to tolerate high aspect ratio rectangles and was implemented along the leading and trailing edges of the wing to reduce the number of points (and consequently the demand on computational resources) required to define the wings shape. For illustration, consider a cross-sectional or chordwise cut of a wing—commonly termed a 2-dimensional airfoil (**Figure 14**).



The cross-section shows curvature chordwise from the leading edge. The slope of the curve is greater near the leading edge and lessens as it moves toward the rear of the aircraft. Compare this to a spanwise view of the wing which is very straight for long distances moving

from the fuselage junction to the wingtip (**Figure 15**).

While a straight line can be defined by just two points, it typically takes more points to outline a curve. In fact, the faster the slope is changing along the curve the more points it will likely take

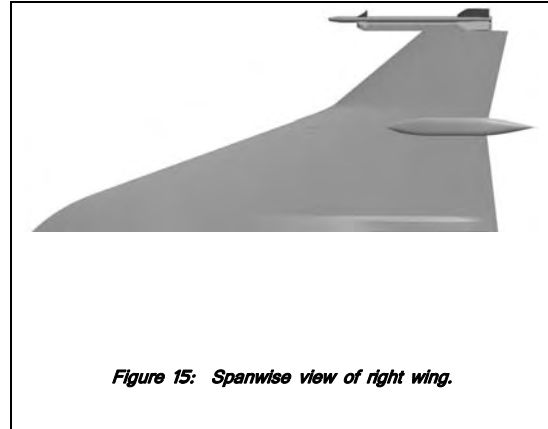
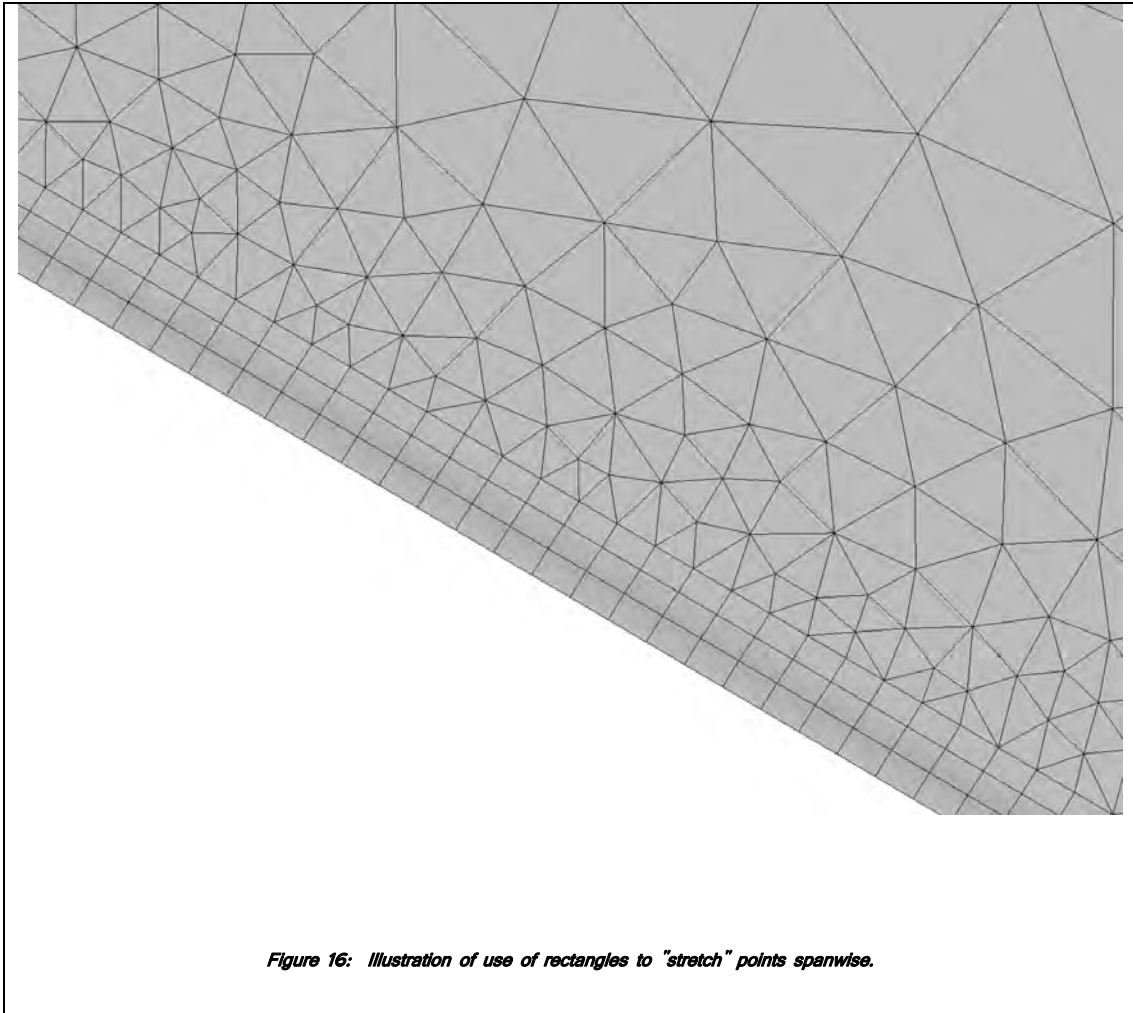


Figure 15: Spanwise view of right wing.

to accurately describe it. Thus, it takes more points to capture the chordwise curve of the leading edge than it does to capture the mostly linear spanwise curve along the leading edge. Therefore, the chordwise direction is of greater interest when discretizing the database connectors that define the shape of the leading edge; and the spacing between points can be increased or stretched in directions of less interest (i.e., in the spanwise direction, **Figure 16**).



2.3 Volume Mesh

Once the surface of the geometry file has been segmented and confined inside surface domain meshes, the inviscid volume mesh can be generated. This volumetric generation requires creating large domains that act as sides to a box (the shape of the container is arbitrary) that encloses the

surface mesh. These domains contain coarse spacing relative to that of the surface and are at some distance from the surface on all sides deemed "far field". Far field is the distance at which the fluid flow within the computational domain would behave as if no obstacle was present within the flow field. The spacing is much coarser on these domains; since without the perturbation caused by the presence of the geometry, fluid energies are changing much less rapidly. Typically, the location of these far field domains for compressible viscous flow is a distance of 10 – 15 times some characteristic length of the geometry. For this case the characteristic length is the average chord length of the wing.

Since the inviscid volume mesh is unstructured, the focus will be on the process of generating this type of volume mesh (although the generation processes are similar for both). The volume mesh, as with the surface mesh, will be generated on the half aircraft geometry file and then mirrored about the symmetry plane. A process that is again valid due to the symmetry of the aircraft except for cases of side slip which are not part of this study.

The primary objective of the inviscid volume mesh generator within Gridgen is to fill the volume inside the far field domains and outside the surface domains with mesh points. This can be thought of as filling a box with packing peanuts to surround an object to be shipped. It was not

feasible to attempt this massive point insertion over the entire half geometry at once because of the large number of surface points and the massive computational resources required. To avoid this problem, the mesh was subdivided into smaller, more manageable boxes that could be sequentially filled with points. These boxes of volumetric elements are commonly called blocks.

The insertion of the inviscid volume elements is accomplished by calculating a center point for each triangle on the surface, and then projecting this point orthogonally away from the surface a distance based on the surface triangle edges. When the projected point is connected to its respective triangular points on the surface, a tetrahedron element is formed. The process is similar for the structured surface elements except the resulting volume element is a pyramid since there are four surface points for each projected point.

What is orthogonal to the surface for one triangle may not be orthogonal to the surface for an adjacent triangle. Since all the projected points then have to be connected to each other through other tetrahedra to maintain connectivity, a certain amount of compromise is involved. Gridgen handles this task internally based upon user inputs that control the amount each normally-projected point can be adjusted. Other user inputs include a boundary decay value that works in a way similar to that for unstructured surface domains described earlier—where the specified value controls

the growth of the volume mesh as it moves away from the boundaries of the volume. An aspect ratio value is also available that controls the height of the pyramids relative to the lengths of the sides of the triangular base. Information about Gridgen functionality and volume meshing is in [5].

2.4 Viscous Layering

With a volume mesh in place, viscous layers must be added between the surface mesh and the existing inviscid volume mesh. The spacing between points in these layers is much less than the smallest spacing in the surface mesh or existing inviscid volume mesh. The scale of the viscous spacing is to capture the sharp gradient changes (changes to fluid energies) caused by the viscosity of the fluid and its interaction with the surface of the aircraft.

Viscosity was previously described as “friction-like”. Both friction and viscosity result from shearing forces developed by the movement of molecules past one another. The shear force acts parallel to the plane of the molecules in a manner as to tear the molecules from their neighboring molecules.

The primary difference between the friction that solids experience and the viscosity of fluids is due to a difference in their molecular structures. Solids have a crystalline structure that provides a form

of rigid connectivity between molecules. Because of this, solids deform only when the shear strain developed is greater than the molecular forces of neighboring molecules. Fluids lack this rigid interconnectivity and deform continuously when a shear force is applied. Viscosity is the ratio of the shear strain developed by the shearing force to the rate of shear. Viscosity, then, is a property unique to the fluid and the strength of its molecular bonds.

This shear force can be idealized as the force a person feels when stepping off a moving airport walkway onto solid ground. A shear strain develops both in the floor and in the person's shoe. A fluid particle can be thought of as the person for purpose of understanding. As the particle moves as part of a free stream (unencumbered by contact with a solid), it is similar to the person on the moving walkway. When the fluid encounters the surface of a solid, it feels a shear force similar to that attempting to de-shoe the unsuspecting person in the example above. This force brings the fluid particle to a halt. Thus, fluid particles adjacent to the surface have no velocity. This phenomenon is termed the no-slip condition and is applied to all continuous fluids.

The next fluid particle away from the solid surface encounters the previous resting fluid particle, and again experiences the "de-shoeing" shear force, but to a lesser degree due to the forces associated with inter-fluid molecular reactions being less than those for solid-fluid molecular interactions. The

smaller forces may be more attuned to our person stepping from the walkway to a slower moving walkway as opposed to stepping onto stationary ground. This second fluid particle, therefore, does not completely stop moving as a result of its interaction. A third fluid particle even further from the solid surface experiences even less shear. Thus, the viscous effects diminish with distance from the solid, but causes sharp gradients within this small distance.

The viscous layer insertion is a second mesh generation program developed by Dr. Steve Karman of the UT SimCenter [6]. This program uses the linear-elastic stress-strain relationships of solids to squeeze and deform the existing inviscid volumetric mesh while inserting a layer of triangular prisms next to the surface. The linear elastic relationships in solids involve a ratio referred to as Young's modulus (E)

$$E = \frac{\sigma}{\epsilon}$$

Equation 3

where σ is the amount of stress applied to a solid (a force per unit area) and ϵ is the resulting amount of strain developed (or the resulting elongation or compaction experienced by the solid).

Young's modulus is, therefore, a measure of stiffness and a material property. Another ratio used to describe the strength of a solid is Poisson's Ratio. When a solid elongates along one axis, say

its length, it experiences a reduction along the other axis (width) to compensate. This reduction of area is commonly termed necking. Poisson's Ratio (ν) is a comparison of the elongation in the direction of an applied force (ϵ_a) to the resulting necking (ϵ_t):

$$\nu = -\frac{\epsilon_a}{\epsilon_t}$$

Equation 4

The negative sign simply implies that an elongation along one axis results in necking along the other while compaction along one axis results in bulging along the other.

For the viscous layer insertion routine the Young's modulus term is used to stiffen the mesh or retard deformation in areas of tight mesh spacing or around corners and other sharp angles. It is calculated based on the aspect ratio of mesh elements and corner angles. The Poisson's ratio term for this mesh was set to a constant value of 0.25 after a few probing trials, thus limiting the deformation in the axial direction to ¼ of that of the transverse deformation (e.g., an axial elongation of 1 inch would cause a reduction of 4 inches due to necking).

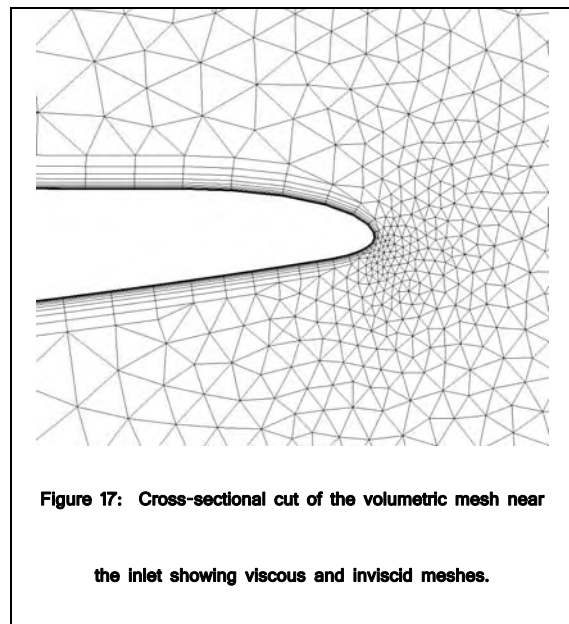
The routine adds one layer of prismatic elements at a time. It starts with the largest elements to

be added and works toward the surface (inward)—only adding elements where the surface mesh spacing is larger than the proposed prismatic element height (the proposed thickness of the viscous layer measured normal to the surface). This process causes elements to be inserted only where they are needed (i.e., where the surface spacing is larger than the required viscous spacing normal to the surface). It then squeezes the existing mesh again and adds another, smaller layer closer to the surface again only adding elements where the surface spacing dictates.

When this routine finished, it had inserted up to the user specified number of viscous layers (25 in this case) between the existing surface mesh and the volumetric mesh and normal to the surface. The net effect was a maximum of 25 layers of triangular prisms extruded from the triangles on the surface mesh.

Atop these prismatic elements sat the pyramids and tetrahedra of the inviscid volume mesh (**Figure 17**).

Upon completion of the viscous layer insertion the total volumetric mesh—



including surface, viscous layering, and inviscid volume meshes—contained 11,869,528 points.

2.5 Adaptive Meshing

Much iteration was performed within each step as well as between steps before obtaining the final mesh outlined above. Initially, the primary changes were coarsening of the surface mesh to lessen the number of points in the mesh using the rule of thumb:

$$\# \text{volume points} = \# \text{surface points} \times 25$$

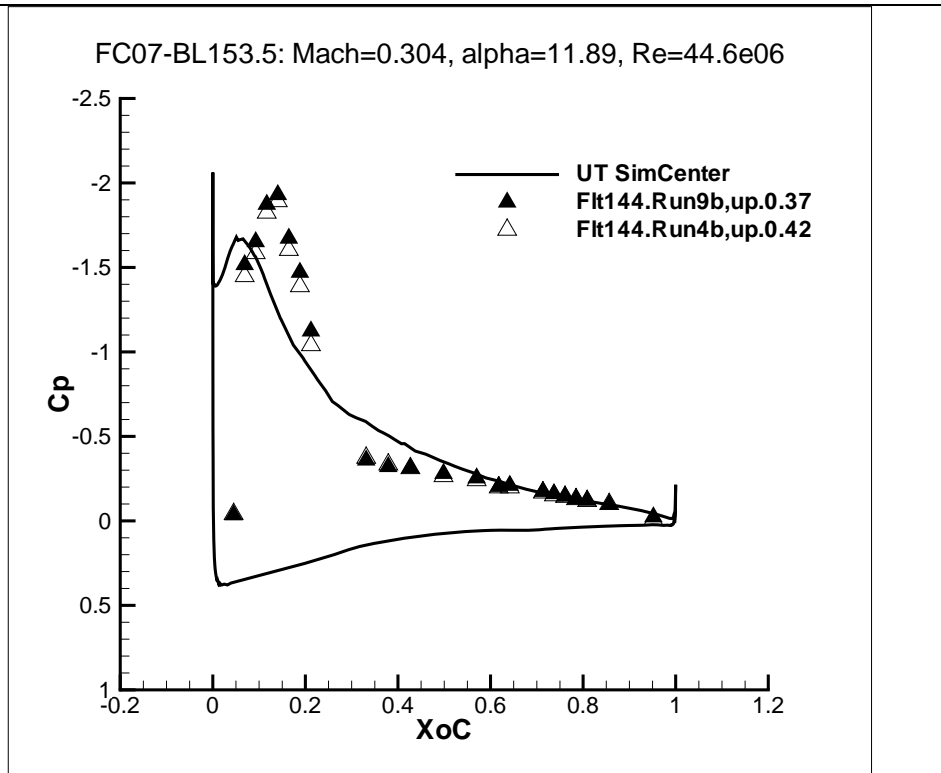
Equation 5

Later baffle surfaces and structured blocks were added to the volume mesh to control its growth rate moving away from the surface. Baffle surfaces are 2-dimensional surfaces that float within the volume mesh and above the aircraft surface. They contain mesh on both sides but have a zero thickness. Spacing set on the connectors of a baffle surface controls the local growth of volume elements serving to constrain the amount of growth that can take place from the aircraft surface to the baffle surface. The structured blocks do the same but have a thickness and are used where a baffle surface would come into contact with the symmetry plane or other boundary

within the volume (ceasing to float within the volumetric mesh). These surfaces were added around the leading and trailing edges, around the wing tip and AIM-9 missile, around the nose mounted air data probe, and around the vertical tail of the aircraft. All these areas contained very tight mesh spacing that lay adjacent to considerably more coarse spacing. The volumetric mesh above the tighter spacings attempted to grow too quickly to obtain smooth transitions with the volume above the coarse surface spacing; that is, the spacing had to quickly reach a common point of equal spacing in this transition zone which was being driven by the coarser spacing.

Perhaps the most noteworthy mesh changes were to the spacings along the upper wing surface.

It was noticed that the CFD data were failing to match the experimental fluid dynamic (EFD) data along one chordwise path circling the wing. The peak of the CFD data was shifted to the right of the corresponding peak within the EFD data, which showed a disagreement in the distance from the fuselage of the highest pressure reading (**Figure 18**).



Examination of the solution utilizing a post-processing visualization software package called Fieldview [7], showed that the shapes of the volumetric mesh elements could be seen in a color coded representation of pressures values within the computational volume. The shapes were observed along the same chordwise path around the wing surface. This indicated that the pressures were not changing naturally within the volume at these locations (as would be noted by smooth transitions), but were driven by the spacing within the mesh. The pressures in these

areas were changing rapidly due to the presence of vortices, and the mesh spacing was too coarse to properly capture these changes. This was perceived as a possible cause of the disagreement in EFD and CFD data: the mesh was too coarse at this section causing the vortex to dissipate prematurely.

The term vortex refers to the rotational motion of fluid molecules about a common center.

Examples of vortices are tornados and whirlpools. The fluid particles of a vortex accelerate toward the center resulting in higher velocities near the center than at locations further from the center. Pressure and velocity work inversely to each other in a moving fluid. Thus, pressures at vortices centers (cores) are lower.

On the F-16XL, vortices form at the leading edge of the wing when the angle of attack is sufficiently large. The angle of attack is the angle the aircraft makes with the direction of flight.

Aircraft in general are streamlined to reduce the drag or viscous effects acting parallel to the surface. As the angle of attack increases, it serves to bring the stream lined profile of the wing

(**Figure 14**) out of line with the flow stream. This results in the first contact between the free

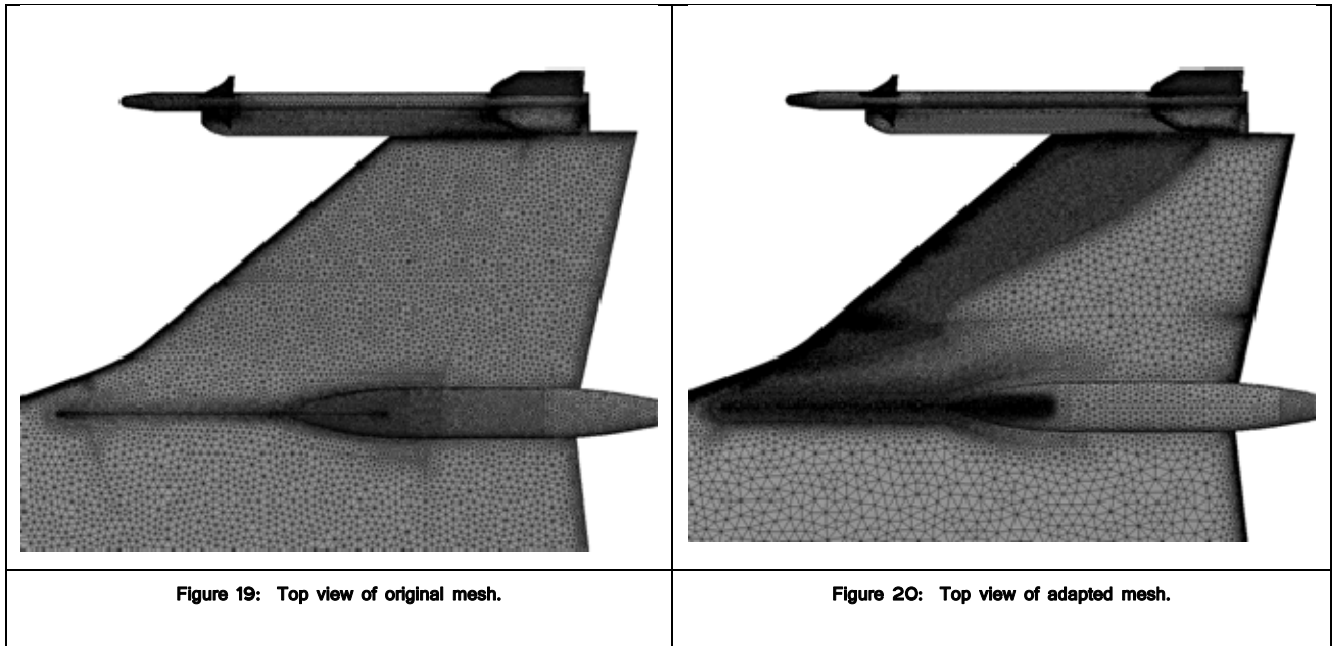
stream air and the plane surface, the stagnation point, being moved from the rounded profile of

the wing's leading edge to a blunter surface of the wing. Stagnation points are points where the

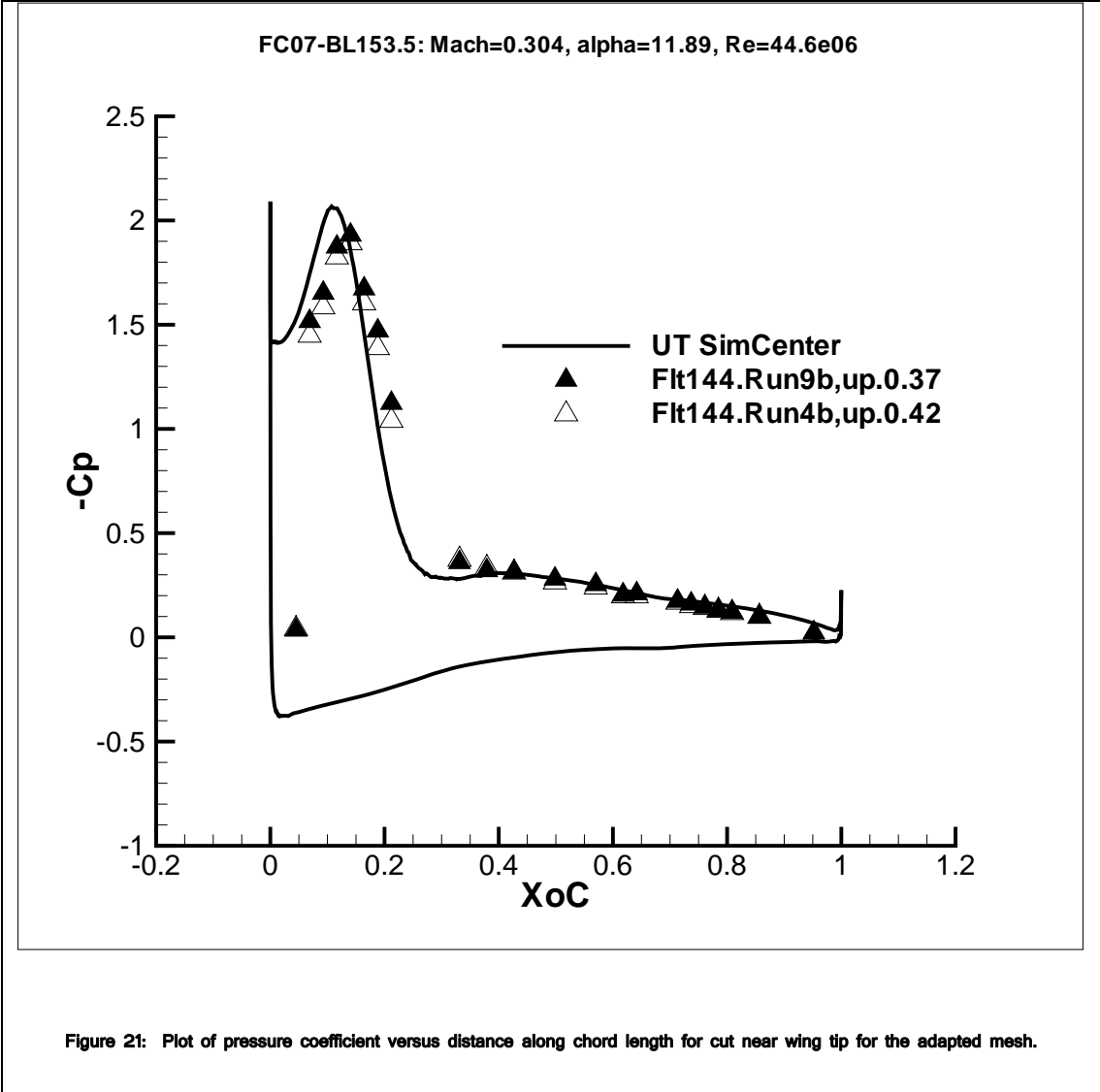
flow stream is temporarily stopped (stagnated) from contact with a blunt surface. Air in this stagnated region retards the flow of the approaching free stream, forcing it upwards and away from the surface of the aircraft. As these air particles again collide with other free stream particles further away from the surface, they are forced back toward the surface and rotational flow develops.

Fieldview was then employed to extract the vortex core path from the current solution. This path was then exported to AutoCAD Mechanical Desktop and smoothed to a more linear representation of the path [8]. A cylinder was then created around the path with an assumed radius long enough to encompass the actual vortex path. This cylinder was then exported to Gridgen as a database entity like that of the aircraft geometry. A surface mesh was applied to the upper half of the cylinder surface with mesh spacing roughly one-fifth that observed in the volumetric mesh previously. The surface formed a 'C' shaped baffle surface above the wing that traced the probable vortex path and constrained the growth of the volume mesh. This surface was then marched (or extruded) toward the surface to form a block (another method Gridgen offers for forming the volumetric boxes or blocks described earlier). The wing surface below the baffle was similarly refined. Having identified the approximate location for phenomena of interest on the upper wing surface from the initial solution, areas of lesser interest were coarsened (Figure 19 and

Figure 20) to limit the impact of the vortex path refinement on the total number of volumetric mesh points (Equation 5).



After refinement, the C_p data agreement with the experimental data was better at this location (Figure 21).



Upon completion of the mesh refinement, the total volumetric mesh—including surface mesh,

viscous volume, and inviscid volume—now contained 13,906,708 points. This was an overall

increase of approximately 1.2 million points for the computational domain.

2.6 Boundary Conditions

Once a discrete computational domain has been obtained, the boundary conditions must be specified before applying the solution algorithm. Previously the fact that the only fluxes entering or leaving the computational domain do so through its boundaries was discussed. The boundaries are those domain meshes that serve to close the computational domain, thereby making it finite. For the model these are the far field (sides of the box) domains and the surface mesh representing the aircraft.

Specifying the conditions at these boundaries provides the solver (the computer code that executes the solution algorithm) with information about the possible fluxes across the boundaries.

For this model there are four different types of boundary conditions: far field, solid surface, inflow (flux across a boundary into the computational domain), and outflow (flux across a boundary leaving the computational domain). A far field boundary condition establishes the flow field parameters for the problem. It provides information about the flow (velocity, Reynold's number, etc) in the form of net system fluxes across its boundaries. A solid surface boundary condition

indicates that there is a no slip (zero velocity) condition enforced on fluid particles immediately adjacent to the surface. The solid surface boundary condition also mandates that there are no gradients across the boundary (i.e., changes in temperature or pressures).

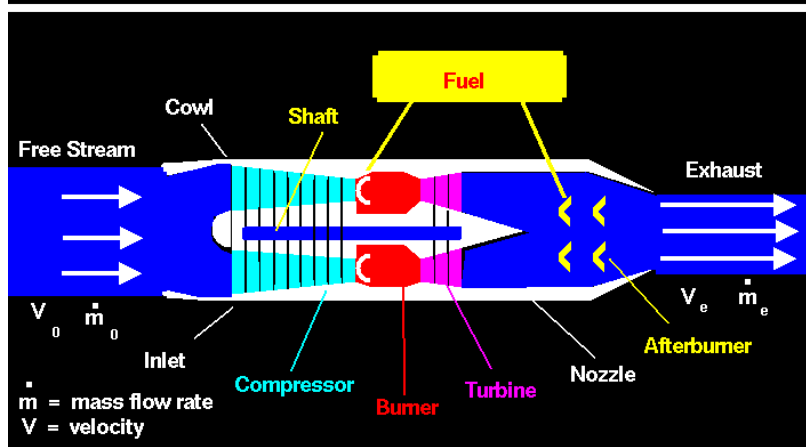
The only inflow boundary condition for the aircraft model is that representing the nozzle aft of the turbine. Here the boundary condition was set as a positive back pressure based upon pressure measurements taken during stand testing of the aircraft's turbine engine. Mass flow out of the actual nozzle provides the thrust for the actual aircraft while the positive back pressure boundary condition enforces realistic flow through the modeled nozzle.

The only outflow boundary condition is at the face of the compressor. Here the boundary condition was set as a negative back pressure inducing suction through the face representing the intake of the compressor. **Figure 22** shows a schematic of a typical turbine aircraft engine represented by the "black box" between the inflow and outflow boundary conditions.



Afterburning Jet Thrust

Glenn
Research
Center



$$\text{Thrust} = F = \dot{m}_e V_e - \dot{m}_0 V_0$$

Figure 22: Schematic of typical turbofan engine [2].

Table 1 summarizes the corresponding pressures of each flight case [4].

Table 1: Summary of conditions at the inlet and nozzle faces.

Flight Condition	Free Stream Altitude, ft.	Free Stream Mach	Inlet Duct Exit Static Temp., degs. R	Inlet Duct Exit Static Press., psia	Inlet Duct Exit Velocity, ft/sec	Inlet Duct Exit Mach	Mixing Plane Total Temp., degs. R	Mixing Plane Total Press., psia
FC7	5000	0.304	498	11	379.6	0.347	1050	23
FC70	22300	0.97	519	10.65	464.7	0.416	1200	30
FC25	10000	0.242	470.1	8.72	474.8	0.447	1209	26.3

2.7 Unstructured Solver

The UT SimCenter unstructured solver is an implicit, parallelized solution algorithm for numerically approximating the Reynolds-averaged Navier-Stokes (RANS) equations within a flow field. The algorithm has roots in the implicit flow solver of Anderson [9] and has evolved over 15 years of continued development and validation over a wide range of flow conditions. A descriptive discussion of these features follows.

2.7.1 Governing Equations

Fluid properties such as density—the mass per unit volume—are by definition only defined within a volume, but often in the study of fluids the properties need to be probed/defined at points within the computational domain (i.e., to find the density at a specific mesh point within the volumetric mesh). Here an assumption that is integral to the study of fluid behavior in general (EFD and CFD) is made: the properties are assumed to be defined over very small but finite volumetric elements. These volumetric elements are considered to be small indeed relative to a very large fluid field. The fluid field is seemingly continuous from the perspective of the small volumetric elements. This allows for so called “point” densities to be defined

throughout the fluid. Fluids for which this assumption is made are termed continuums, and this is likewise termed the continuum assumption [10].

Continuous fluid fields and the continuum assumption offer many benefits toward the development of a set of governing equations; chief among them is the Reynolds Transport Theorem (RTT). The RTT describes the relationship between a system and interactions with the system across its boundaries. It is the key to the development of conservation statement governing extensive fluid properties. For illustration, consider the statement of the conservation of mass termed the Continuity Equation.

Defining a system of fixed boundaries and containing a fixed amount of mass, the Continuity Equation can be summarized as the change in the quantity of mass within the system over a time period is equal to the sum of all internal changes in mass within the system (the internal generation or destruction of the property) over that time period plus the net change caused by quantities of mass crossing the boundaries of the system. If the internal generation or degeneration within the system is zero, then the change in the system is the net "flux" across the system boundaries and becomes a matter of "what comes in" minus "what goes out".

Thus, change in mass of a system is

$$\Delta m_{SYS} = m_{IN} - m_{OUT}$$

Equation 6

since there can be no internal generation or degeneration of mass (matter and therefore mass can be neither created or destroyed). If the mass in the system is not changing ($\Delta m_{SYS}=0$), then the mass coming in must equal the mass leaving the system. Or the change in the mass of the system plus the net flux (net amount entering or leaving the system) must equal zero. Thus the Continuity Equation is a statement of conservation. It is used extensively in the derivation of equations that govern fluid flow.

The computer program that executes the solution algorithm uses a finite volume method to approximate the solution of five integral conservation equations derived by application of the RTT. These equations represent conservation statements governing the mass, energy and momentum in three axial directions of a system and are collectively referred to as the Navier-Stokes equations. The conservative, integral, vector forms of these equations in Cartesian coordinates are written below:

2.7.1.1 Mass Conservation

$$\frac{d}{dt} \iiint_V \rho dV + \iint_S \rho (\vec{u} - \vec{u}_s) \cdot \vec{n} ds = 0$$

Equation 7

Above ρ is the density of the fluid, u is the fluid velocity, u_s is the velocity of the surface relative to that of the fluid, and n is a vector normal to the surfaces of the volume and pointing outward by convention. The term dV is the equivalent of the very small volumes ("point" properties) discussed in association with the continuum assumption. The integral operator serves to sum any property's value within these very small volumes throughout the larger volume of interest (the continuous fluid). Likewise, ds is a very small surface area on the surface of the very small volumes, and the surface integral operator sums the flux across and the forces acting on these very small areas for all such areas within the volume.

Without derivation, the first term of this equation is the rate of change of the sum of all the mass within a finite volume. The second term is the flux of mass across the surfaces of that volume. Thus, the mass conservation equation, as discussed earlier states that the rate of change of the mass within the volume plus the net flux across the surfaces of the

volume is equal to zero.

2.7.1.2 Momentum Conservation

$$\frac{d}{dt} \iiint \rho \vec{u} dV + \iint \rho \vec{u} (\vec{u} - \vec{u}_s) \cdot \vec{n} ds - \iiint \rho \vec{f} dv - \iint \vec{P} ds = 0$$

Equation 8

The conservation of momentum equation states that the rate of change of the momentum within each differential volume summed through out the volume, plus the net flux of momentum across the surfaces of the volume, minus the sum of the body forces (f) acting on the volume, minus the sum of the surface forces (P) acting on the surfaces of the volume are equal to zero. Here the body forces are forces such as gravitational and electromagnetic forces. The surface forces are forces such as pressure and the shear forces related to viscosity as described earlier.

2.7.1.3 Energy Conservation

$$\frac{d}{dt} \iiint \rho e_t dV + \iint \rho e_t (\vec{u} - \vec{u}_s) \cdot \vec{n} ds - \iiint \vec{u} \cdot \vec{f} dv - \iint \vec{u} \cdot \vec{P} ds + \iint \vec{q} \cdot \vec{n} ds = 0$$

Equation 9

Here e_i is the total energy per unit mass and includes latent (or internal molecular energies) and the kinetic energies of a moving fluid. The rate of change of the sum of all the energy in the volume, plus the flux of energy across the volume, minus the body forces acting on the volume, minus the surface forces acting on the surface of the volume, plus the amount net heat (q) flux across the surface of the volume are equal to zero.

The proceeding is meant to give the reader a general idea of how the governing equations apply to a volume of fluid. A more detailed discussion is found in [11][12].

2.7.2 Finite Volume Method

The Finite Volume Method (FVM) provides a way to apply the integral conservation equations to the computational domain. The volumetric terms of the governing equations (those with a leading \iiint) are integrated across each of the volume elements (tetrahedral, pyramids, and prisms), and a volume or cell average is thus obtained for the conserved quantity (mass, momentum (x, y, z), and energy) within each volume element. The values at the mesh points that define each of these volumes must now be found. An interpolation scheme is then applied between the volume-average values in one volume element and those of its

neighboring elements to find values for the conserved quantities at common points.

Finally, the flux terms (those with a leading \iint) are determined using any of many ways of rewriting the flux terms as time averaged values. Since, as we noted in the discussion of the governing equations, the only changes within the volume elements are those from quantities “fluxing” across the surface of the volume; the volume-averaged values can now be advanced in time and interpolated to the mesh points. That is, the volumetric terms of the governing equations are integrated throughout the mesh. Values for the conserved quantities then exist at the volume element centers. The fluxes are then time-averaged and their effects added to the volume centers. Then the volume center values are interpolated between adjacent volumes to determine the conserved quantity values at the mesh points. Finally the solution is moved forward in time where the process is repeated.

Intuitively the flux leaving the surface of one volume element is the same as that entering the volume element sharing that surface; therefore, the only net flux to the computational domain (total volumetric mesh) is that entering or leaving the boundaries (the box sides or surface mesh) of the computational domain. This guaranties conservation throughout the computational domain.

2.7.3 User-Defined Variables

The unstructured solver is a computer code that, for a given input—user defined variables and a computational domain (volumetric mesh with appropriate boundary conditions)—executes a solution algorithm based on the finite volume method described above to approximate the RANS Equations. There are many variables under the user's control within the unstructured solver, but this discussion will focus on those of primary interest: Courant number, number of iterations, regime type, scale factor, unsteady flag, implicit limiter, Newton's iterations, and turbulence model. Of these the turbulence model will require a more detailed explanation and, therefore, will be treated separately. In addition to the input parameters mentioned above, there are those descriptor characteristics inherent to the flow: Mach number, Reynolds number, the ratio of specific heats (γ), the flow direction, and the lift direction.

The latter two are vectors calculated from the angle of attack and angle of sideslip. The flow direction vector is computed solving

$$\vec{u} = u \cos \beta \cos \alpha$$

Equation 10

$$\bar{v} = u \sin \beta$$

Equation 11

$$\bar{w} = u \cos \beta \sin \alpha$$

Equation 12

where α and β are the angles of attack and sideslip defined previously; u is the linear velocity of the air relative to the aircraft; and \bar{u} , \bar{v} , \bar{w} are the three directional components of the velocity.

The Courant number or CFL (Courant, Friedrichs, and Lewy) number is a relationship between the time step size (Δt) and spatial step size (Δx).

$$CFL \cong \frac{\Delta t}{\Delta x}$$

Equation 13

The spatial steps are the spacing between the mesh points of the computational domain.

Setting the CFL number then governs the resulting time step (i.e., larger CFL numbers yield larger time steps and vice versa). The CFL number is employed in von Neumann's analysis for solution stability. Although von Neumann's analysis determines CFL numbers that provide

stability for numerical approximations to linear partial differential equations (PDE's), it works well as a guide for stability in non linear PDE's as well.

Truncation error is inherent to all numerical methods. Von Neumann's analysis establishes an amplification factor (G) that is a ratio of the error induced through approximation at the next time step (ϵ^{n+1}) to that induced through approximation at the current time step (ϵ^n).

$$|G| = \left| \frac{\epsilon^{n+1}}{\epsilon^n} \right|$$

Equation 14

For stability G must be no greater than 1, that is, the error at the future time step can be no larger than the error at the current time step. Thus, the error is not growing as the approximation is advanced through time. CFL numbers are then chosen to yield a G that is no greater than unity.

The number of iterations in the solver is the number of time steps that will be executed. As stated earlier the size of these steps is governed by the chosen CFL number; therefore, it affects how quickly the approximation is advanced in the time domain. Usually a CFL number

is chosen and the number of iterations is set. The approximation is then examined for iterative convergence at the end of these steps. Iterative convergence means that the solution approaches steady state (constant) values. In the previous water faucet example, if sometime after turning the faucet on the flow leaving the hose has not reached a constant value, then it has not reached its steady state and is in a period of transients. Similarly, if the approximation has not converged to a constant solution, it must be restarted from the current time and run for additional iterations (time steps), or it can be restarted from the beginning with a larger CFL number if possible (i.e., each time step would be larger).

The regime type in the solver refers to the type of flow. For this model the “varMach” regime is chosen to handle the viscous, compressible flow at a wide range of Mach numbers. The scaling factor is the characteristic length used to non-dimensionalize the length of the model. Here the average chord length of 7.5208 feet is used. The unsteady flag is used for time dependent models: those where the solved values vary with time. For the steady state model of the F-16XL this flag was turned off.

The implicit limiter function helps to obtain solution values at mesh points that border discontinuities. As discussed previously, abrupt pressure changes occur in association with

shock waves. The pressures in front of the shock wave are dramatically higher than those behind the wave. Between these points exists a discontinuity. The implicit limiter “interpolates” (for the case of first order limiters) to find property values across the discontinuity.

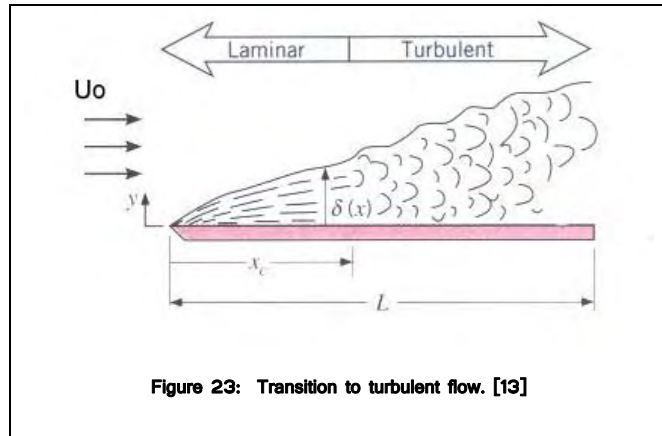
Newton’s iterations are additional iterations that are taken between time steps and serve to more quickly advance an approximation toward convergence. They also help to minimize effects of the enforcement of boundary conditions by allowing values at volume elements near the boundaries to be updated within each time step.

2.7.4 Turbulence Modeling

As discussed previously a transition area exists next to the surface of a solid that is in contact with a moving fluid. This area next to the solid surface where fluid velocities are affected by the developed shear is known as the boundary layer. The boundary layer thickens as the fluid continues along the surface due to shear stresses and their effects on growing numbers of

fluid particles (Figure 23).

At some distance after first contact (x_c) that is unique to the fluid and the surface, the boundary layer becomes unstable due to the “traffic



jam” of fast moving particles colliding with slower moving particles. At this point the boundary layer is said to be fully developed (no longer growing in thickness, δ) and the flow begins the transition to turbulent flow.

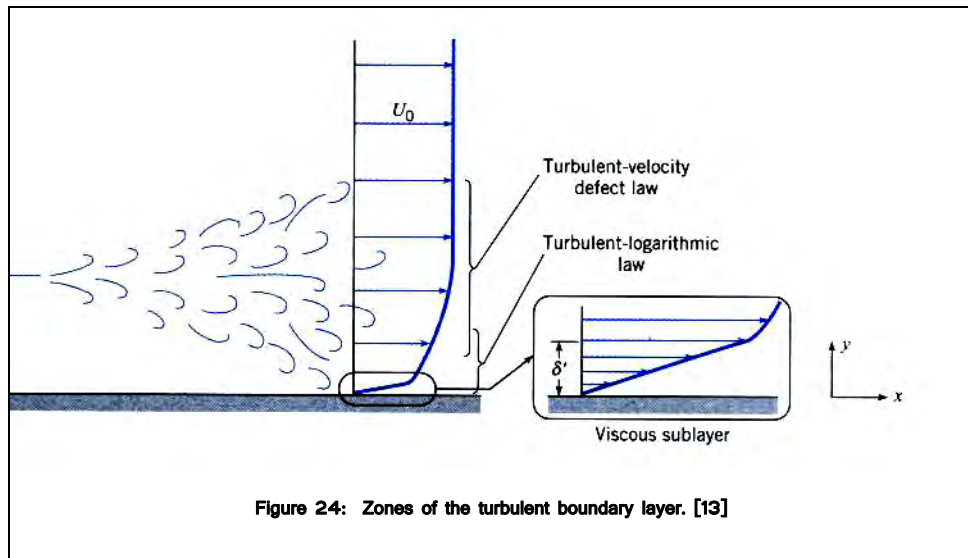
Before this transition point the flow moves in stream lines (paths of particle movement in nearly straight lines) that are mostly parallel to the surface and have predictable velocity and pressure behaviors. Past this point the onset of turbulence causes the particle paths and the fluid’s properties to behave in an increasingly chaotic nature. Pressure and velocity values become increasingly stochastic or non-deterministic due to the mixing action of the fluid particles. This mixing motion is due the development of eddies within the flow that visually

characterize turbulent flow (**Figure 23**).

Because of this non-deterministic or erratic behavior of fluid properties within the boundary layer of turbulent flow, much research has been directed toward finding methods to predict or model this behavior.

One such effort of this type attempts a direct solution with no separate model for turbulent behavior by packing large numbers of points into the boundary layer adjacent to simple geometric surfaces (flat plates, cylinders, etc.) and directly applying the RANS equations. This method is termed Direct Numerical Simulation (DNS). While approximations made using this model generally agree well with experimental results, the computational cost is much too high for practical uses. "Any flight vehicle large enough to carry a human ($L > 3$ m), moving faster than 72 km/h (20 m/s) is well beyond the limit of DNS simulation ($Re = 4$ million)." [14]

Other prevalent types of turbulence models are the so called zonal models. The turbulent boundary layer has three "zones" of flow compared to the single zone of laminar flow. The layer immediately adjacent to the wall is called the viscous sub-layer (**Figure 24**).



Fluid flow here remains relatively calm due to the shear forces developed from contact with the wall and is essentially laminar flow. The shear across this thin layer is nearly constant (that of the wall and first row of fluid particles (τ_w)), and the resulting velocity is termed shear velocity (u^*).

$$u^* = \sqrt{\frac{\tau_w}{\rho}}$$

Equation 15

Outside this zone purely turbulent flow exists. In the remaining two zones the mixing action of fluid particles causes slower moving particles close to the surface to be swept away from the surface and into faster moving regions. This mixing has a retarding effect on fluid flow in this

region as particles collide (transfer of momentum). Likewise faster moving particles are pulled into the slower moving regions next to the surface. Again collisions take place and momentum is transferred. The transverse particle movement and the momentum transfer between regions of vastly differing velocities causes retarding stresses similar to those caused by contact with the solid surface, but these so called Reynolds Stresses dwarf the shear stresses induced at the surface.

The final two zones are identified by the behavior of the fluid velocities. The first zone, adjacent to the viscous sub-layer, is slightly affected by the viscous sub-layer (particularly shear stresses from the wall) and largely affected by the outer most turbulent zone. The velocities here follow a logarithmic velocity distribution. The outer most zone is unaffected by the shear induced by the wall and obeys the velocity defect law that relates the relative "defect" of velocity given by

$$\frac{U_0 - u}{u^*}$$

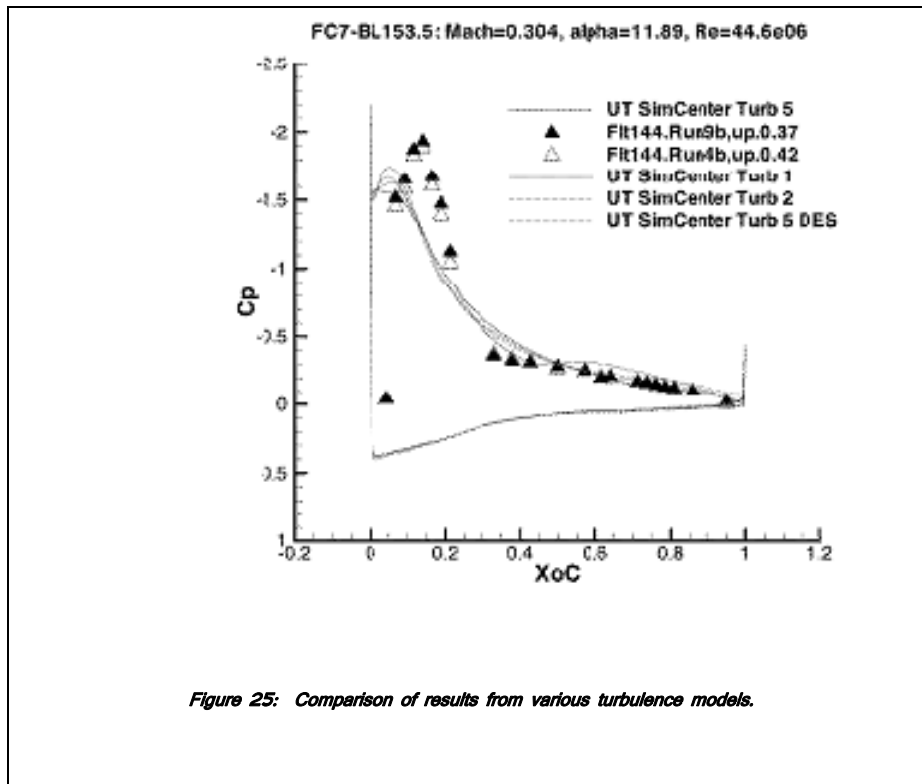
Equation 16

to a normalized distance $\frac{y}{\delta}$. Here U_0 is the free stream velocity, u is the actual velocity at

a point, u^* is the shear velocity defined above, y is the distance from the wall, and δ is the thickness of the viscous sub-layer. [13]

The zonal methods treat the zones or some combination of the zones separately from the flow outside the boundary layer. These methods generally apply two or three equations to calculate eddy viscosities within each zone.

After applying several different turbulence models as part of a parallel study of the F-16XL with no drastic variances between models (Figure 25), the modified K-Epsilon/K-Omega ($k\epsilon$ - $k\omega$) model was employed for this study.



The $k\epsilon$ - $k\omega$ model is a two-equation model that falls into the zonal category described above.

This model is actually a blending of two separate two-equation models the $k\epsilon$ model and

the $k\omega$ model. The $k\epsilon$ model is a derivative of the $k\omega$ model, resulting

from a modification of its turbulent viscosity term. Both models are

based on the Boussinesq assumption that turbulent viscosity is

related to the product of the fluid density and the square of the

stream wise velocity (kinetic energy).

The $k\epsilon$ model calculates a turbulent viscosity based on the turbulent kinetic energy

associated with the transport of shear stresses within the two outer most zones of the boundary layer. It also takes into account the dissipation rate of this energy to calculate the turbulent viscosity.

The $k\omega$ model conversely is applied near the innermost zone and again takes into account the turbulent kinetic energy. The $k\omega$ model also takes into account the energy lost through vorticity fluctuations to calculate the turbulent viscosity. These fluctuations are primarily due to the dominance of shear stresses within close proximity of the surface. The two turbulent viscosities calculated are then combined and added to non-turbulent viscosity term of the RANS equations. Turbulent flow is therefore assumed throughout the computational domain, but the turbulent viscosity term is very small outside the boundary layer—an artifact of its dependence upon the very large turbulent kinetic energies [15].

2.7.5 Parallelization

The computer code that executes the solution algorithm utilizes parallel computing in contrast to serial computing. In serial computing the solution algorithm for an entire computational domain (as defined previously) is executed on a single computer processor and then passed on to the next processor in line. Parallel computing allows the computational domain to be

broken down into smaller pieces and then passed to several computer processors where they are executed simultaneously. This allows for the solution of larger problems or for faster solutions to equivalently sized problems, but requires clusters of computers and the application of controls that govern the layout, the processing and transfer speeds, and the efficiency and strategy for attacking the problem. These all come at financial cost.

The parallelization of the solution algorithm requires the decomposition of the computational domain into sub-domains. The number of sub-domains is determined by the number of processors to be used for computation. This number is specified by the user, and the problem is then decomposed by a routine referred to as Decomp. Decomp employs a commercial parallelization engine called Metis [16]. Metis consists of a group of serial computer programs that execute algorithms to efficiently partition large meshes into manageable components. The number of processors for compressible, viscous flow problems is determined by experience and expressed as the rule of thumb:

$$\#cpu = \frac{\#mesh_points}{200,000} = \frac{13,906,708}{200,000} = 70$$

Equation 17

Here #cpu is the number of processors, #mesh_points is the number of points in the total volumetric mesh, and the quantity 200,000 corresponds to the number of points each processor can handle efficiently for this specific flow type (viscous and compressible). Based on experience, this number may range from 200,000 to 300,000 points per processor. Larger numbers of points per processor lead to longer computation times per iteration. Following Equation 17, the total volumetric mesh for the F-16XL required 70 processors for each flight condition.

Once a flow solution has been found for each sub-domain, the pieces must be put back together using a routine called Recomp. This routine takes the 70 individual “sub-solutions” and re-assembles them back into one complete solution using the Metis engine. The whole solution can then be viewed in Fieldview for interpretation of the results. More information regarding the parallelization of the UT SimCenter unstructured solver can be found in [17].

2.8 Post Processing

All solutions for this study were post processed utilizing Fieldview. This is a graphical visualization packet that allows the examination of flow characteristics such as pressure, velocity, and vorticity

throughout the computational domain. It was used to create all illustrations of the solution to flow characteristics in this study. It was also used to extract values for surface pressure coefficients which were plotted for comparison to those found through EFD.

3.0 Experimental Data

Typically two types of experimental fluid dynamic (EFD) data are used for comparison with CFD results:

test flight data and scaled model wind tunnel data. For this study results recorded during test flights will

be used for comparison. Specifically, three unique flight conditions (FC's) are examined. Each FC is

characterized by four variables under which the data were taken: the velocity of the aircraft relative to

the speed of sound, termed the Mach number (M); the angle of attack (α), which is the angle between

the body of the aircraft and a the direction of flight; the angle of sideslip (β), which refers to rotation

about a vertical axis that brings the aircraft out of line with the free stream air flow; and the Reynolds

number (Re) of the air. The Reynolds number is a non-dimensional quantity that relates the velocity of

the fluid flow (U_0) over some characteristic length (X) to the viscosity (ν^*) of the air and serves to

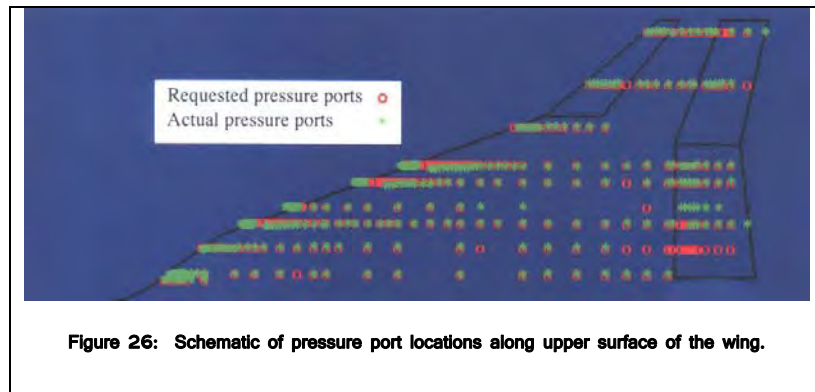
characterize the behavior of the flow (i.e., laminar or turbulent).

$$Re = \frac{U_o X}{\nu^*}$$

Equation 18

The experimental data collected are in the form of surface pressure coefficients obtained from 326 static ports located in streamwise belts along and flush with the surface of the right wing. These belts were positioned such that a sufficient number of ports would lie in chordwise and spanwise paths about the wing surface called butt lines (BL) and fuselage stations (FS), respectively (**Figure 26**). Of the 326 pressure ports, 280 lie upon the upper surface of the wing and 46 upon the bottom of the wing.

The pressure at each location was sensed by one of eleven electronically scanning pressure transducers;



10-psi sensors were used along the leading edge while 5-psi sensors were used elsewhere.

The static pressure measured at each of these ports was normalized by comparing it to the free stream pressure at the same flight conditions to obtain a surface pressure coefficient (C_p) at each location. C_p is calculated by the formula,

$$C_p = \frac{(p - p_o)}{\left(\rho \frac{V_o^2}{2}\right)},$$

Equation 19

where p is a port measurement of static pressure, p_o is the static pressure of the free stream

(unencumbered air stream), ρ is the density of air under conditions at which the measurement was taken,

and V_o is the free stream air velocity.

4.0 Comparison of Results

The EFD results for the coefficient of pressure (C_p) as described in the previous section are now

compared with those obtained through CFD simulation and plotted below using Tecplot [18]. Following

this discussion, there are two data sets presented for each of the three flight conditions (FC): one

comparing EFD and CFD values of $-C_p$ along each of 6 BL or chordwise cuts and the other set for $-C_p$

values along each of 5 FS or spanwise cuts. Negative values of C_p were plotted to conform with the

format of data presented by other groups conducting similar studies. This format also follows a convention common to the study of aerodynamics that the Cp axis is negative upward. The BL cuts are considered constant along the Y Cartesian axis by convention, and these -Cp values are plotted versus a normalized distance from the leading edge of the wing forming a closed loop about the wing. This normalized distance (XoC) is the actual distance in the X Cartesian direction from the leading edge divided by the chord length of the respective butt line. Likewise, the FS cuts are considered at constant X locations and mark normalized distances (YoC) from the symmetry plane, but they do not form closed loops. The FS cuts begin at the symmetry plane and end at the wing tip. A schematic of the BL and FS locations is included with each plot for reference. Table 2 is a summary of the FC's under which the data were taken.

Table 2: Summary of flight conditions.

Flight Condition (FC)	Mach Number (M)	Angle of Attack (α)	Reynolds Number (Re)
FC7	0.304	11.89	44.4E+06
FC70	0.97	4.37	88.77E+06
FC25	0.242	19.84	32.22E+06

The solid lines in the proceeding plots represent data obtained through CFD modeling at the UT SimCenter and are grouped by FC. These data form loops around the upper and lower surfaces of the wing. The symbols capital delta (\square , \square) and nabla (\square , ∇) are used to denote experimental data sensed at the upper and lower wing surfaces respectively where the shaded and non shaded symbols denote separate runs.

4.1 Flight Condition: 07

FC07 was a subsonic case with a Mach of 0.304 and angle of attack of 11.89° . The CFD and EFD data show very good agreement for FC07. The most notable deficiency is the failure of the CFD model to predict the minimum pressures (the maximum $-C_p$ values) seen by the actual wing during the test flight along BL55 and BL70. This is noticed to a lesser degree at BL80 and BL95. While the refinement of the wing and addition of the structured block that encased the suspected vortex path along the upper wing improved overall agreement at BL153.5 compared to those before the mesh was adapted in this region (**Figures 18 and 21**), the CFD data are still predicting the associated pressure readings to be slightly farther from the fuselage than the EFD

data shows them to be. FS407.5 and FS450 show discontinuous changes to the pressure in the vicinity of the boundary layer diverter and the fuel tank. While the EFD data nearest this vicinity show good agreement, there is an absence of EFD data within this region to verify these results. The remaining FS cuts also show good agreement, but echo the model's inability to predict the peak pressures along FS300 and FS337.5.

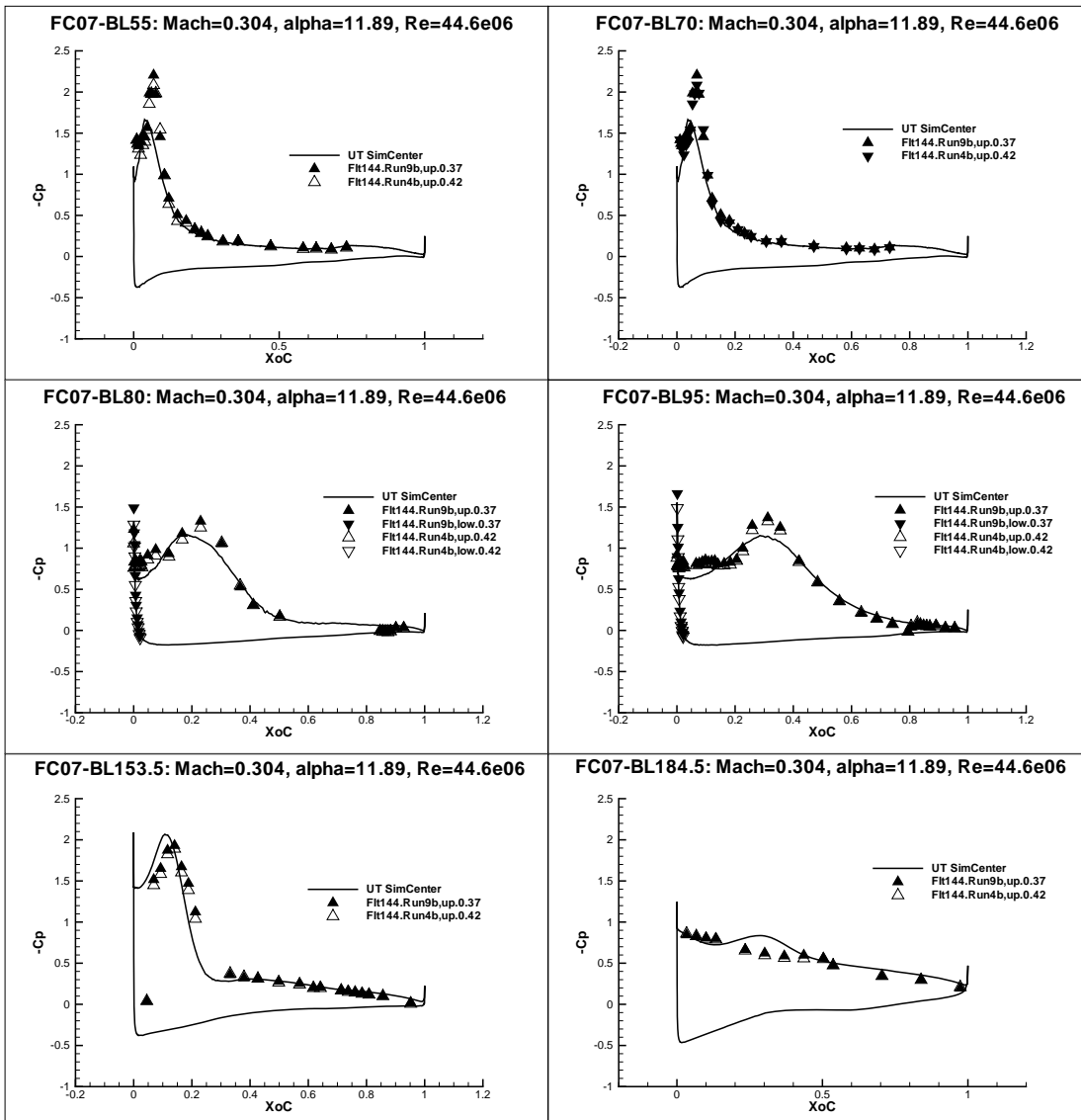
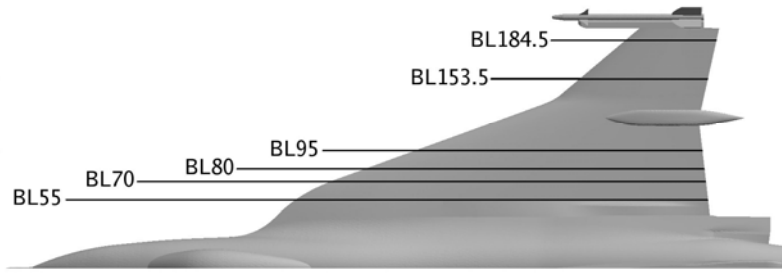


Figure 27: Comparison of C_p along varying BL cuts for FC07.

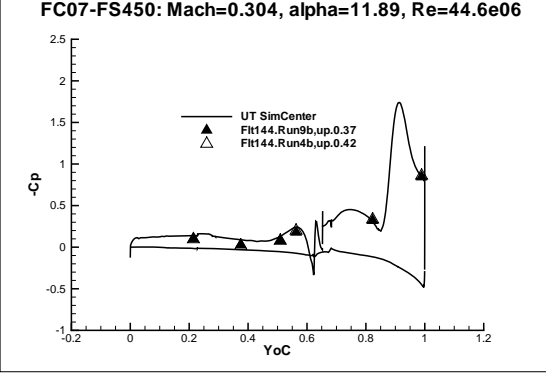
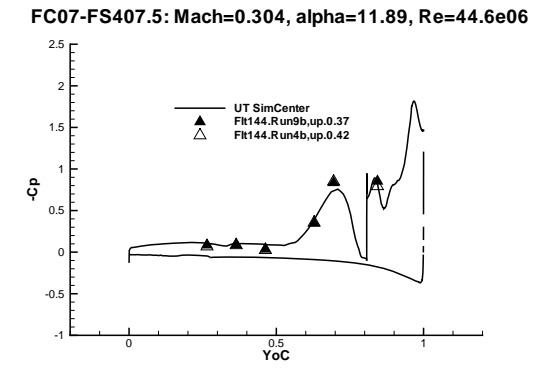
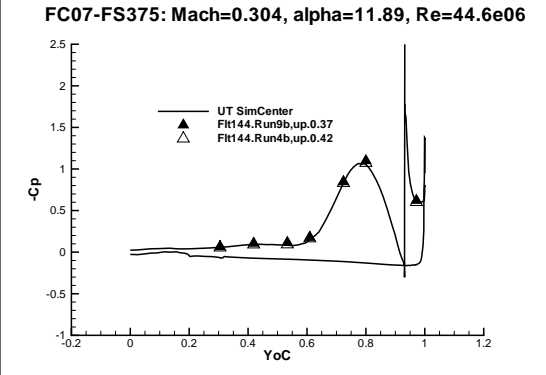
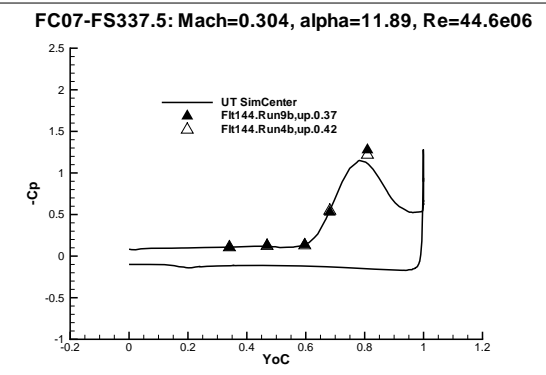
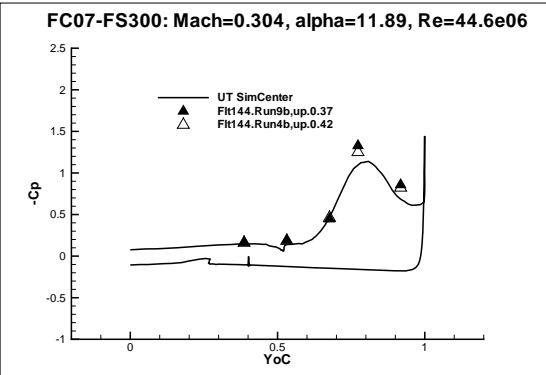
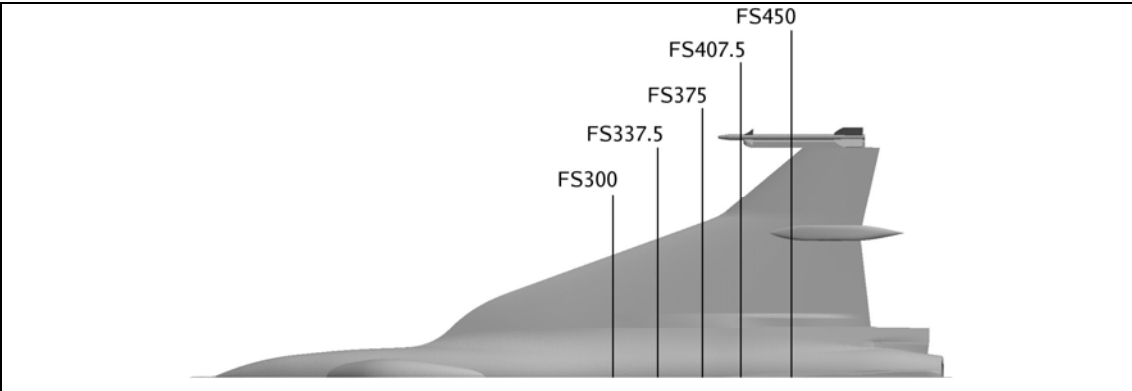


Figure 28: Comparison of Cp along varying FS cuts for FC07.

A plot of color coded C_p values for the entire upper wing surface for FCO7 is included for comparison (**Figure 29**). The solution has been mirrored about the symmetry plane to show a fully configured geometry.

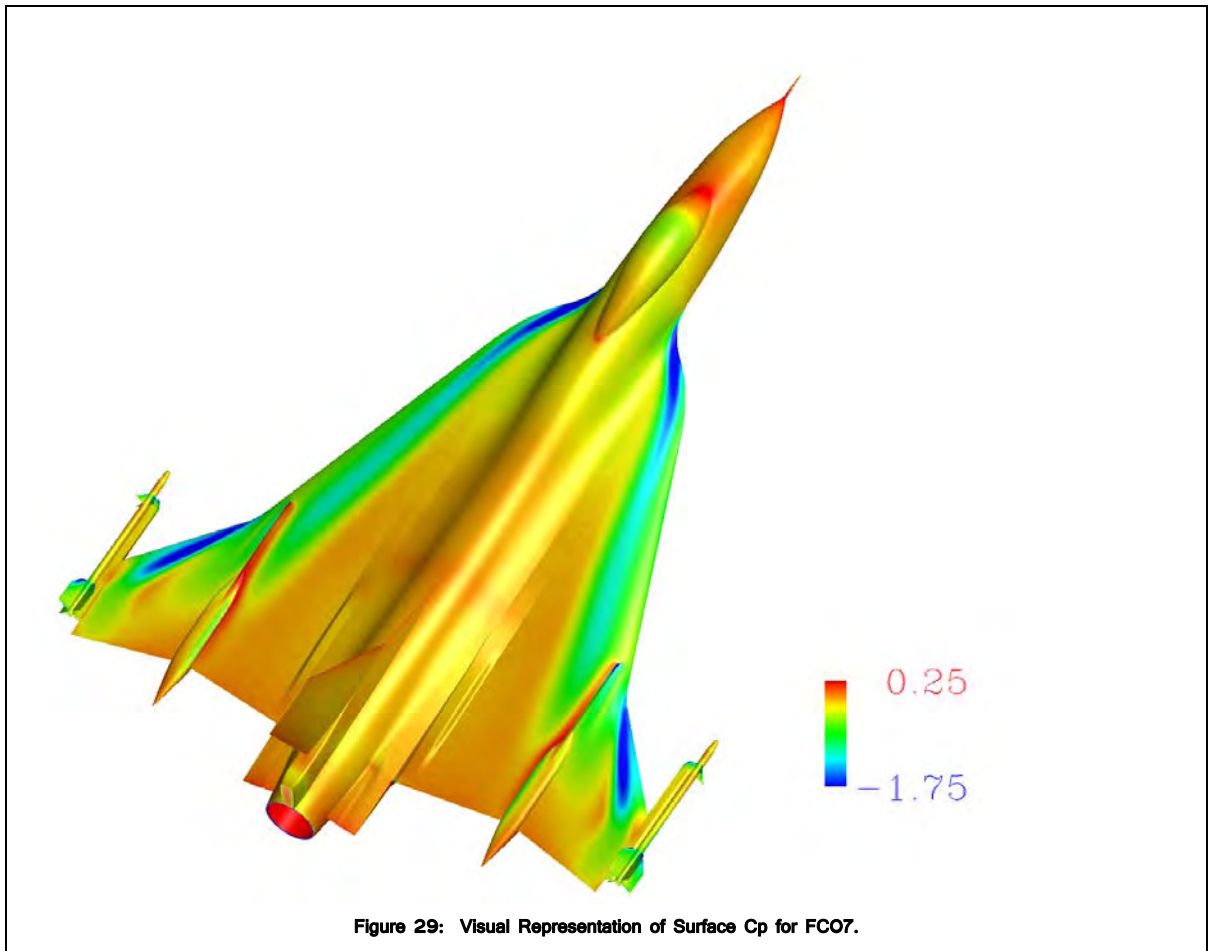
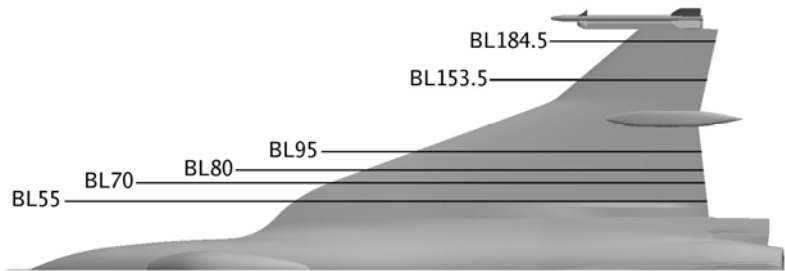


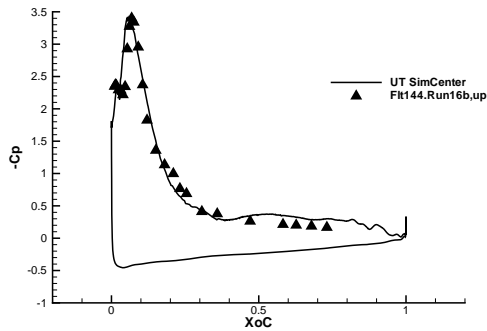
Figure 29: Visual Representation of Surface C_p for FCO7.

4.2 Flight Condition: 25

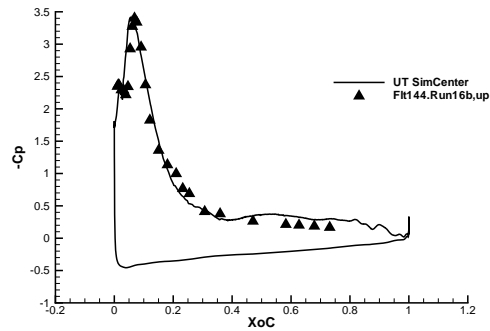
FC 25 data were taken at a subsonic velocity similar to that of FC07 (Mach = 0.242), but with an angle of attack of roughly double ($\alpha = 19.84^\circ$). The data along the BL and FS cuts for FC25 show slightly better agreement than the corresponding cuts for FC07. The CFD model again failed to predict the peak pressure along BL184.5 in an area near the tip missile but with less variance than found in FC07. The FC25 cuts show predicted and actual pressures higher than those experienced during FC07. FS407.5 and FS450 again show discontinuous changes to the pressure in the vicinity of the boundary layer diverter and the fuel tank.



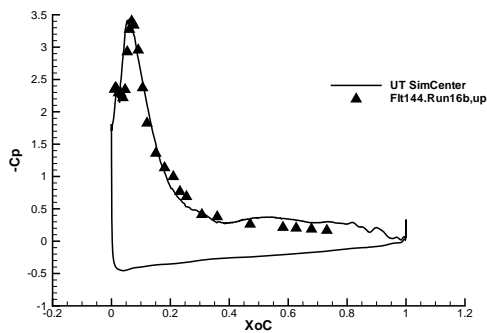
FC25-BL55: Mach=0.242, alpha=19.84, Re=32.22E06



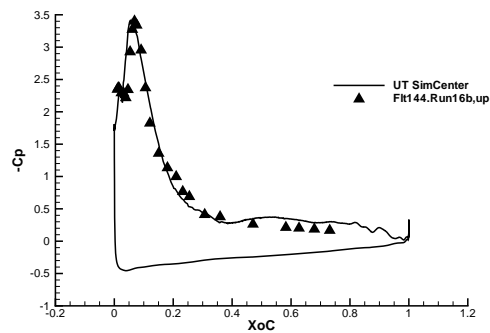
FC25-BL70: Mach=0.242, alpha=19.84, Re=32.22E06



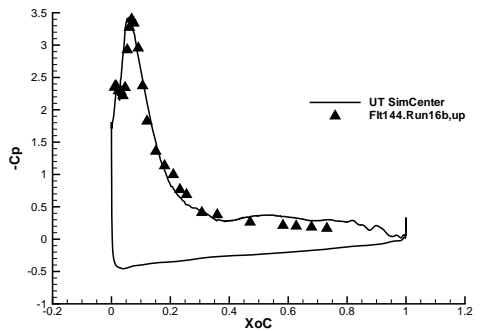
FC25-BL80: Mach=0.242, alpha=19.84, Re=32.22E06



FC25-BL95: Mach=0.242, alpha=19.84, Re=32.22E06



FC25-BL153.5: Mach=0.242, alpha=19.84, Re=32.22E06



FC25-BL184.5: Mach=0.242, alpha=19.84, Re=32.22E06

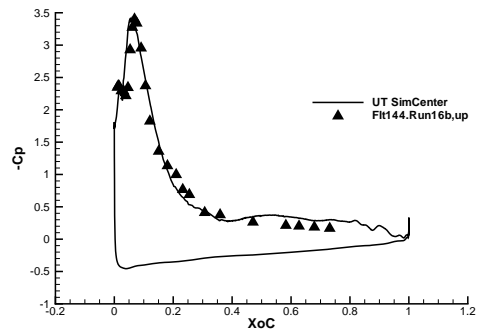
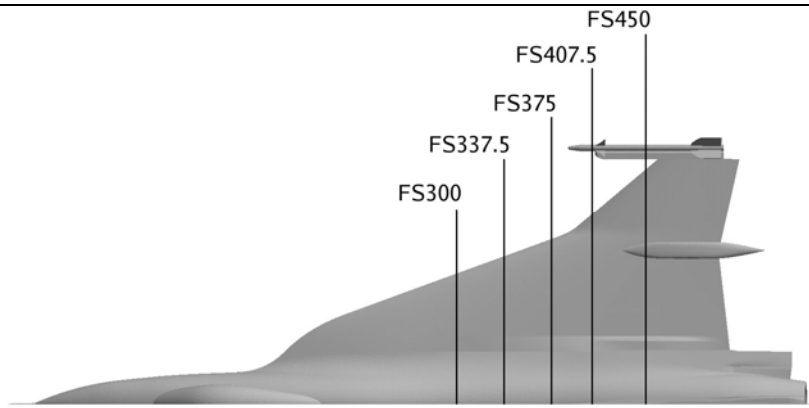
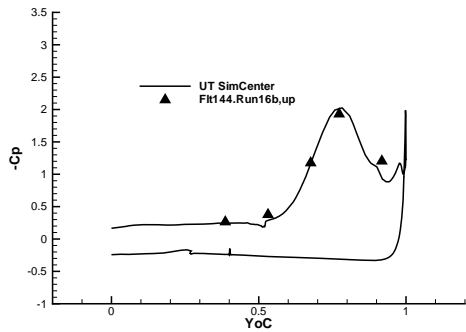


Figure 30: Comparison of C_p along varying BL cuts for FC25.

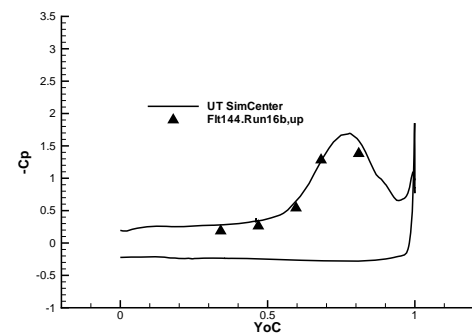




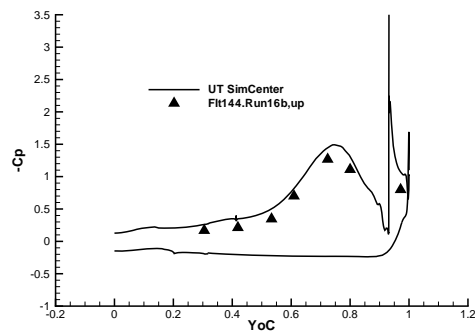
FC25-FS300: Mach=0.242, alpha=19.84, Re=32.22e06



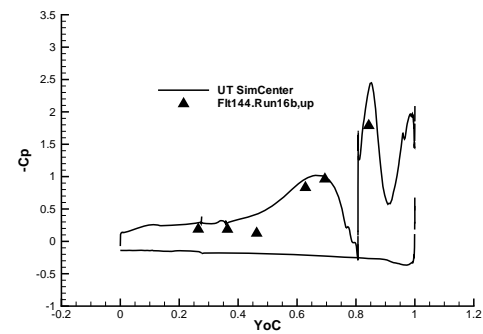
FC25-FS337.5: Mach=0.242, alpha=19.84, Re=32.22e06



FC25-FS375: Mach=0.242, alpha=19.84, Re=32.22e06



FC25-FS407.5: Mach=0.242, alpha=19.84, Re=32.22e06



FC25-FS450: Mach=0.242, alpha=19.84, Re=32.22e06

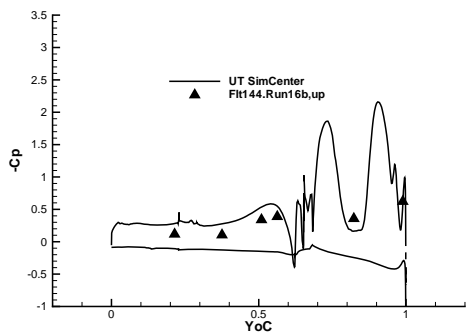
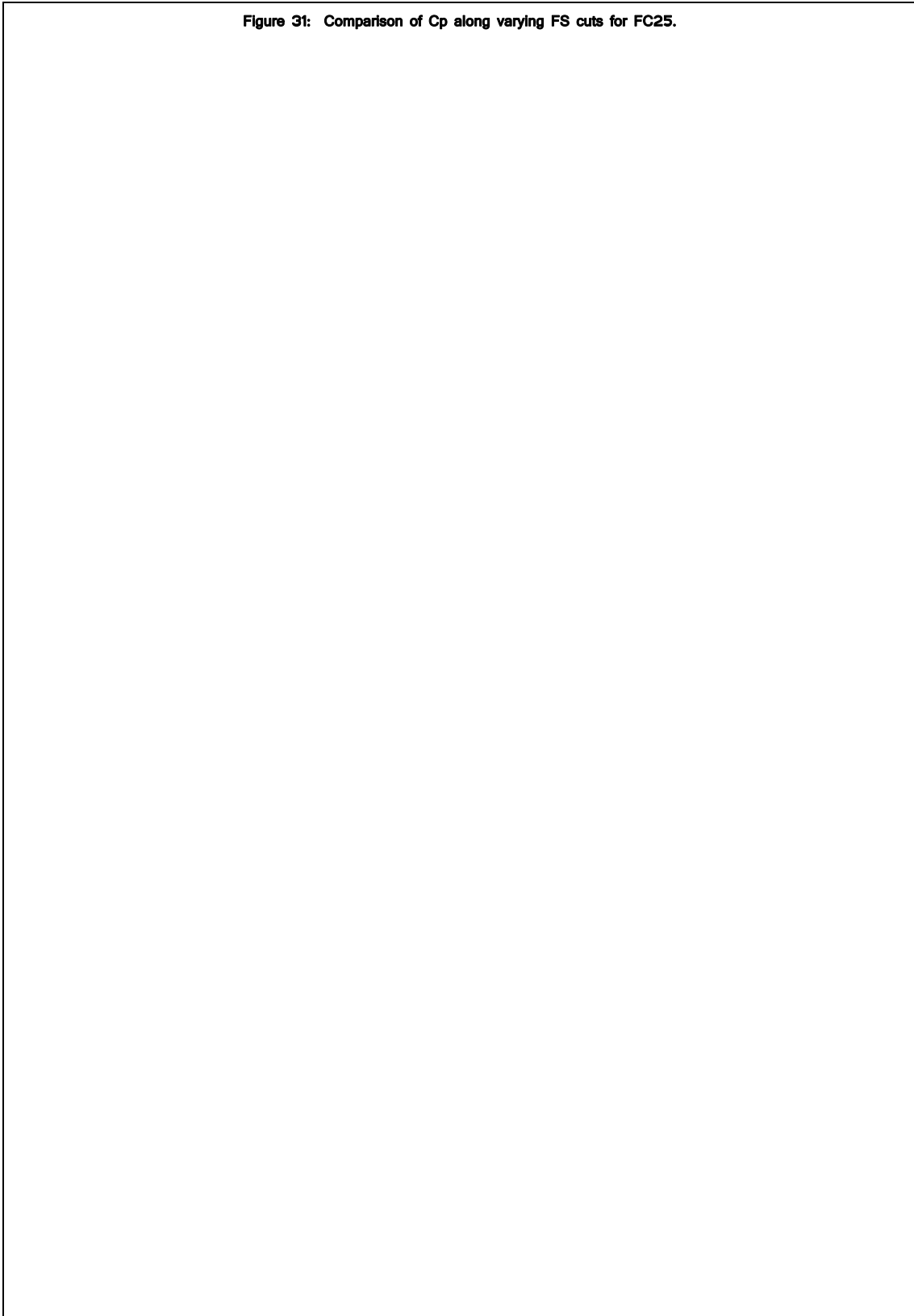
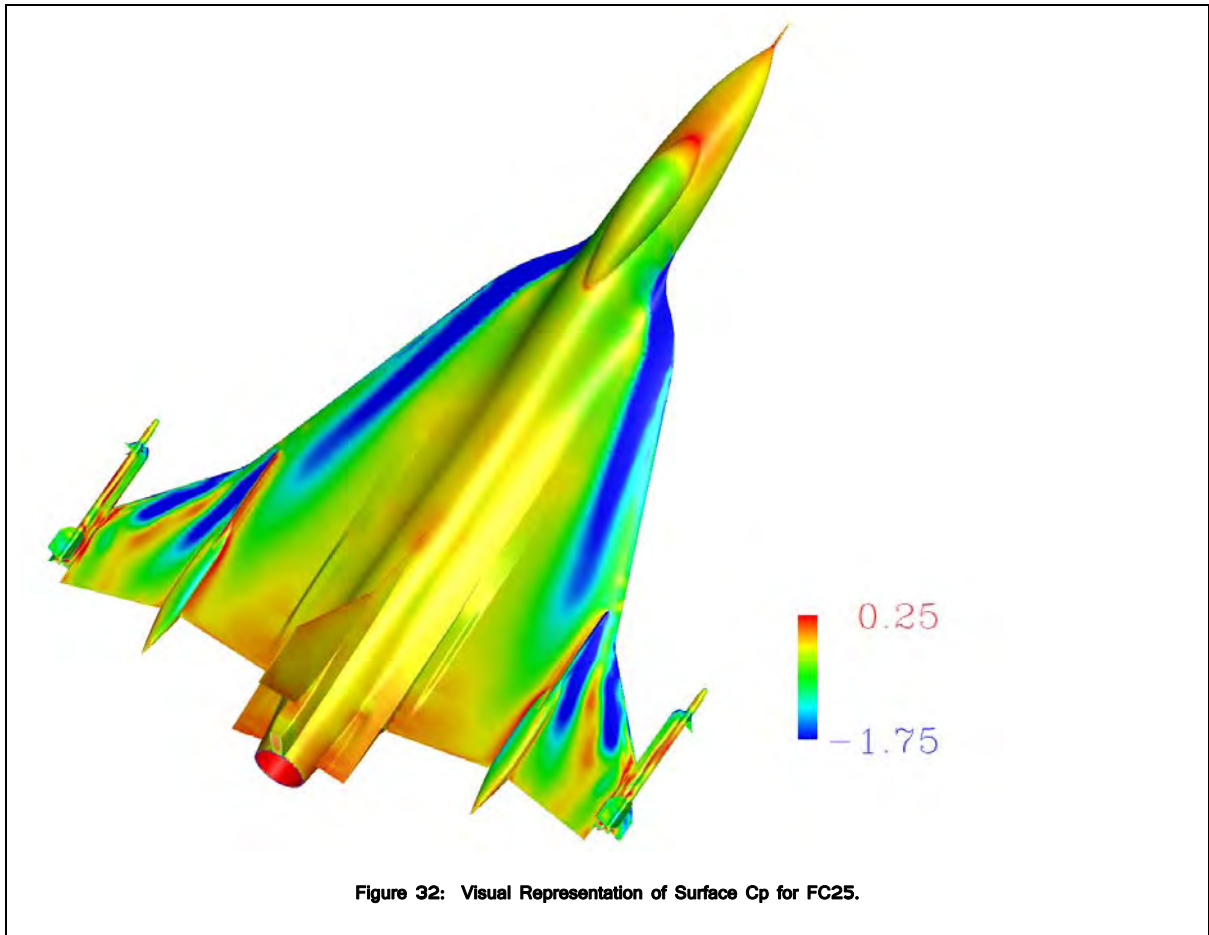


Figure 31: Comparison of Cp along varying FS cuts for FC25.



The plot of the surface C_p values for FC25 is included below for comparison (**Figure 32**).



The darkest blue areas in both **Figure 29** and **Figure 32** correspond to the minimum (maximum – C_p values) pressures seen in the plots for FC07 and FC25 (**Figures 27, 28, 30, and 31**).

These minimum values fall along the path of vortex centers as they move aft and outward from

the fuselage (Figure 33 and Figure 34).

A vortex originates from the wing- fuselage junction at the leading edge. Another originates at the turn in the leading edge outward from the boundary layer diverter. Smaller vortices originate off the tip of the boundary layer diverter and off the aft fins of the missile. The erratic pressure changes near the boundary layer diverter and fuel tanks noticed in the BL plots for

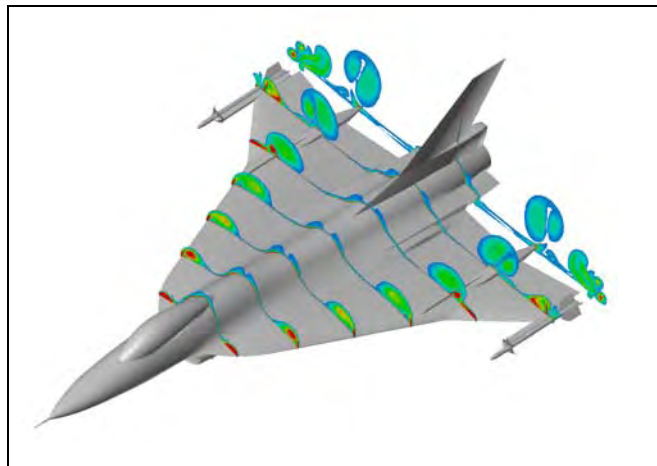


Figure 33: Vorticity Magnitude at constant spanwise cuts for FC07.

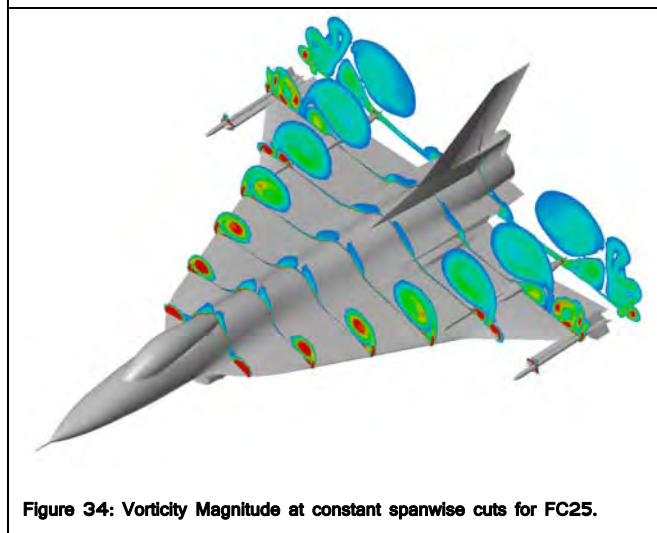


Figure 34: Vorticity Magnitude at constant spanwise cuts for FC25.

FC07 and FC25 are due to sharp corners on the geometry at these locations. As detailed earlier the flow accelerates around curves on the surface of the geometry. The acceleration around corners is even greater. Because the mesh spacing is not small enough to capture these sharp gradient changes, they appear as large jumps between the velocity found at one mesh point relative to that found at an adjacent point. Jumps in velocity translate to inverse jumps in

pressure. Thus the large discontinuous decreases in pressure in the regions near sharp corners are artifacts of the fluid behavior coupled with a lack of mesh resolution.

Also, of interest in **Figure 29** and **Figure 32** are the high C_p values associated with stagnation points along the fuselage nose and front of the canopy.

4.3 Flight Condition: 70

FC70 is the only trans-sonic (near Mach = 1) case examined for this study. It took place at a Mach of 0.97 and an α of 4.89° . The result was much lower pressures experienced by the wing than those of the previous two cases.

The overall agreement for BL55, BL70, and BL95 is very good with the CFD model capturing the maximum and minimum pressures experienced by the wing surface. The remaining BL's and FS's also show reasonable, but slightly less, agreement with the model—once again failing to predict peak pressures. The peaks predicted in BL's 153.4 and 184.5 also reside at the wrong location.

A possible cause for the discrepancies between the CFD and EFD data for this flight case is the absence of leading edge deflectors in the model. The actual F-16XL is equipped with computer controlled leading edge deflectors which improve stability at high speeds. These deflectors were not included in the IGES geometry and, therefore, were not modeled.

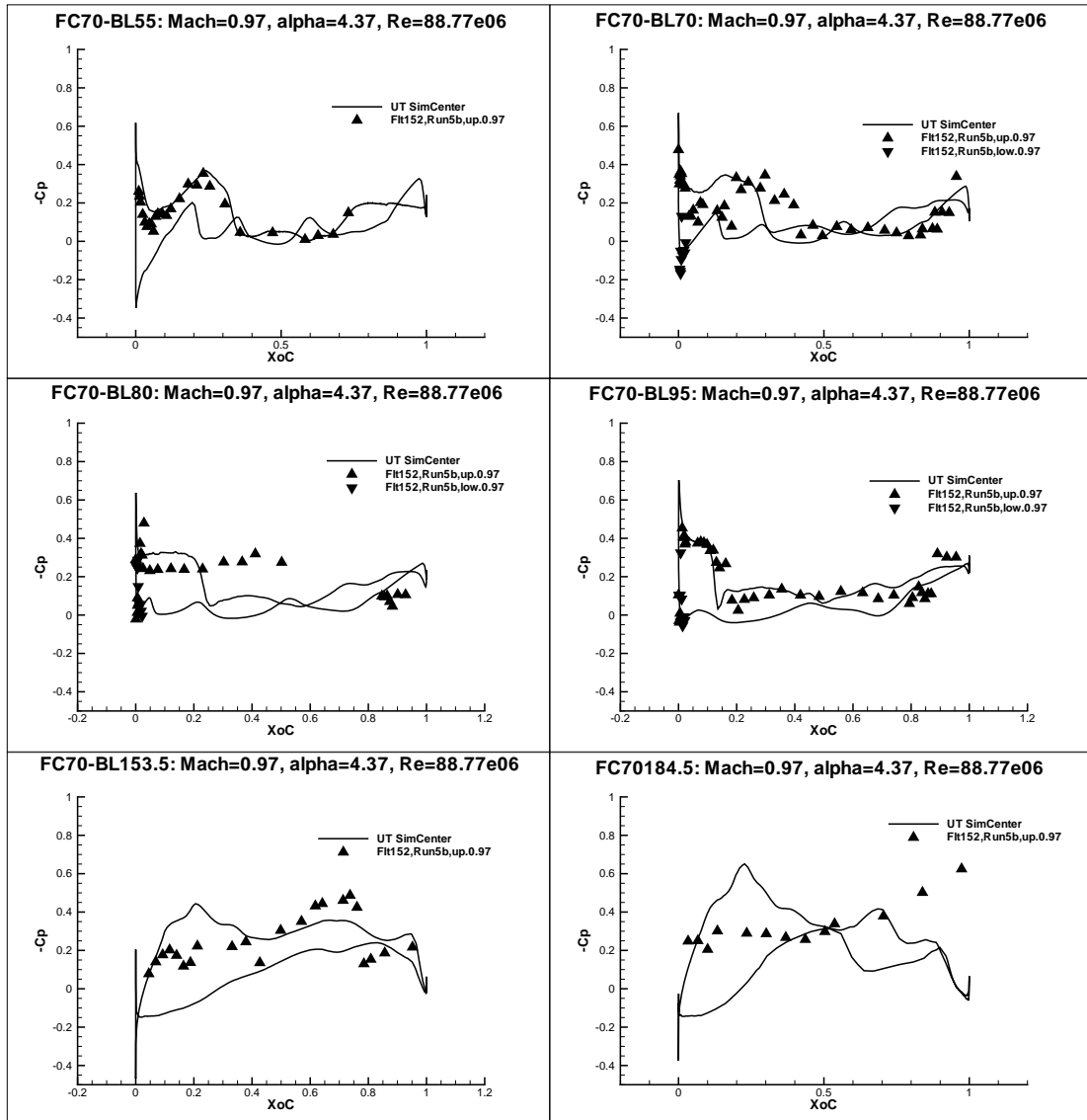
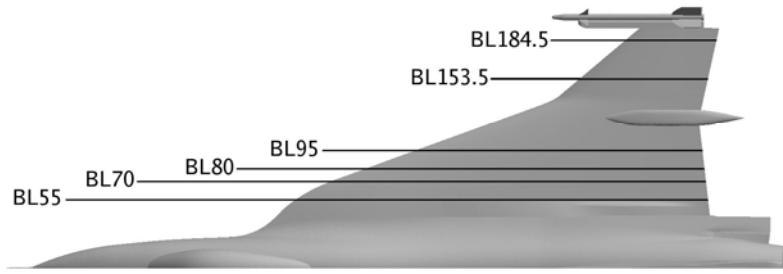


Figure 35: Comparison of C_p along varying BL cuts for FC70.

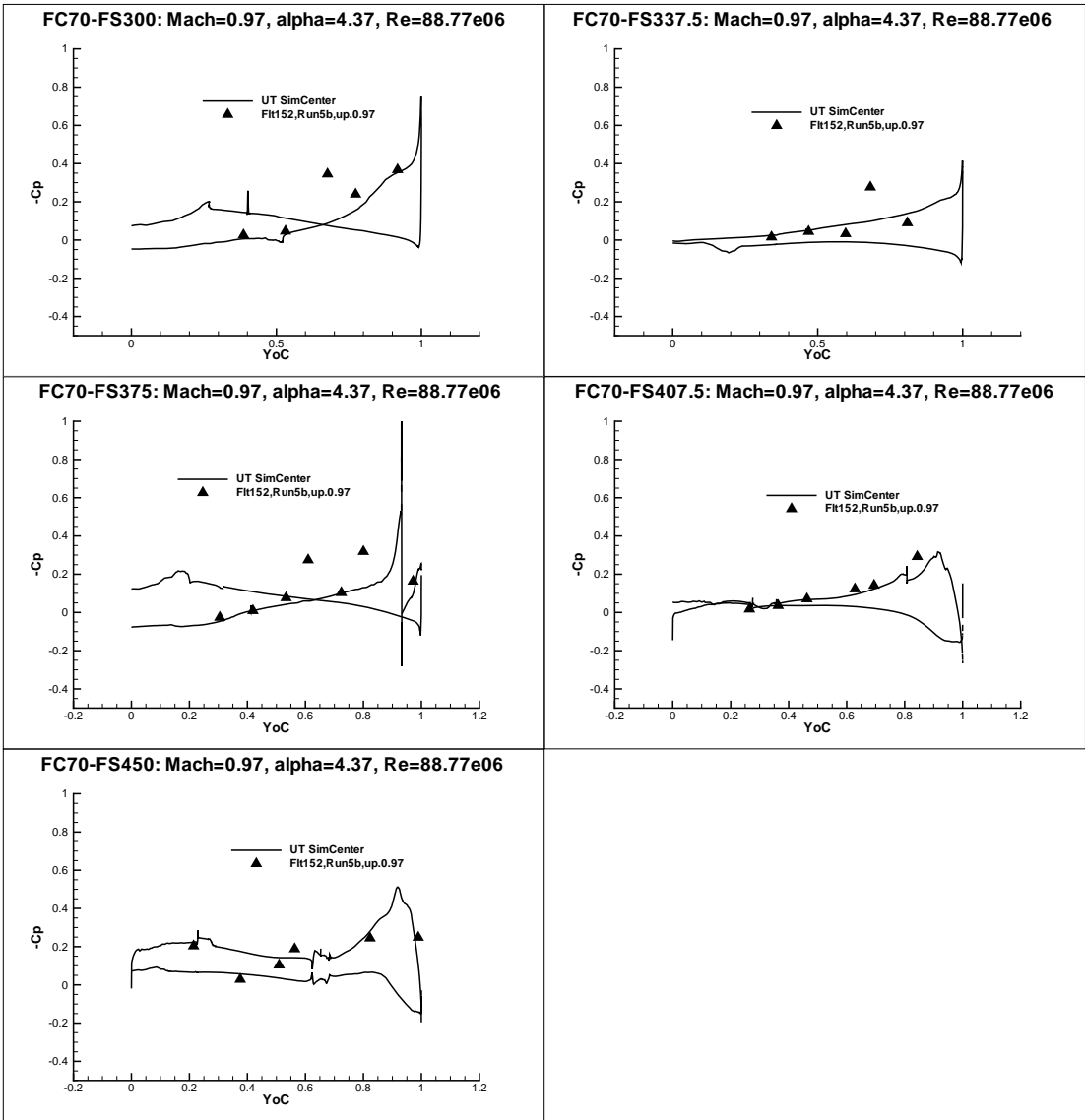
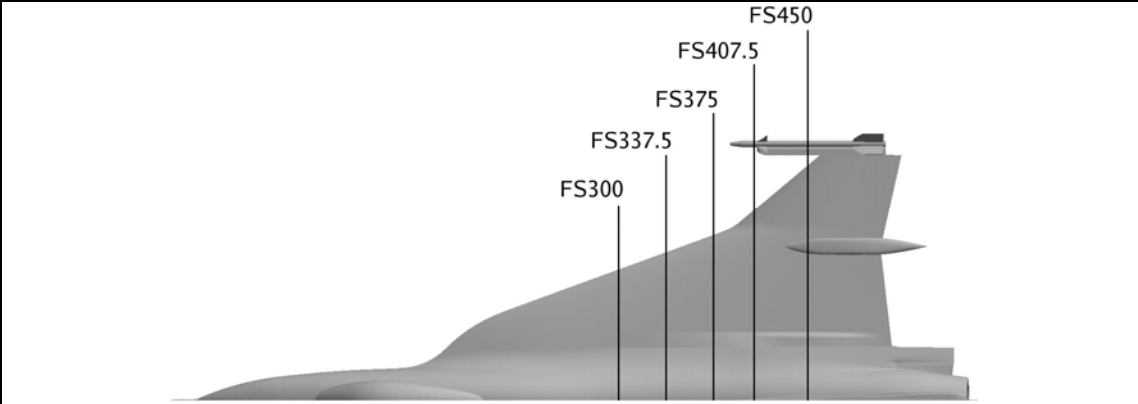
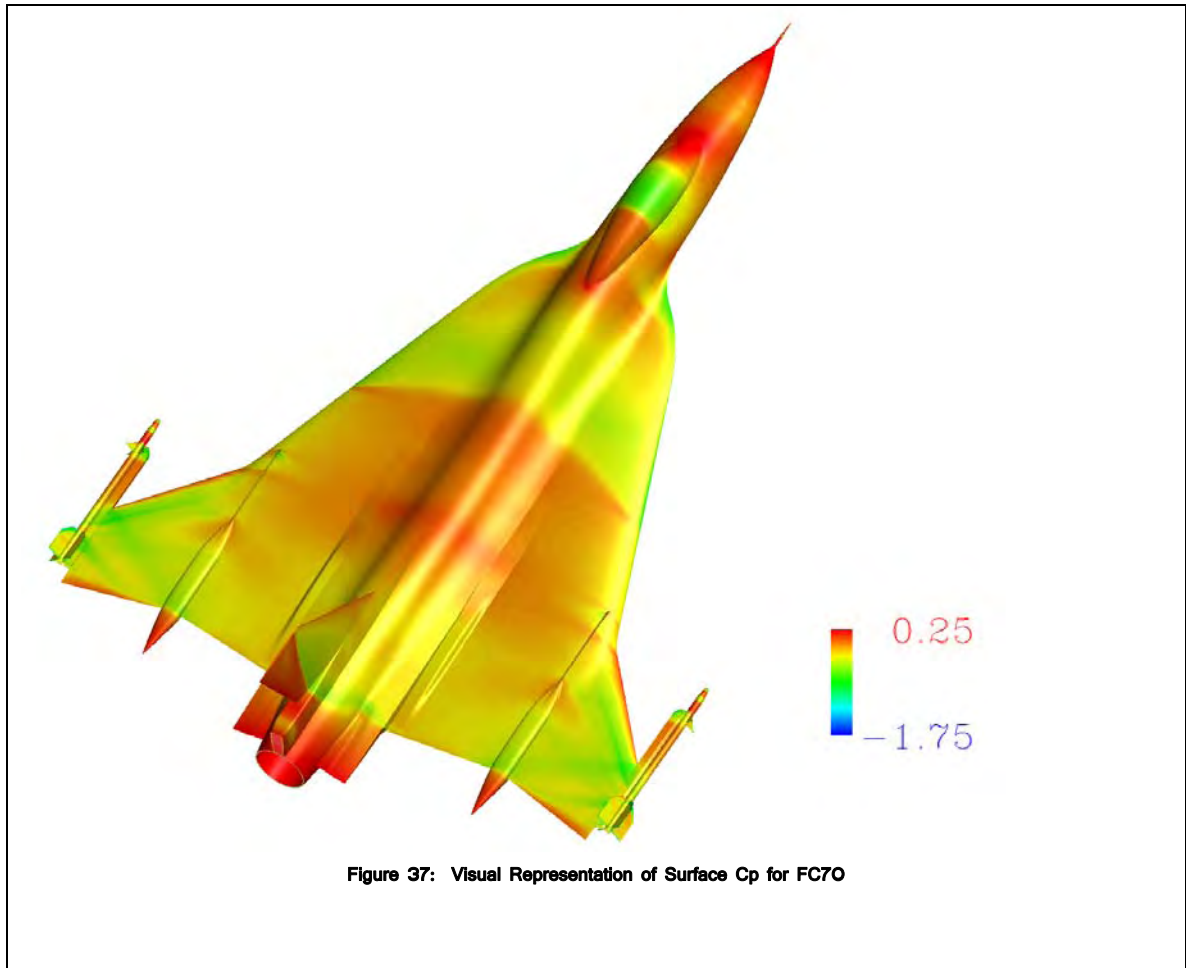


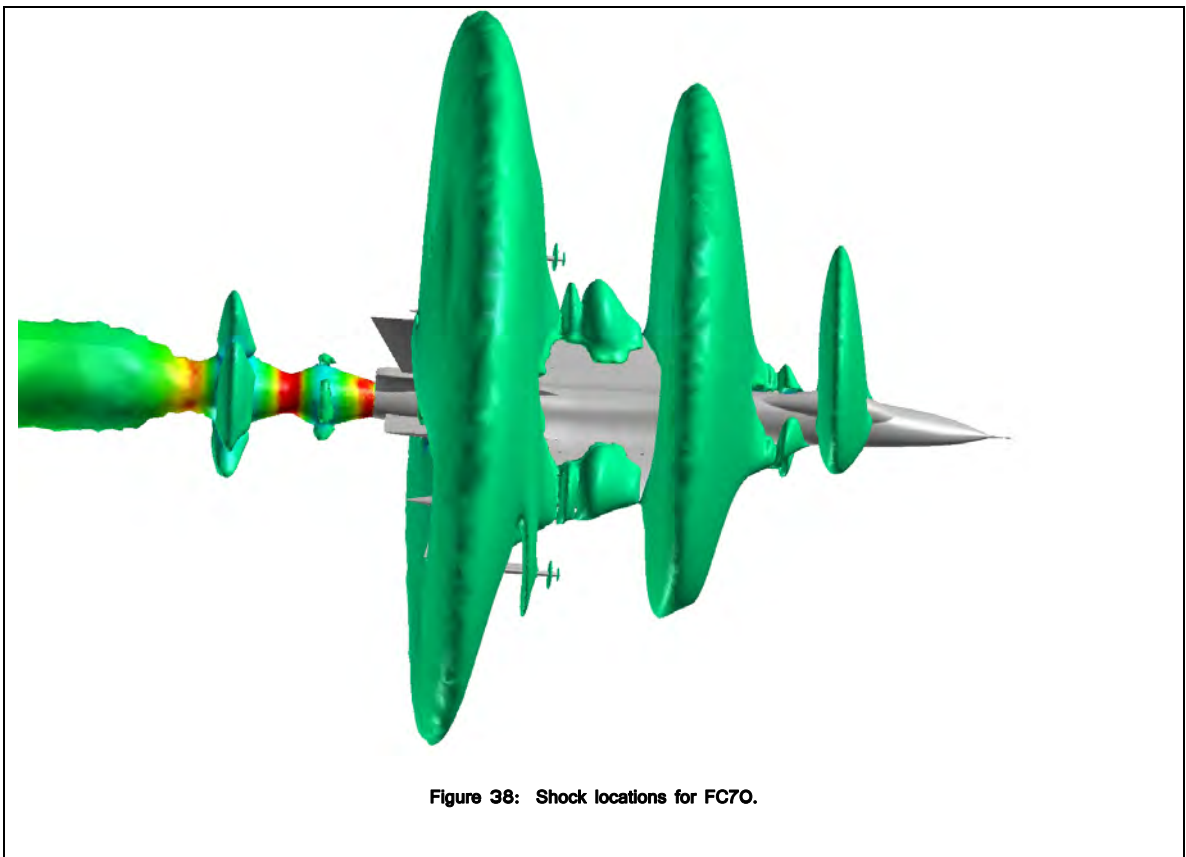
Figure 36: Comparison of Cp along varying FS cuts for FC70.

The plot of surface Cp values is included for the fully configured FC70 geometry (Figure 37).



Despite the increase in stagnation pressures at the nose and canopy, the maximum pressure coefficients observed in FC07 and FC25 are not achieved in FC70. This is primarily due to the much smaller angle of attack ($\alpha = 4.89^\circ$); the effects of which were detailed earlier.

The surface Cp image (Figure 37) shows high Cp striations along the upper surface that could not coincide with stagnation points. These points are the result of shocks developing from the acceleration of airflow around sharp angles or along surfaces with rapidly increasing curvature (Figure 38).



As the transonic airflow reaches the leading edge, a particle taking a path along the upper surface of the wing must travel a greater distance than one traveling along the lower wing surface; yet

these particles must reach the trailing edge simultaneously. The particles initially both have velocities equal to that of the free stream. Thus, the upper particle must accelerate causing it to cross the sonic threshold. Once the fluid makes the turn past the geometry change, it decelerates to match the velocity of the lower surface particle at the leading edge. The physical mechanism for this deceleration is a normal shock wave. The normal shock represents a discontinuity between the high velocity and low pressure of the fluid at sonic speeds and the lower velocity high pressure fluid after deceleration back to free stream velocity. Thus, there is a large jump or instantaneous change to fluid properties across the shock.

Each time the fluid encounters a change in curvature of the aircraft it again accelerates through the turn and decelerates past the turn by forming a normal shock wave. Normal shocks develop anywhere along the surface of the aircraft where the curvature increases at a rate great enough to accelerate the airflow past the sonic threshold (i.e., the leading edge, the canopy, the vertical tail).

5.0 Conclusions

The overall agreement between the CFD and EFD data was quite good. The CFD did fail to predict the minimum pressures for all FC's, but captured the maximum pressures in most cases. One reason for the failure to predict the minimum pressures is that the model is not accurately representing vorticity in these regions. The velocities at vortex cores are being under-approximated along the path as a result of dissipation. This discrepancy between actual and modeled fluid velocity accounts for the failure to predict minimum pressures in regions of high vorticity.

The maximum C_p values predicted for FC25 were the highest of all FCs. This is due to the extreme angle of attack bringing the lower surface of the leading edge into a more pronounced opposition to the flow stream. The minimum C_p values were also observed in FC25 and are again related to higher fluid velocities due to the angle of attack. The higher fluid velocity prior to the development of vortices leads to higher fluid velocities at vortex cores. This causes increased vorticity magnitude at the cores. Similar phenomena with less magnitude are also observed for FC07.

Although the CFD data agree well with the EFD data, it is possible this agreement could be increased by

including the leading edge deflectors in the model. Additional mesh refinement (tighter spacing between mesh points) should also decrease the variance between the CFD and EFD data. A mesh refinement study was not included in this examination but would provide further validation of the unstructured solver by providing for the possibility of a solution that is completely independent of the mesh spacing; that said, the results are more than sufficient to validate the ability of the computational model to reasonably predict flow phenomena and their locations for the complex F-16XL geometry.

Appendices

A. References

1. Wikipedia, F-16XL, <http://en.wikipedia.org/wiki/F-16XL>
2. NASA Dryden Research Center, URL: <http://www.nasa.gov/centers/dryden/home>
3. Aerial Archive, Introduction to Photogrammetry, <http://www.univie.ac.at/Luftbildarchiv/wqv/intro.htm>.
4. Lamar, J. E., Obara, C. J., Fisher, B. D., Fisher, D. F., "Flight, Wind-Tunnel, and Computational Fluid Dynamics Comparison for Cranked Arrow Wing (F-16XL-1) at Subsonic and Transonic Speeds," NASA Langley and NASA Dryden Research Centers.
5. Pointwise, Inc., Gridgen User Manual, version 15, <http://www.pointwise.com>.
6. Karman, S. L. Jr., "Unstructured Viscous Layer Insertion Using Linear-Elastic Smoothing," AIAA-2006-0531, January 2006.
7. Intelligent Light, Inc., URL: <http://www.ilight.com>.
8. Autodesk, Inc., URL: <http://usa.autodesk.com>.
9. Anderson, W. K., 1992 "Grid Generation and Flow Solution Method for the Euler Equations on Unstructured Grids," Tech. Rep. L-16986, NASA Langley Research Center, Hampton, VA 23665-5225.
10. Swafford, Tim, 2006 Class Notes: Computational Fluid Dynamics
11. Tannehill, J. C., Anderson, D. A., Pletcher, R. H., 1997, Computational Fluid Mechanics and Heat Transfer, 2nd edition.
12. Briley, W. R., McDonald, H., "Solutions of the Three-Dimensional Compressible Navier-Stokes Equations by an Implicit Technique," Lecture Notes in Physics, Vol.35, Springer—Verlag, New York, NY.

13. Crowe, C. T., Elger, D. F., Roberson, J. A., 2001, Engineering Fluid Mechanics, 7th edition.
14. Wikipedia, Laminar vs. Turbulent Flow,
http://en.wikipedia.org/wiki/Fluid_dynamics
15. White, F. M., 1991 Viscous Fluid Flow, 2nd ed., McGraw-Hill, New York, NY.
16. Karypis Lab, METIS - Serial Graph Partitioning and Fill-reducing Matrix Ordering, URL: <http://glaros.dtc.umn.edu/gkhome/views/metis>
17. Hyams, D.G., Sreenivas, K., Sheng, C., Briley, W. R., Marcum, D. L., and Whitfield, D. L., 2000 "An Investigation of Parallel Implicit Solution Algorithms for Incompressible Flows on Multielement Unstructured Topologies", AIAA 2000-0271.
18. Tecplot, Inc., URL: <http://www.tecplot.com>.

B. Additional Figures

Figure 39: Comparison of Cp along BL55 for Flight Case O7.

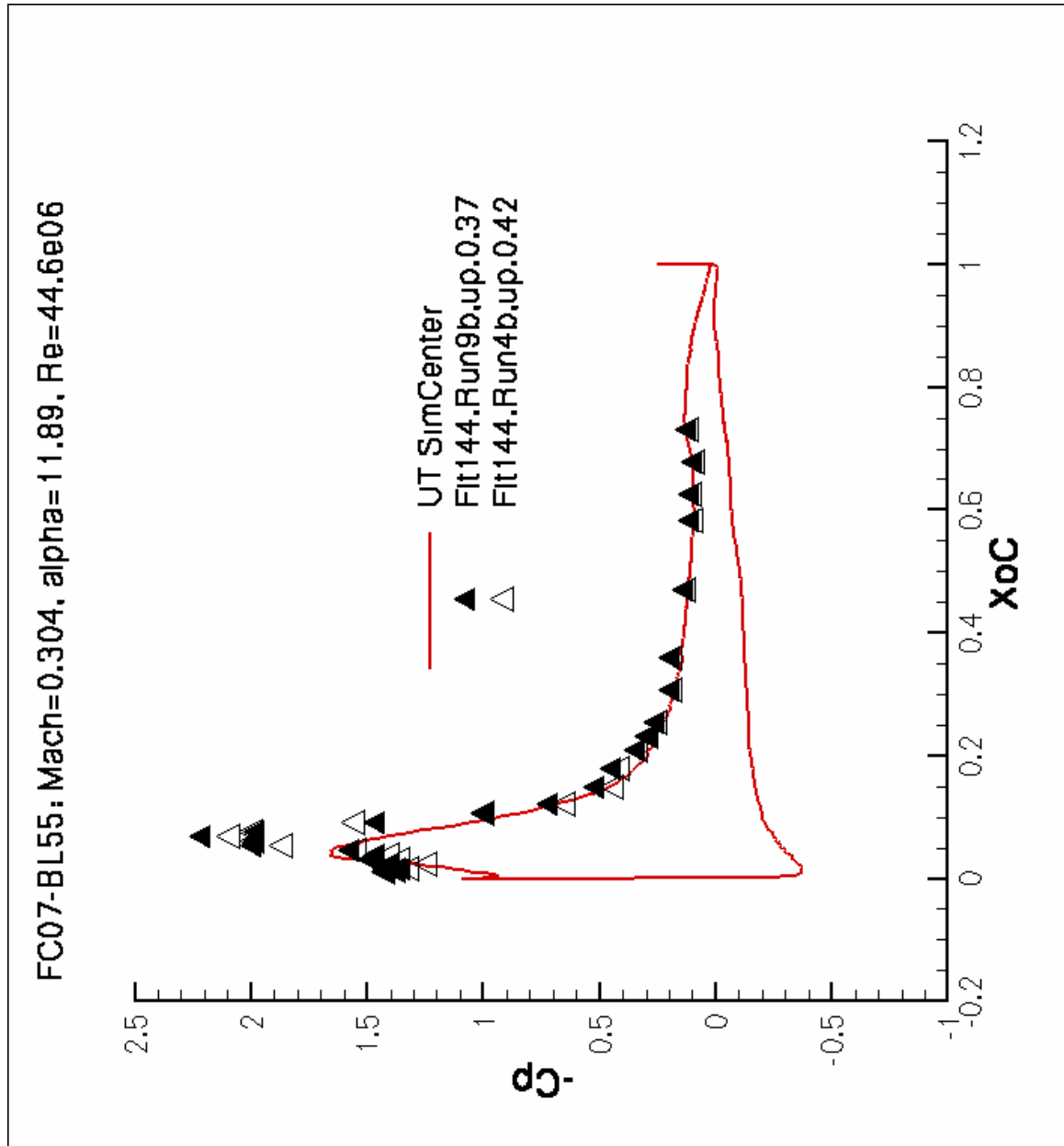


Figure 40: Comparison of Cp along BL70 for Flight Case O7.

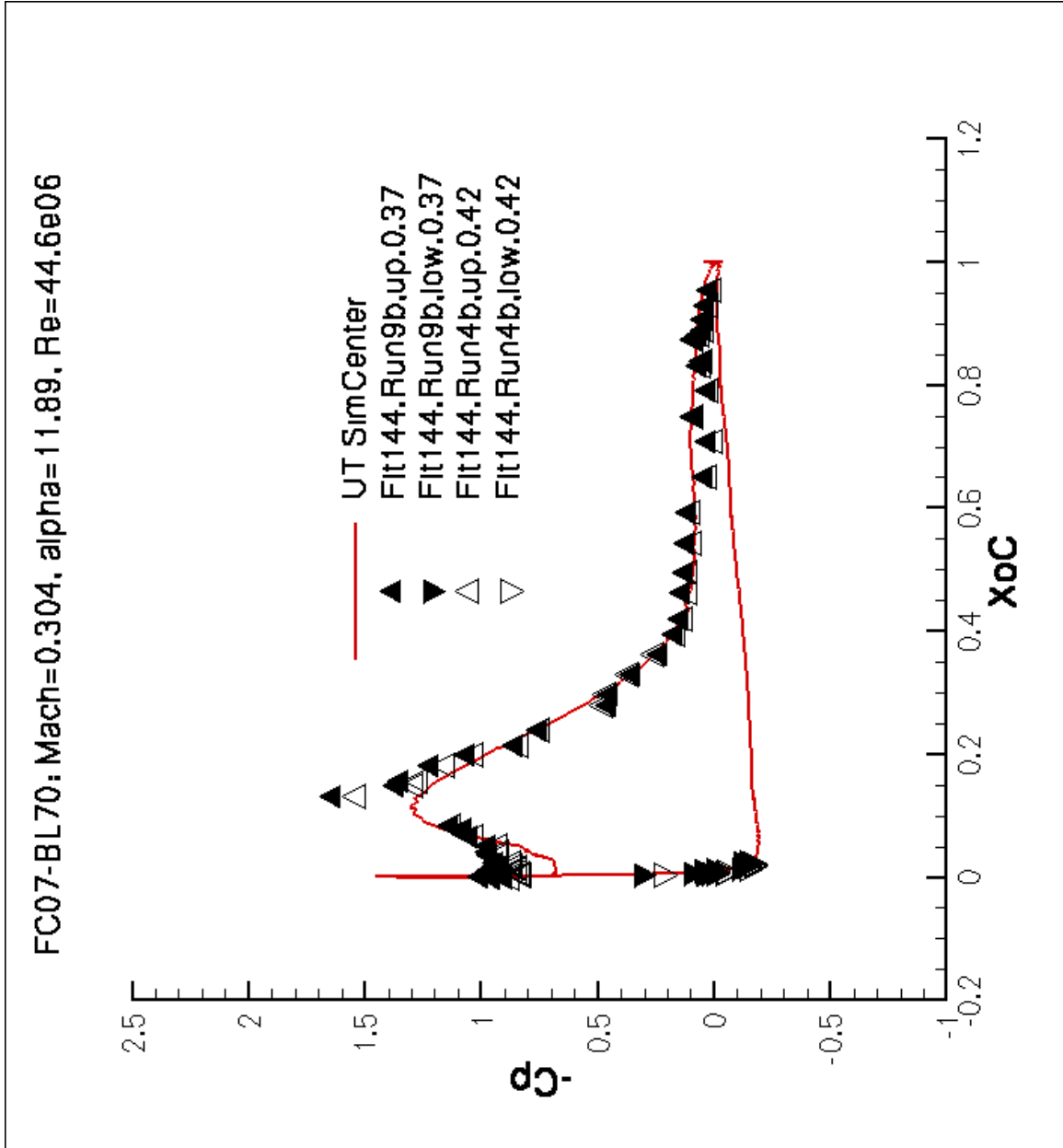


Figure 41: Comparison of Cp along BL80 for Flight Case O7.

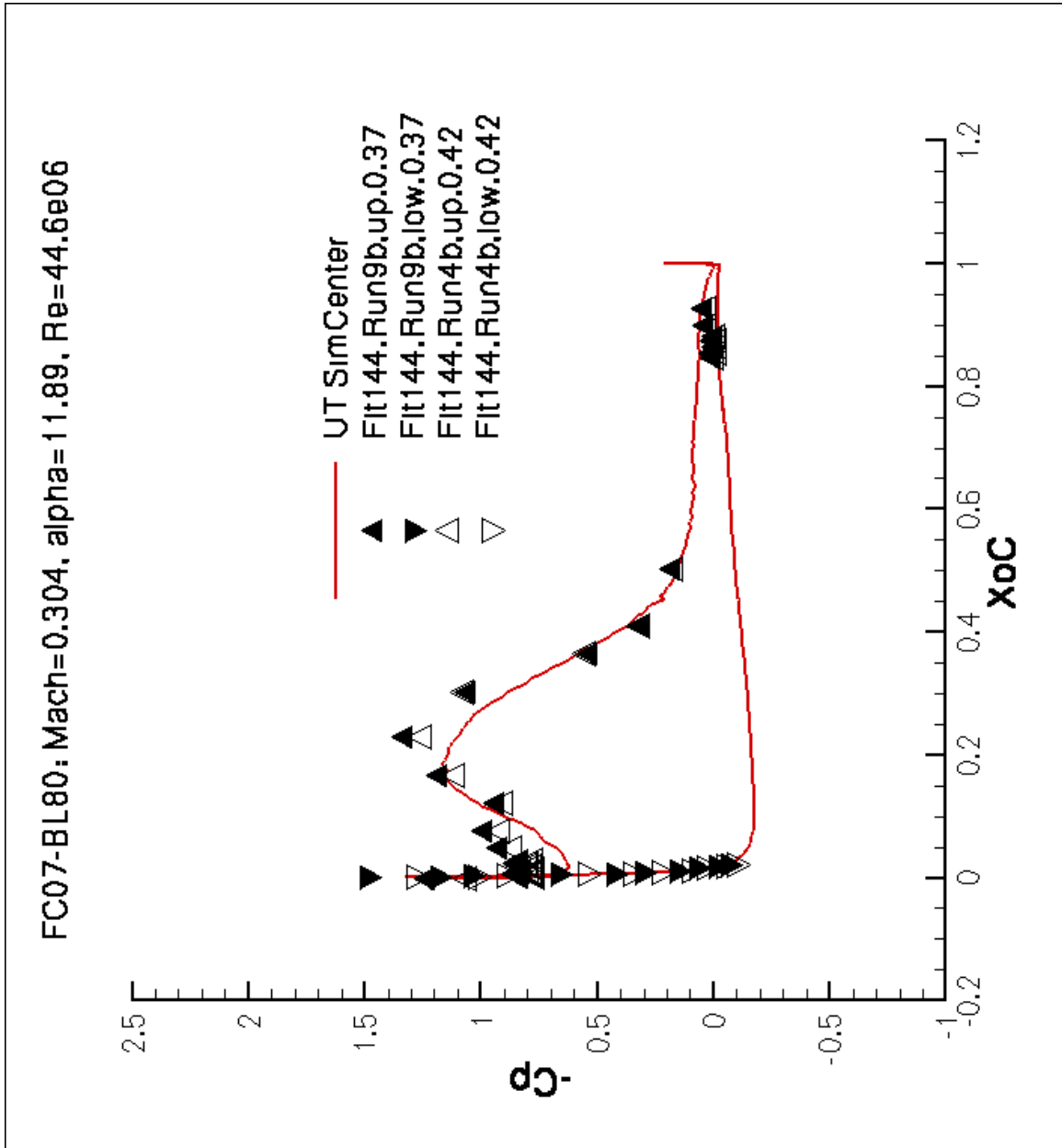


Figure 42: Comparison of Cp along BL95 for Flight Case O7.

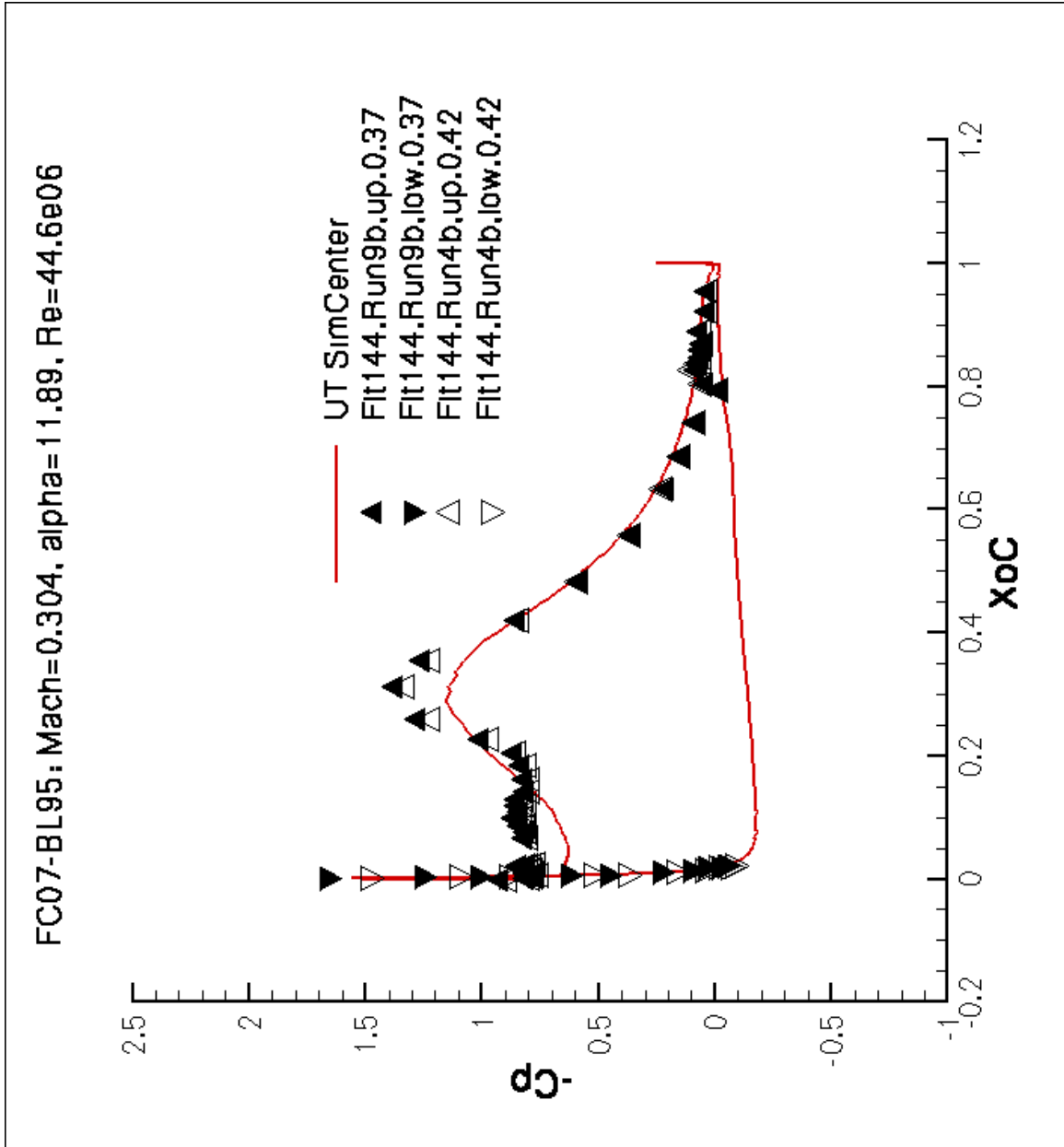


Figure 43: Comparison of Cp along BL153.5 for Flight Case O7.

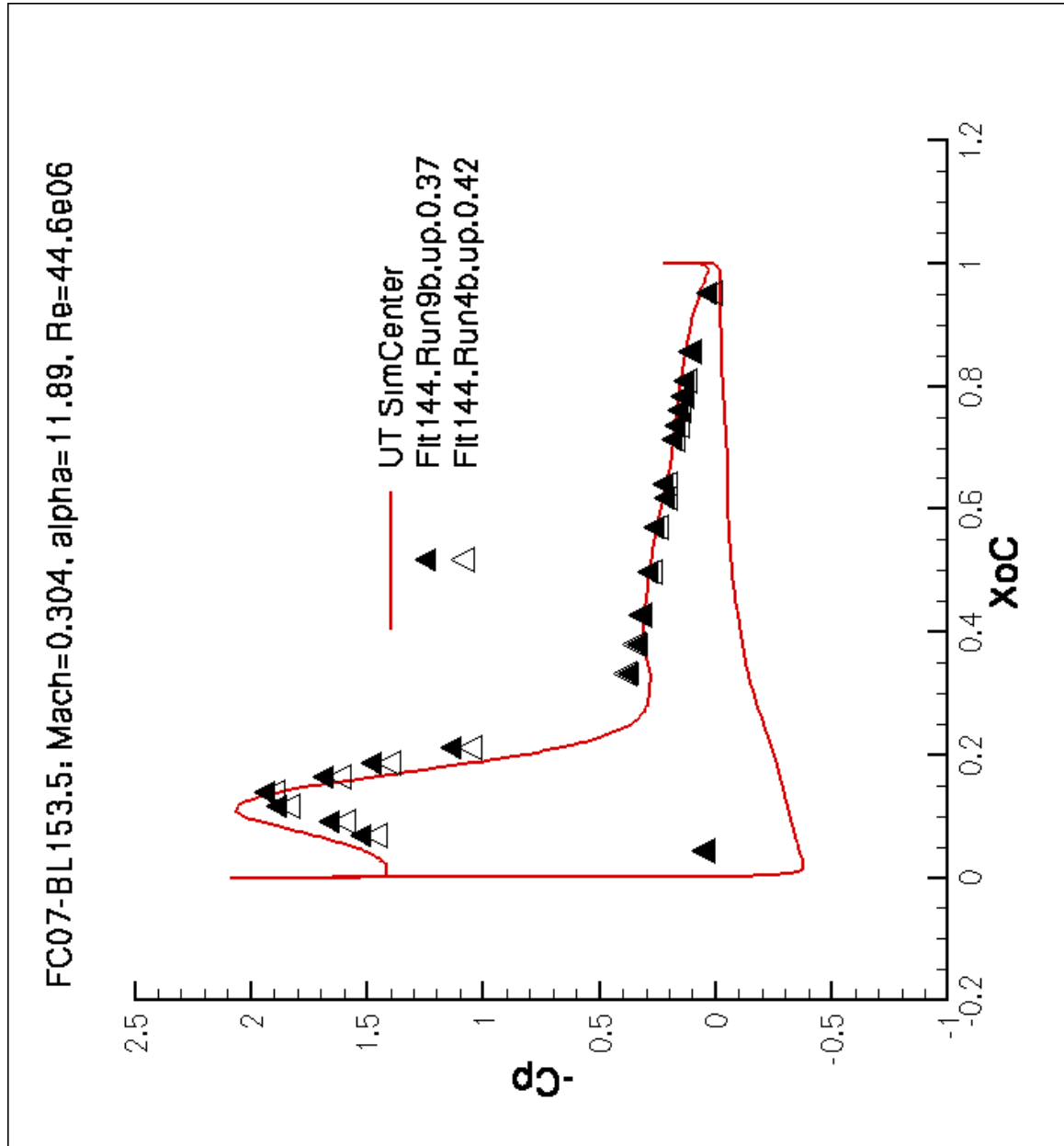


Figure 44: Comparison of Cp along BL184.5 for Flight Case O7.

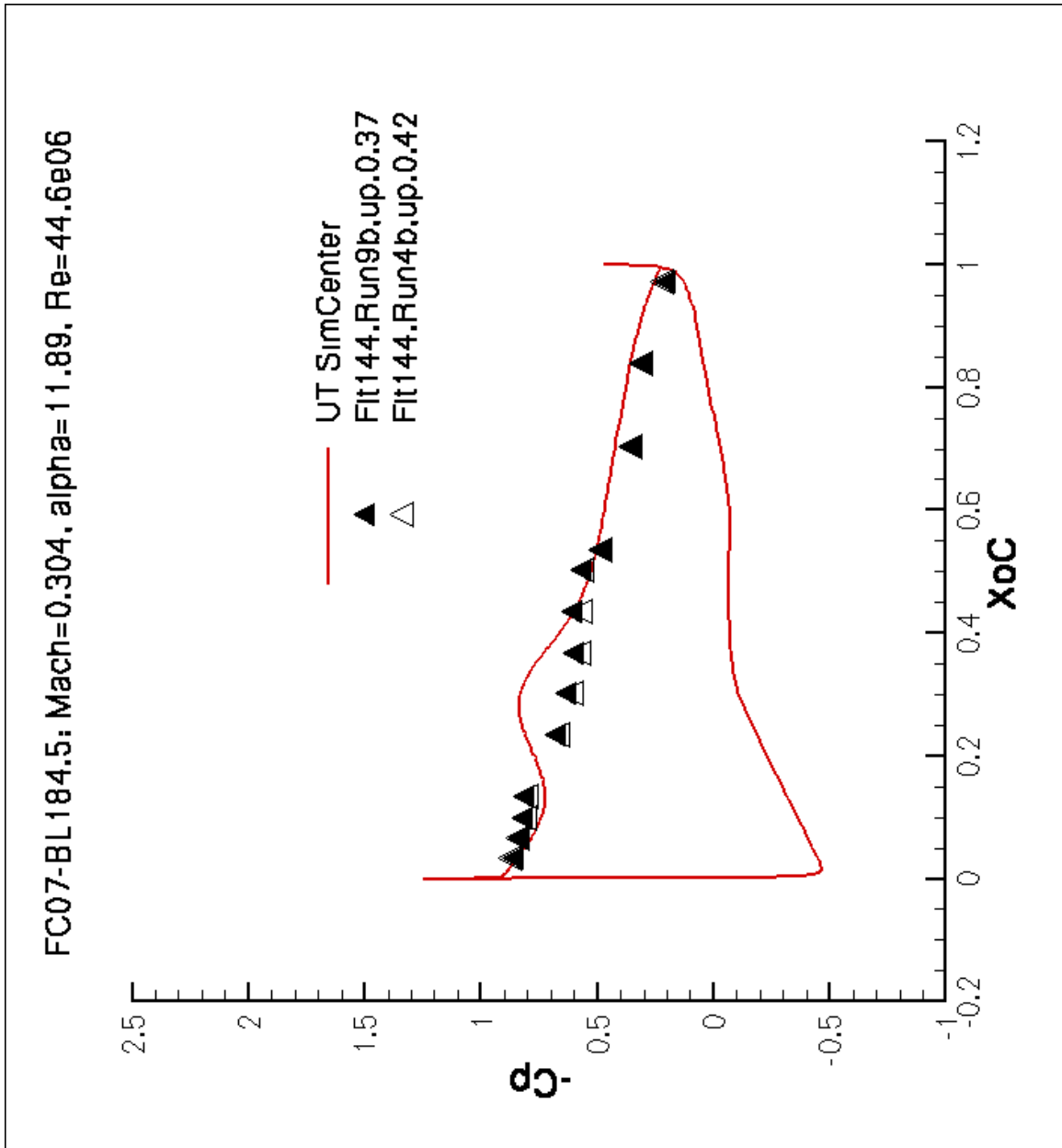


Figure 45: Comparison of Cp along FS300 for Flight Case O7.

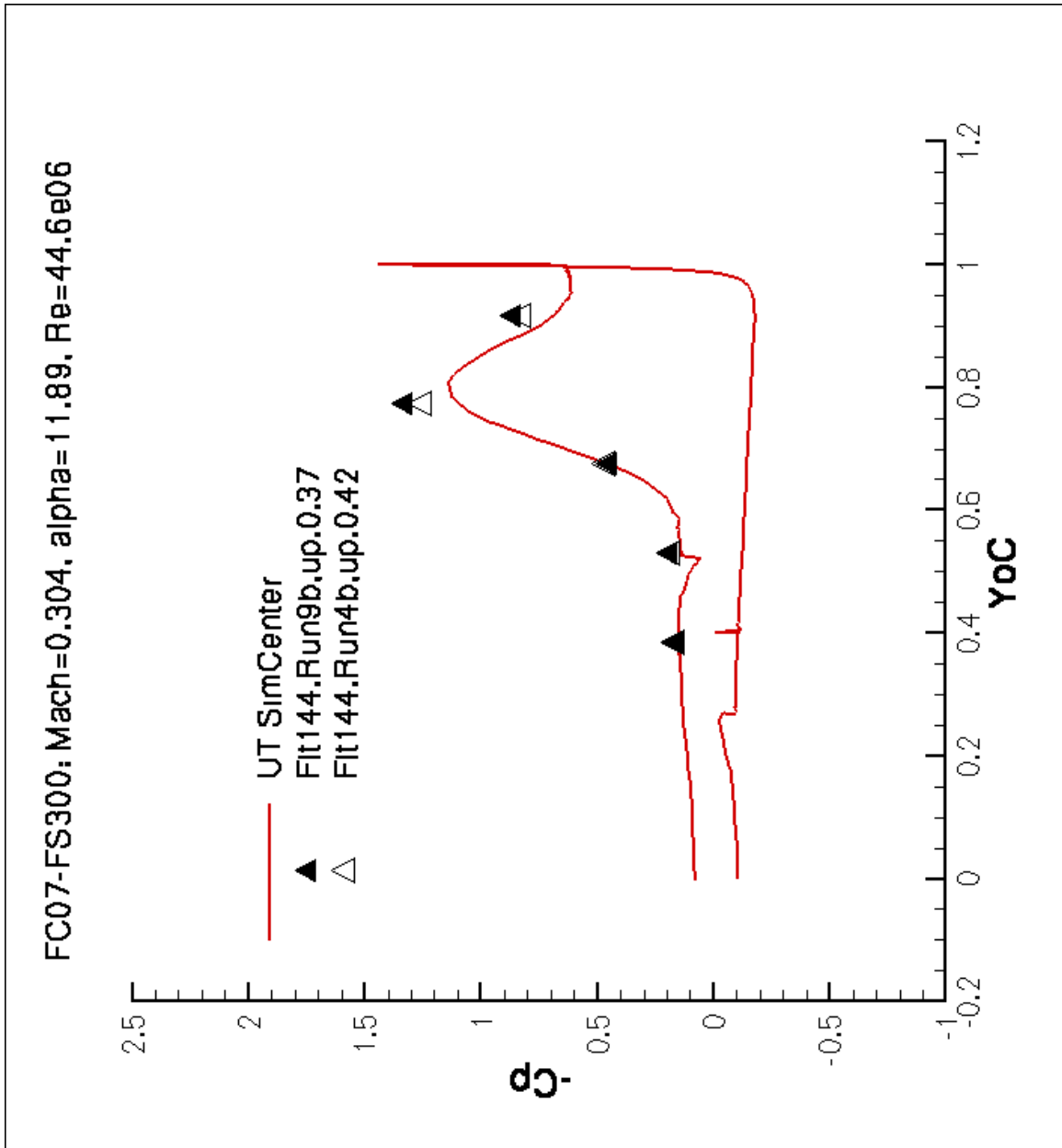


Figure 46: Comparison of Cp along FS337.5 for Flight Case O7.

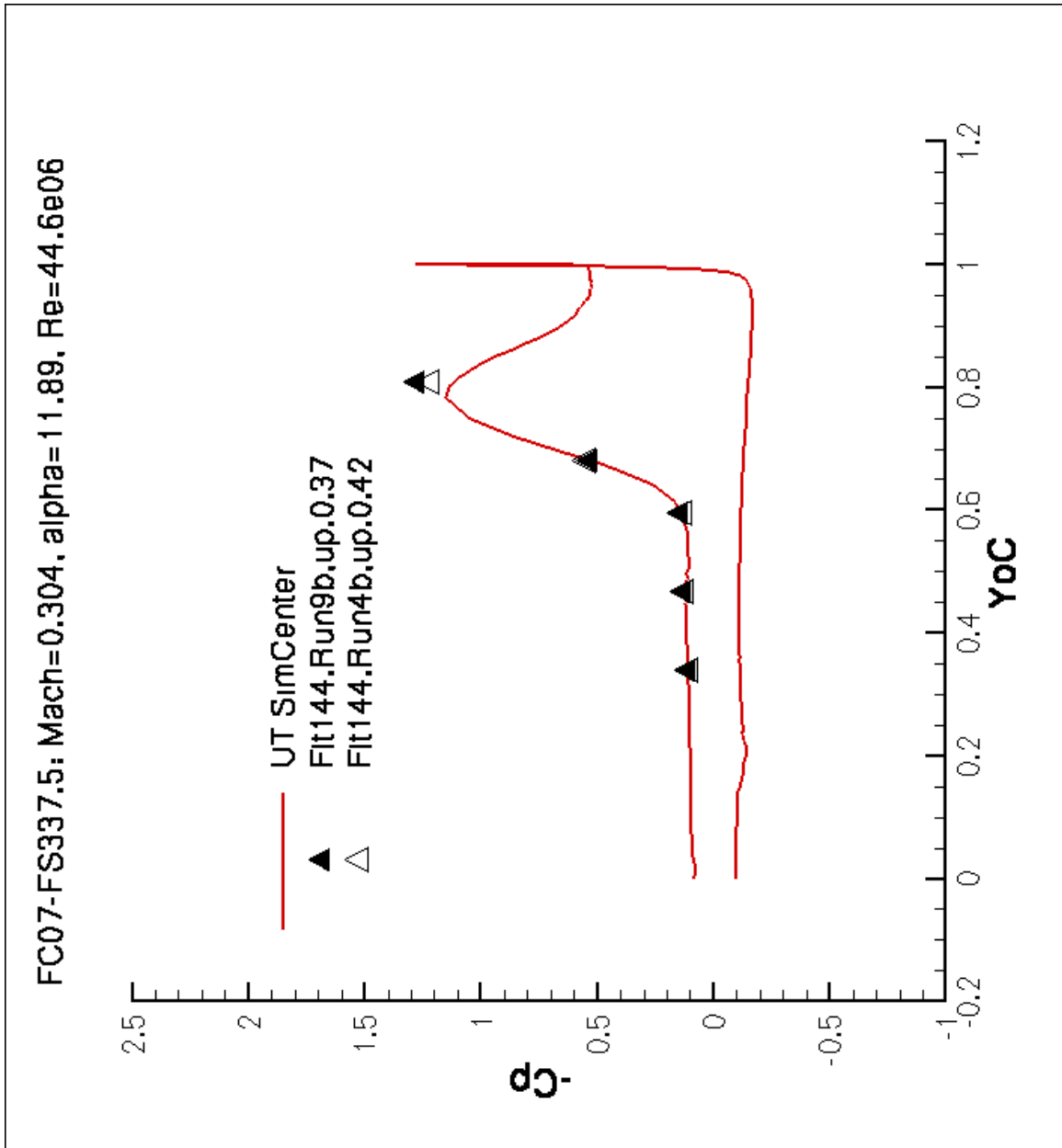


Figure 47: Comparison of C_p along FS375 for Flight Case 07.

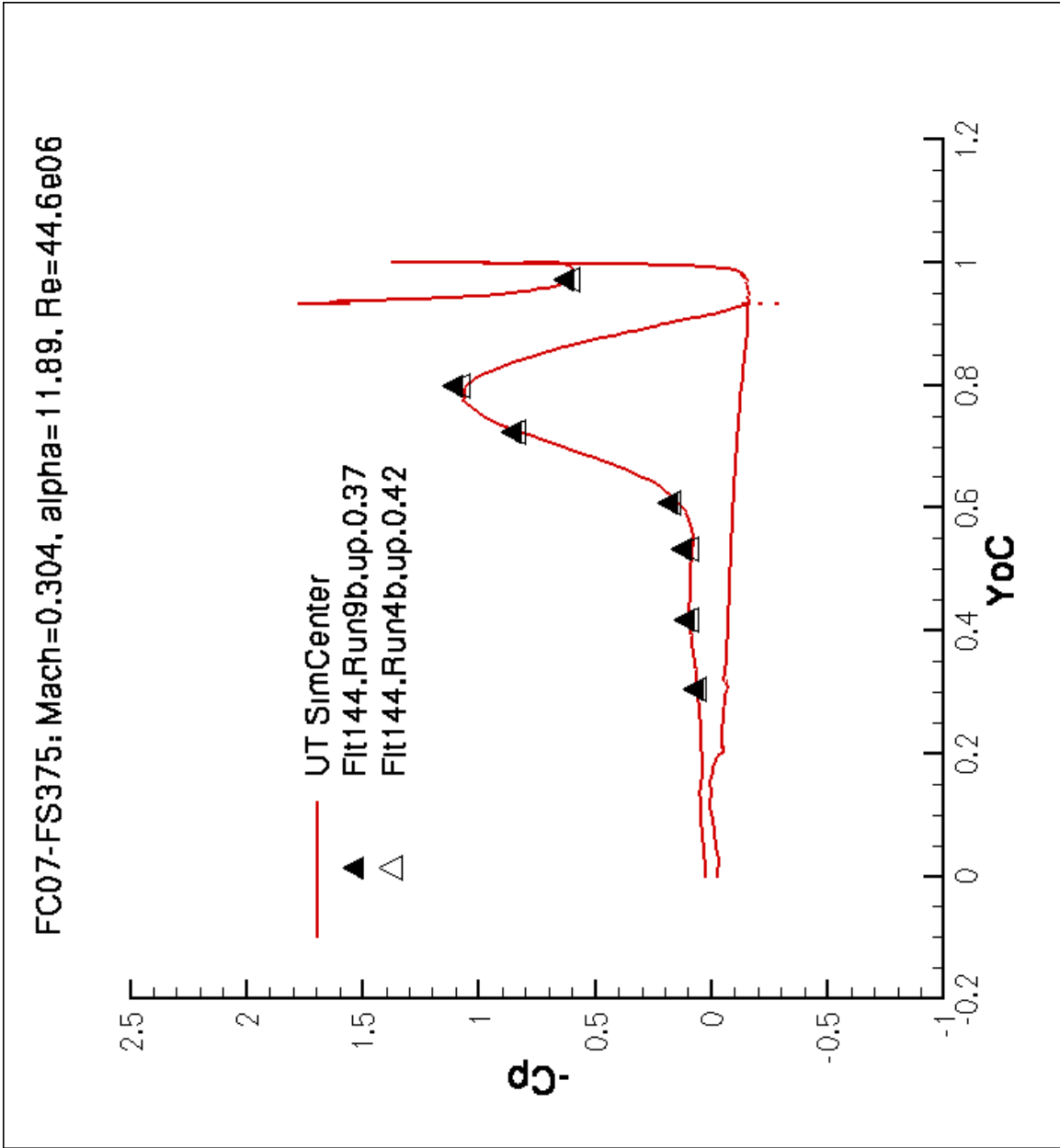


Figure 48: Comparison of Cp along FS407.5 for Flight Case 07.

FC07-FS407.5: Mach=0.304, alpha=11.89, Re=44.6e06

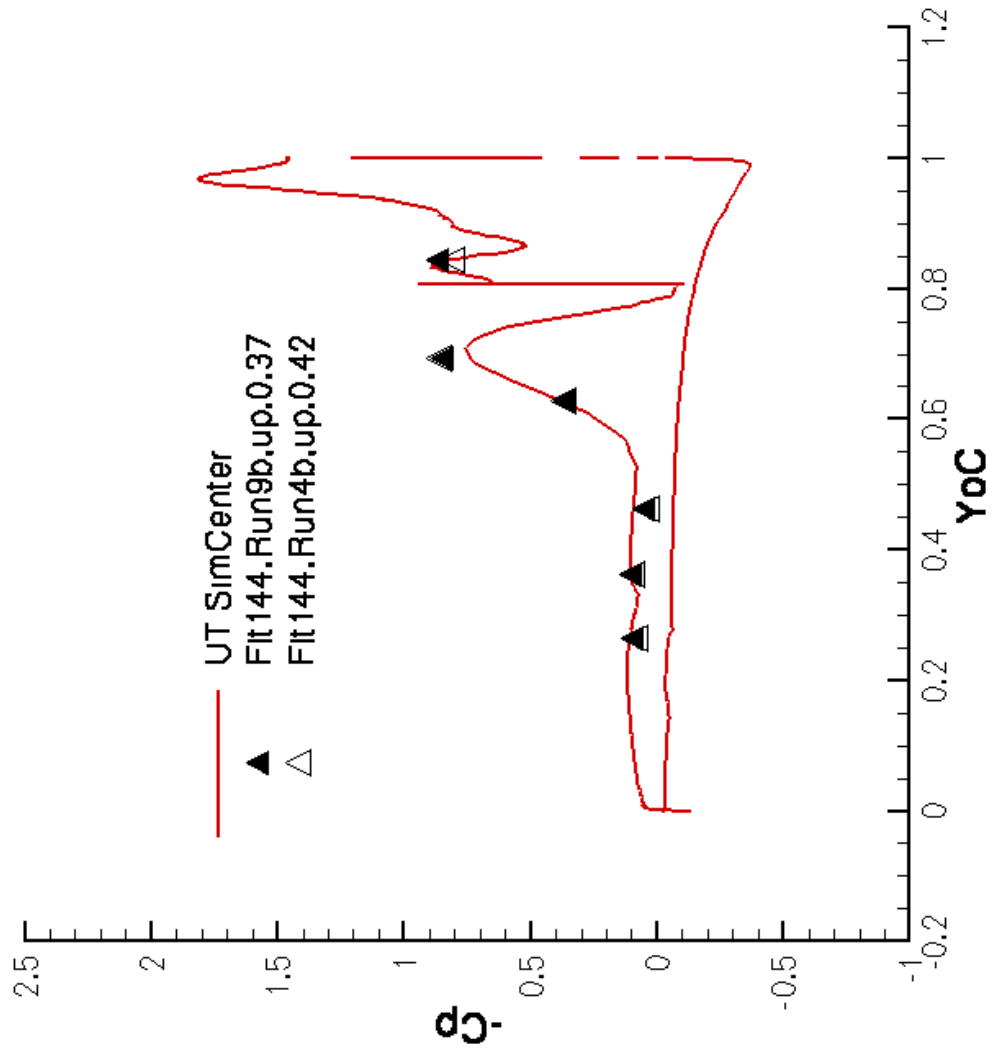


Figure 49: Comparison of Cp along FS450 for Flight Case O7.

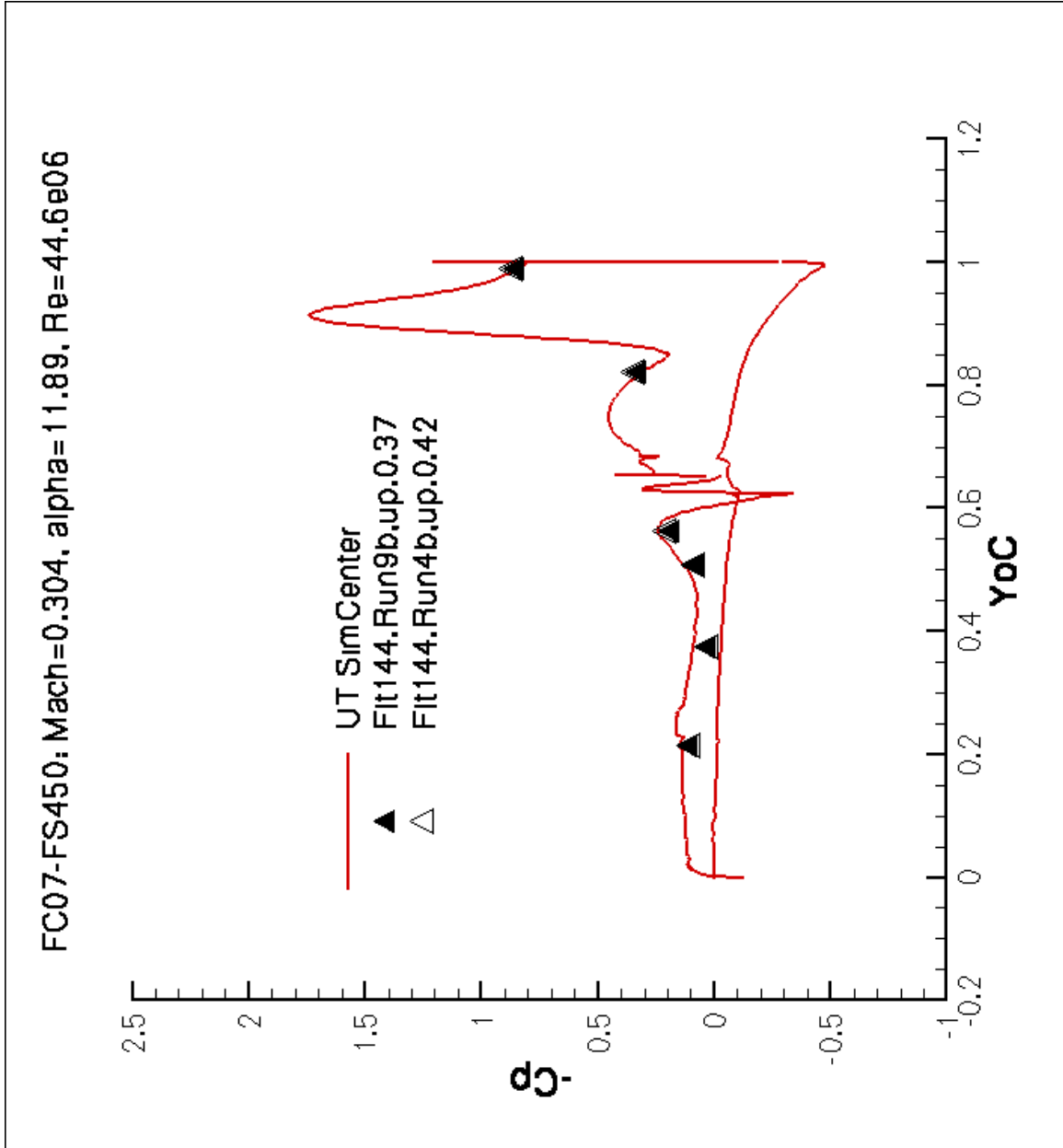


Figure 50: Comparison of Cp along BL55 for Flight Case 25.

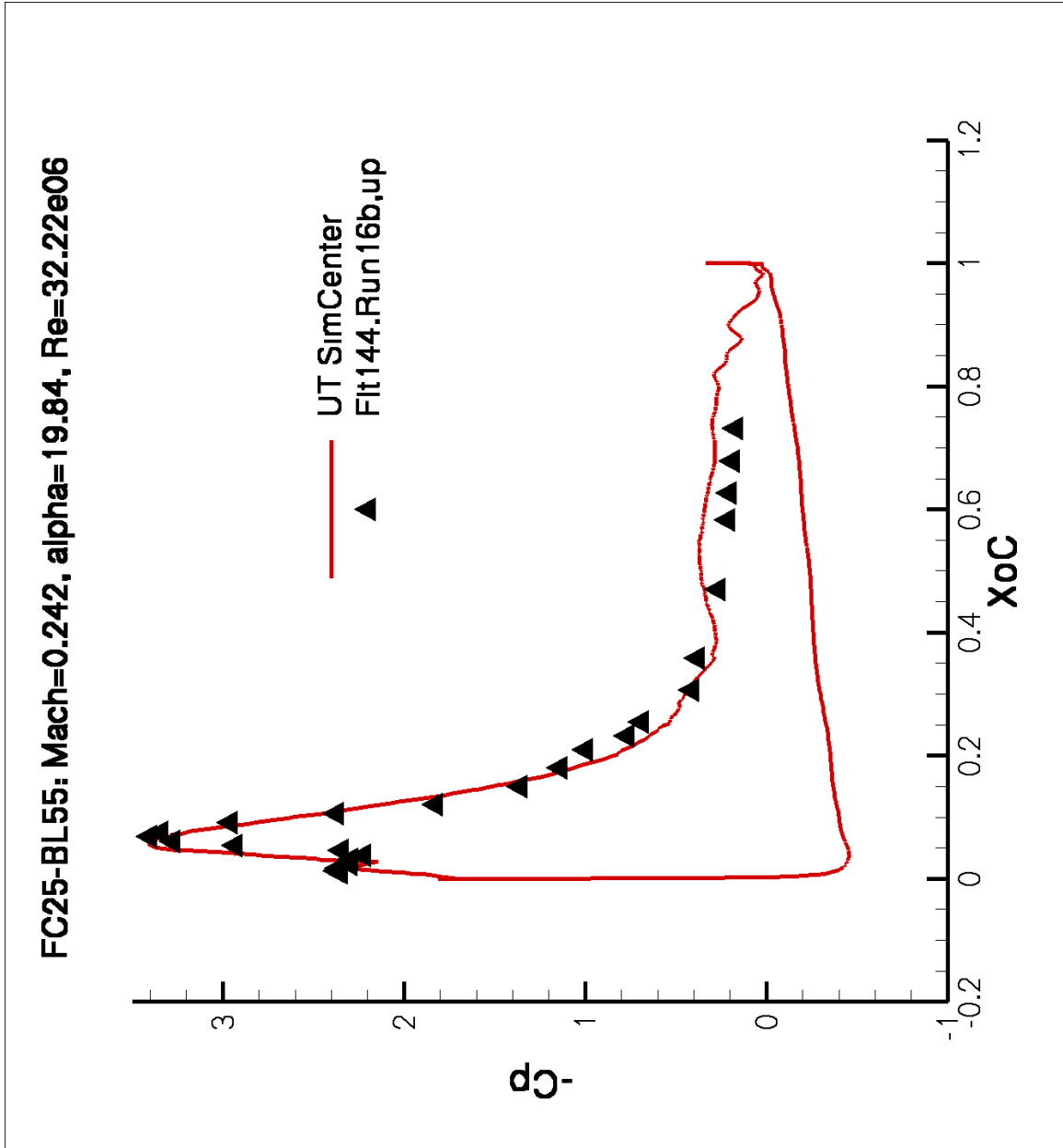


Figure 51: Comparison of Cp along BL70 for Flight Case 25.

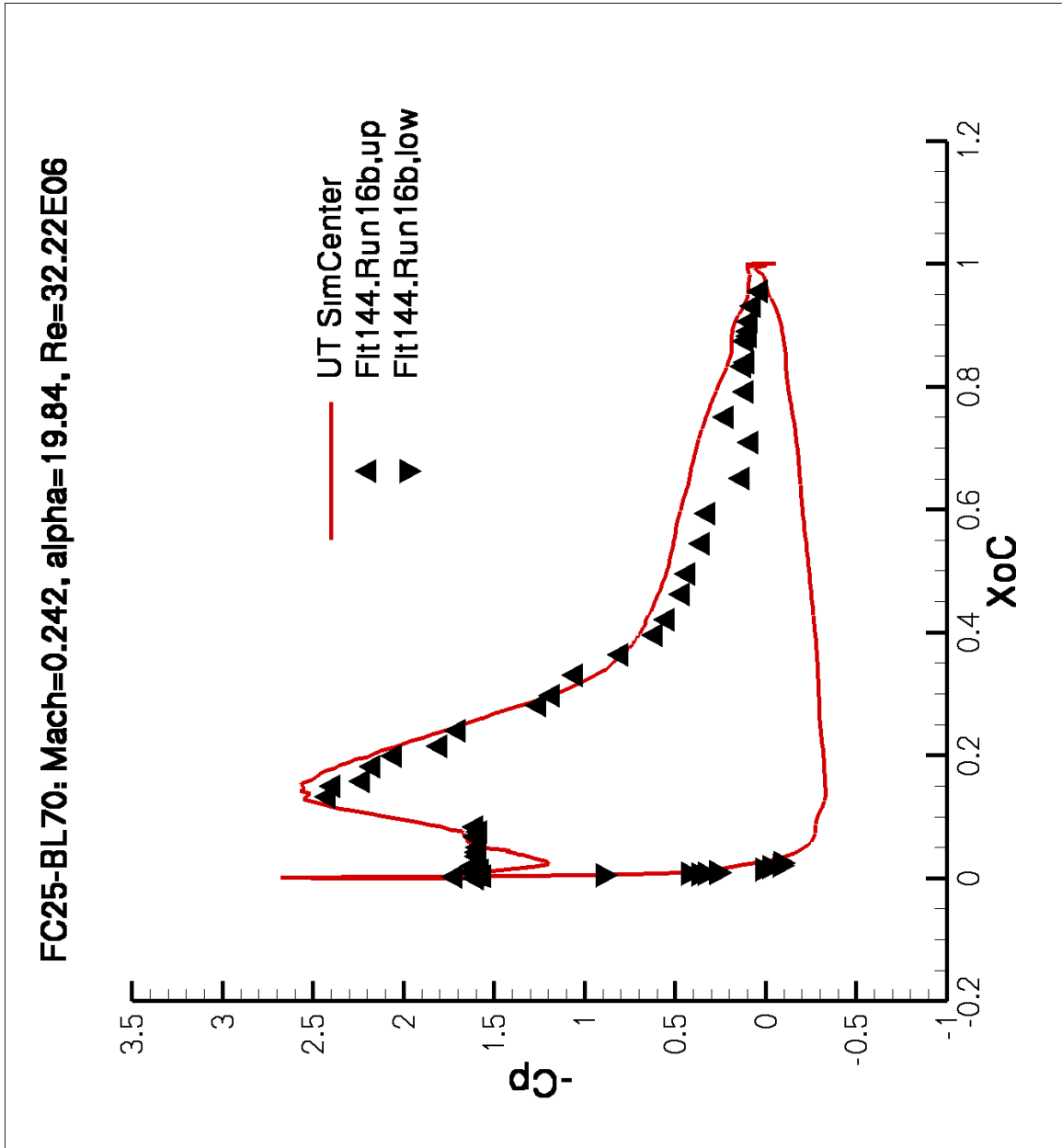


Figure 52: Comparison of Cp along BL80 for Flight Case 25.

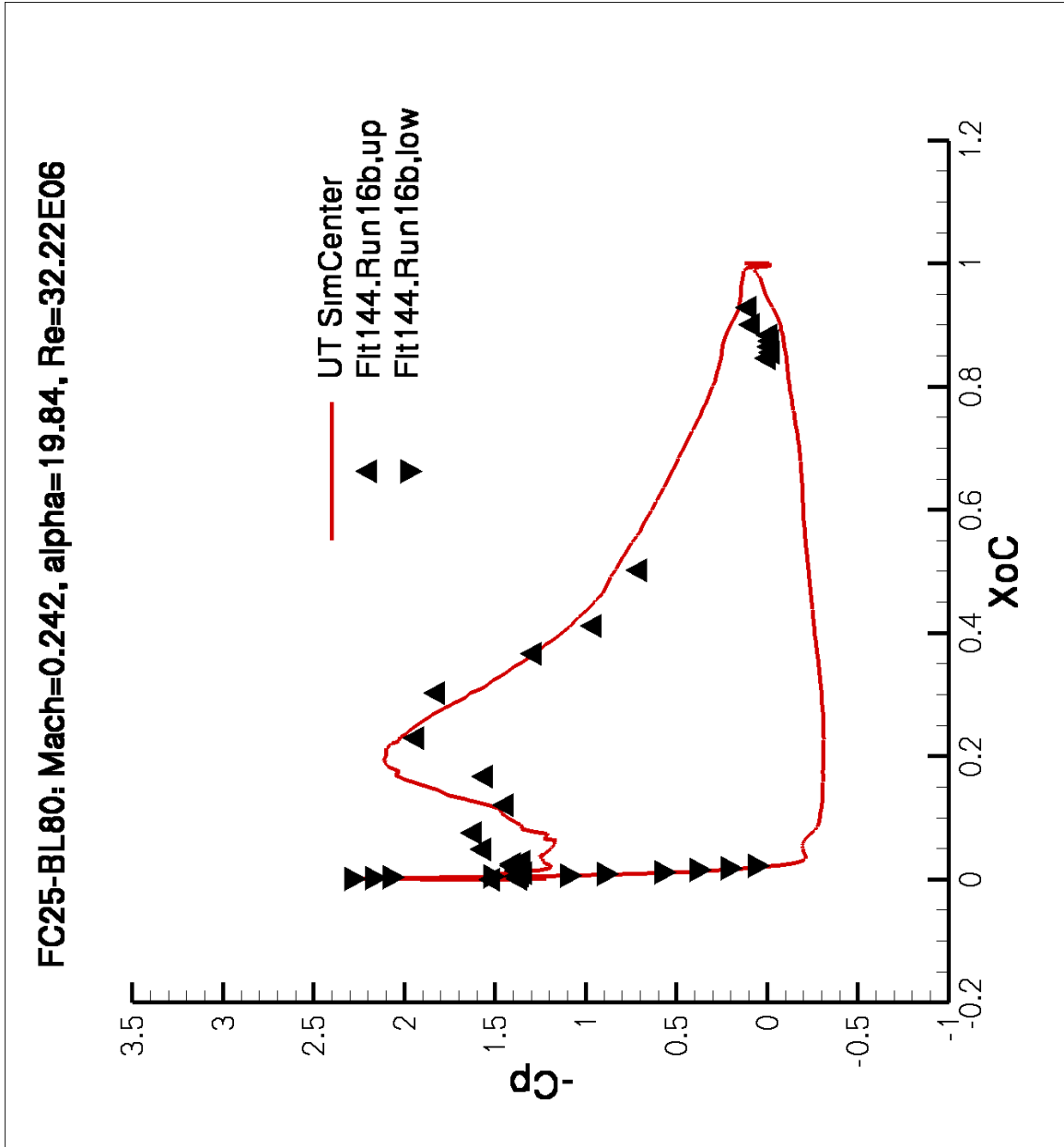


Figure 53: Comparison of Cp along BL95 for Flight Case 25.

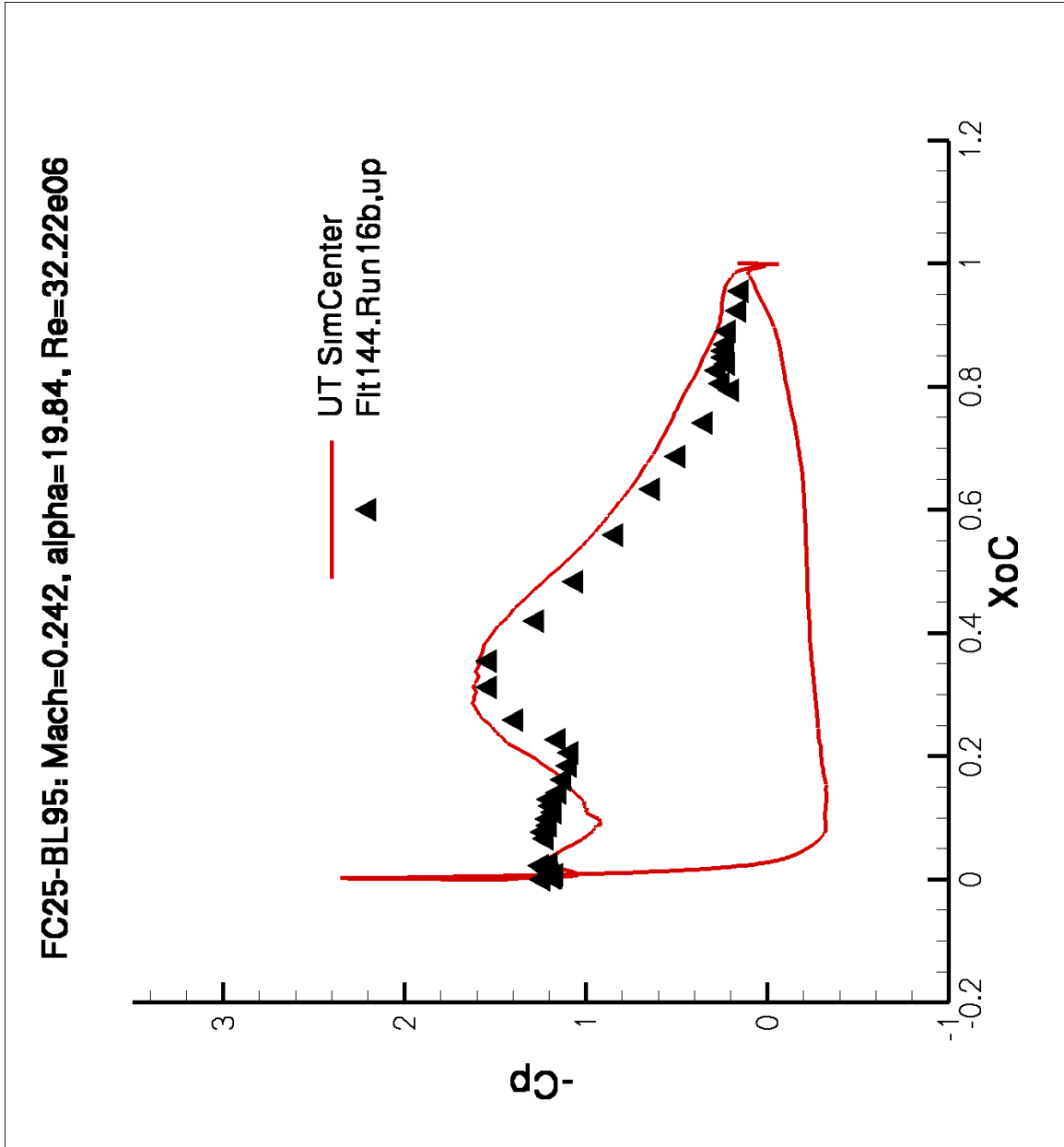


Figure 54: Comparison of Cp along BL153.5 for Flight Case 25.

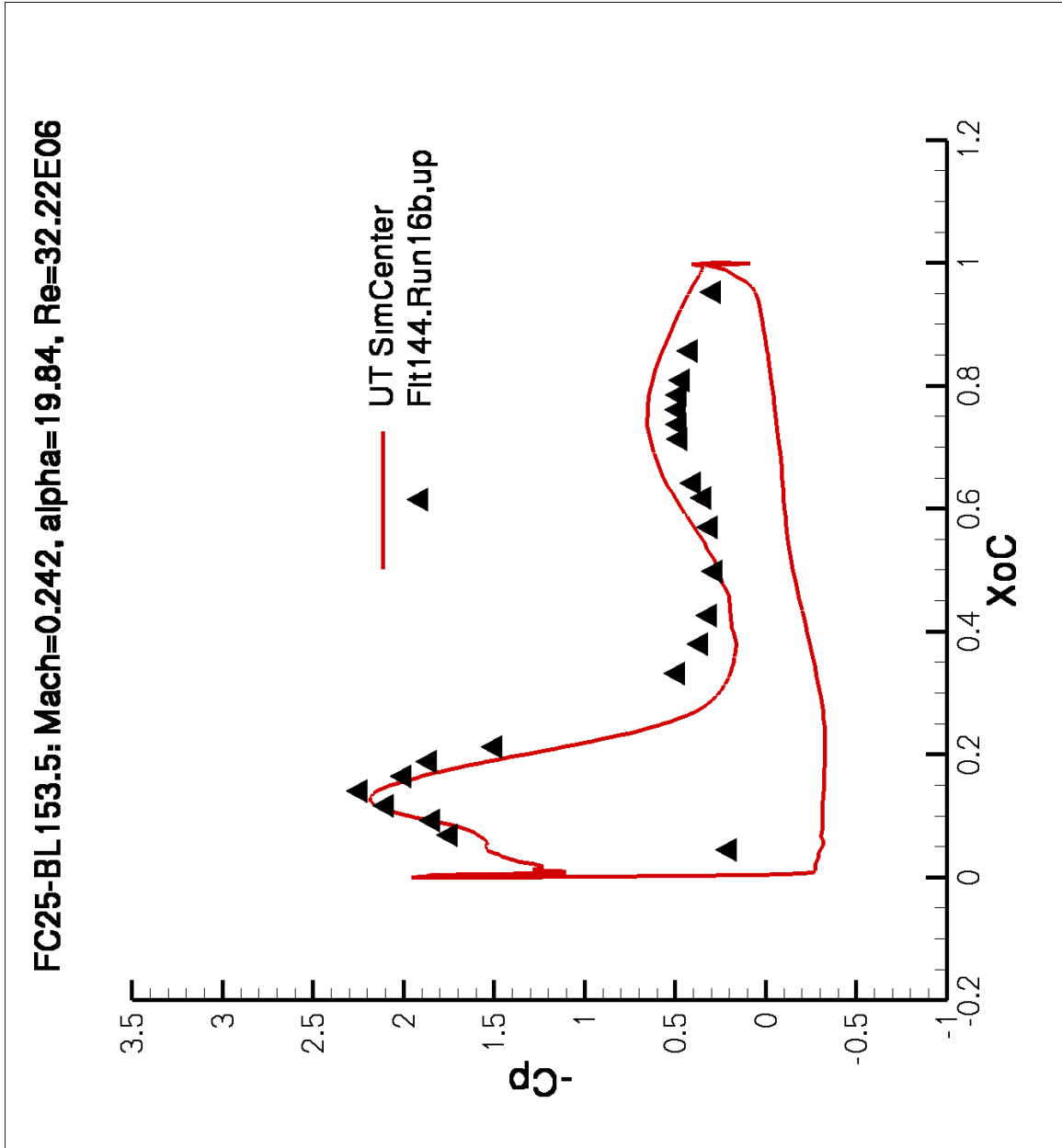


Figure 55: Comparison of Cp along BL184.5 for Flight Case 25.

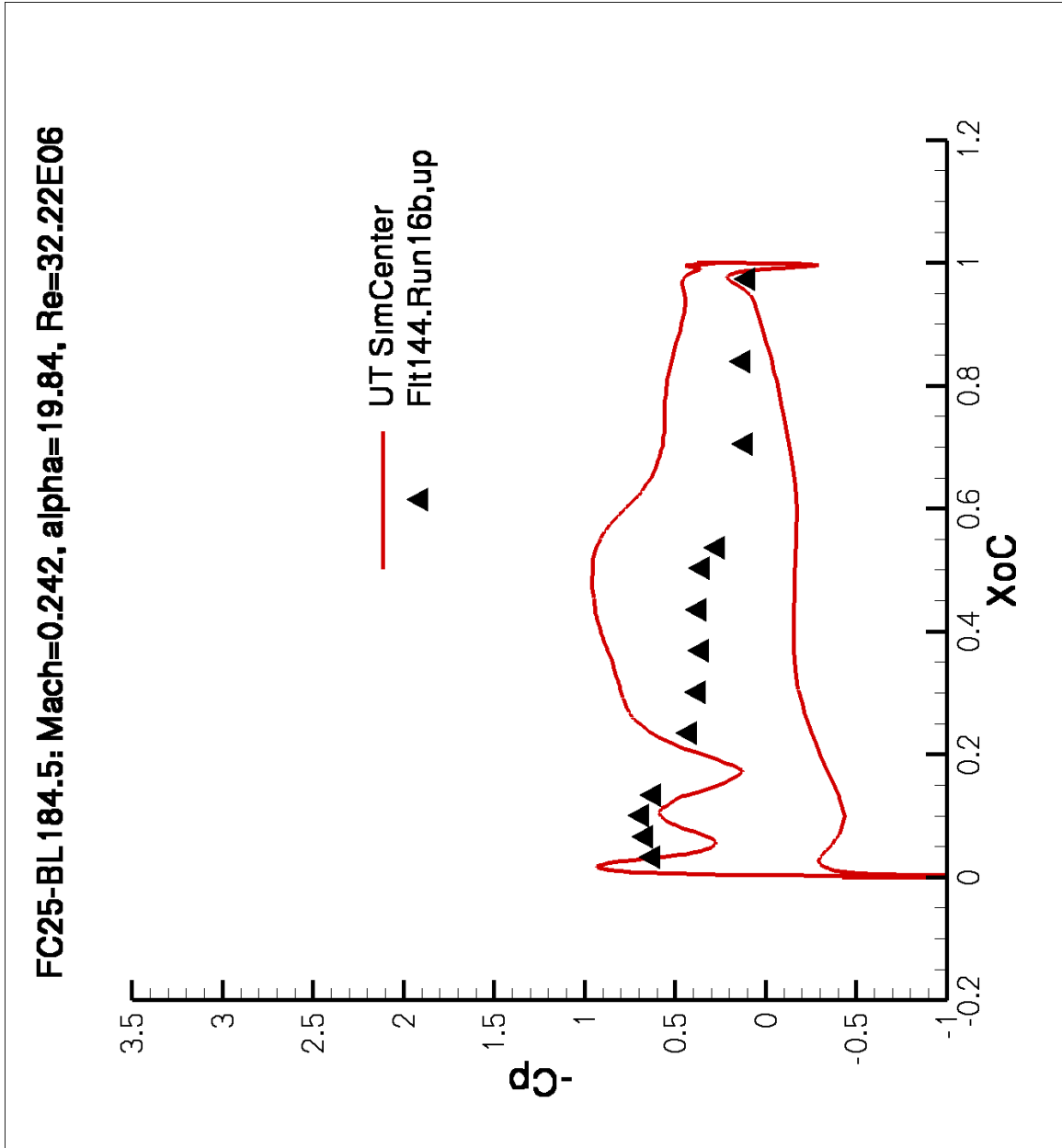


Figure 56: Comparison of Cp along FS300 for Flight Case 25.

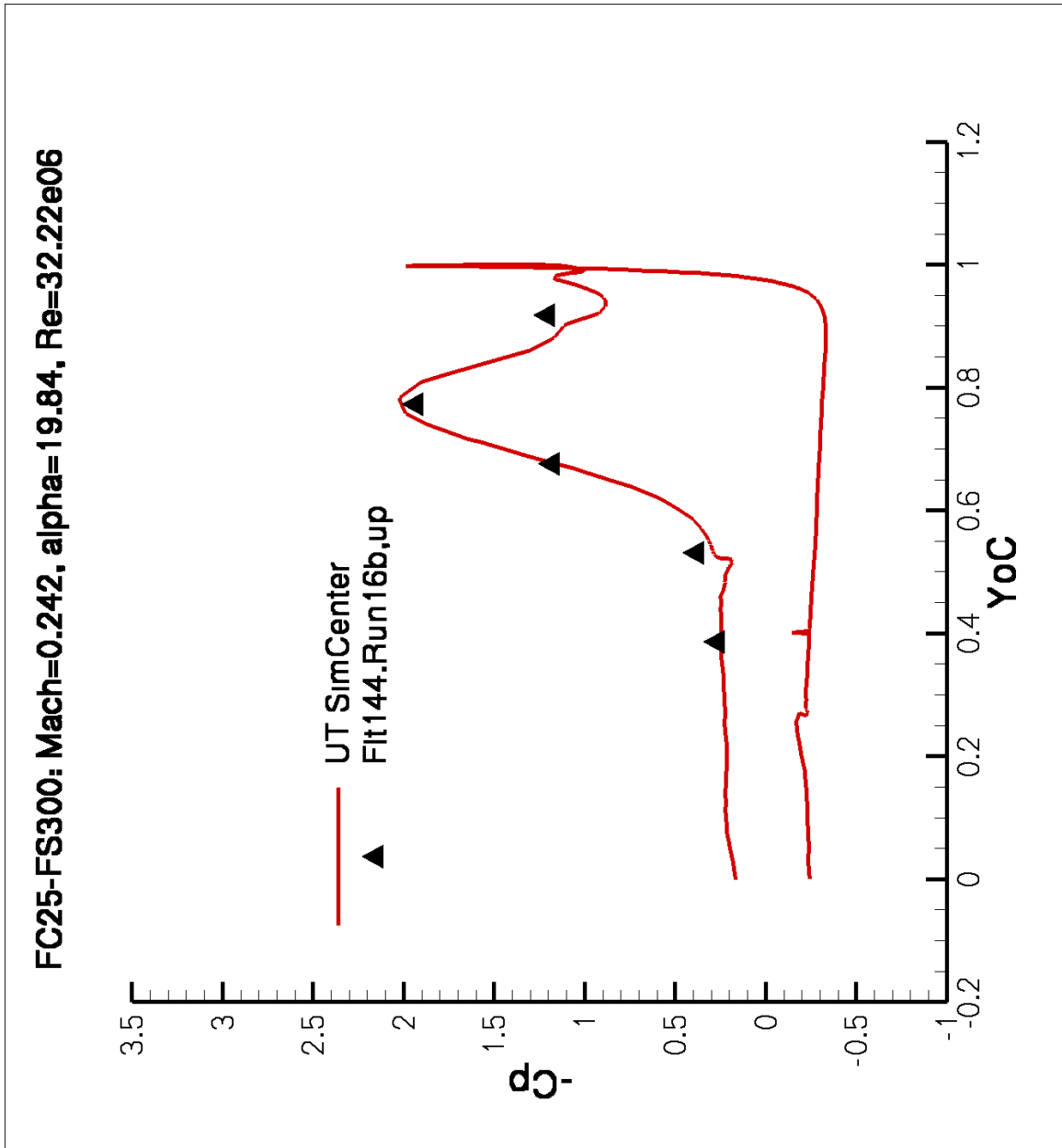


Figure 57: Comparison of Cp along FS337.5 for Flight Case 25.

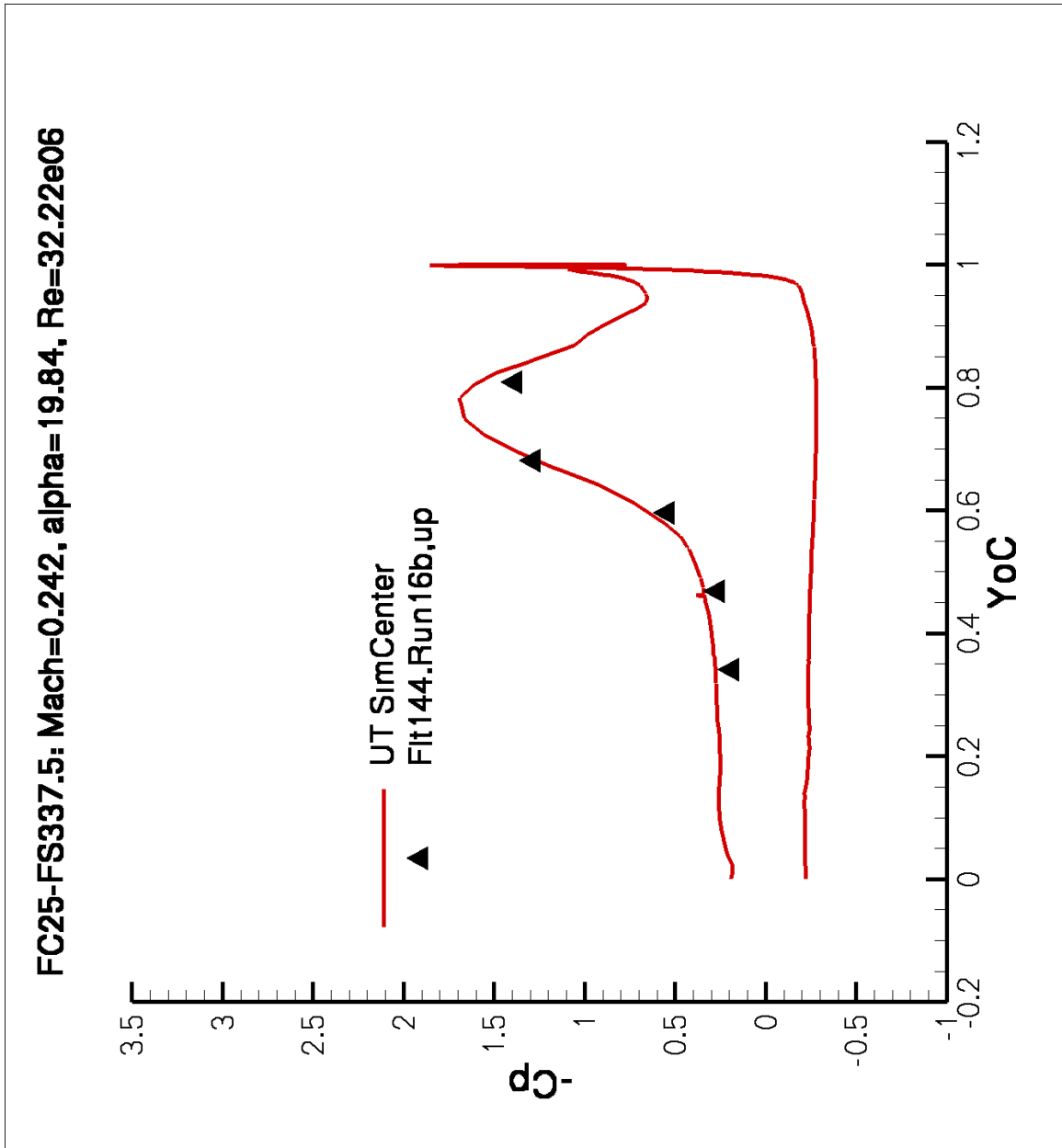


Figure 58: Comparison of Cp along FS375 for Flight Case 25.

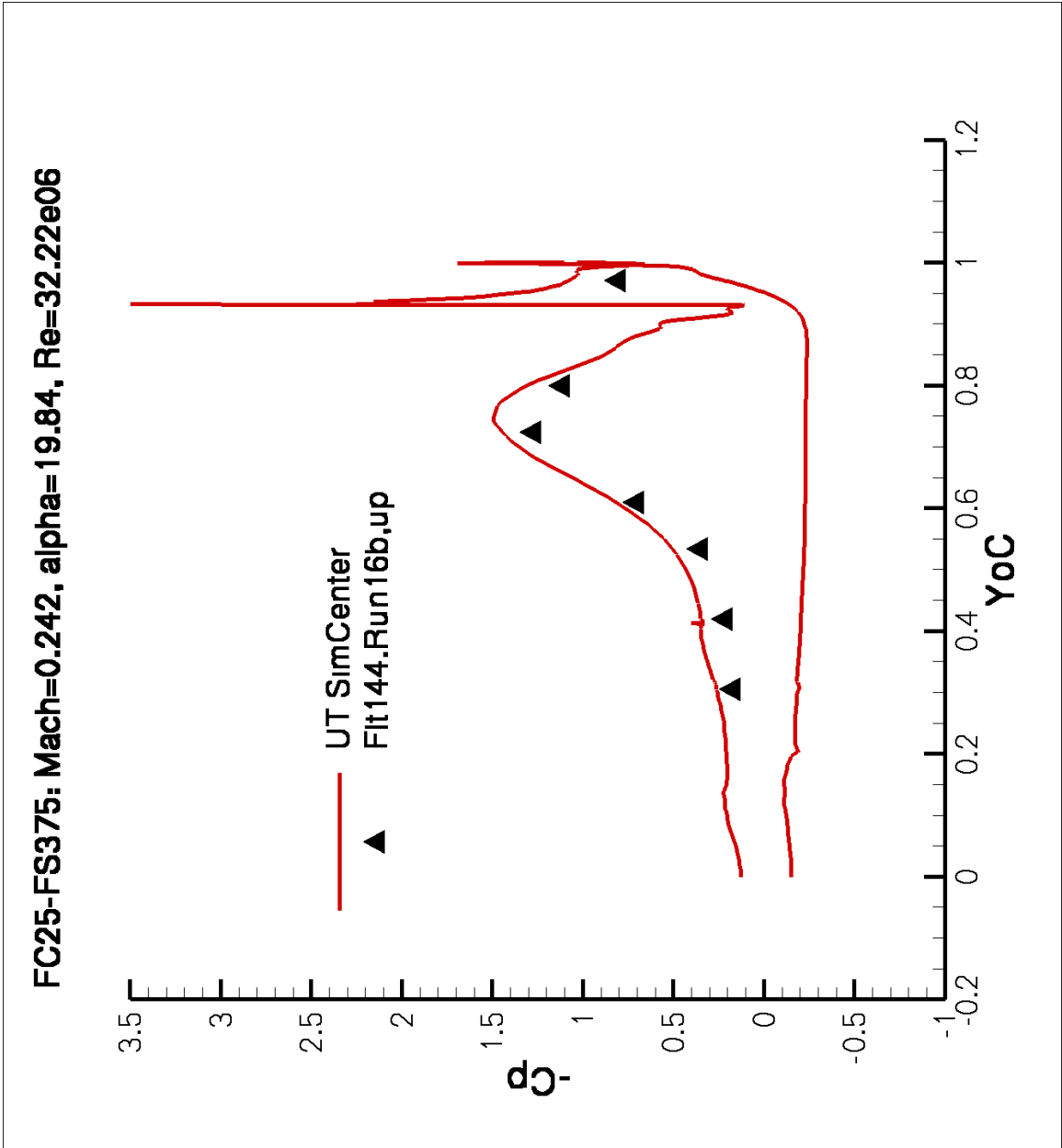


Figure 59: Comparison of Cp along FS407.5 for Flight Case 25.

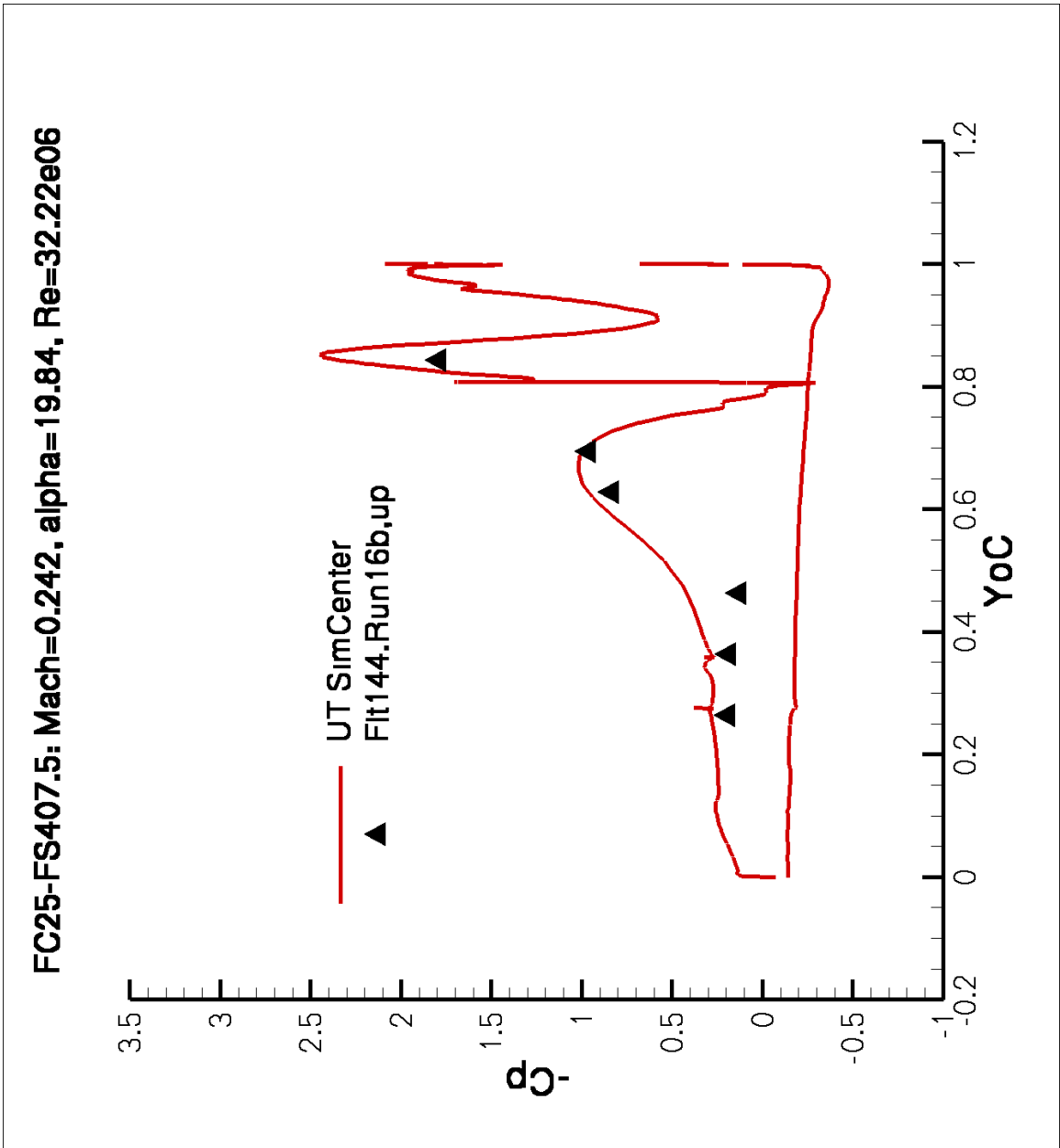


Figure 60: Comparison of C_p along FS450 for Flight Case 25.

FC25-FS450: Mach=0.242, alpha=19.84, Re=32.22e06

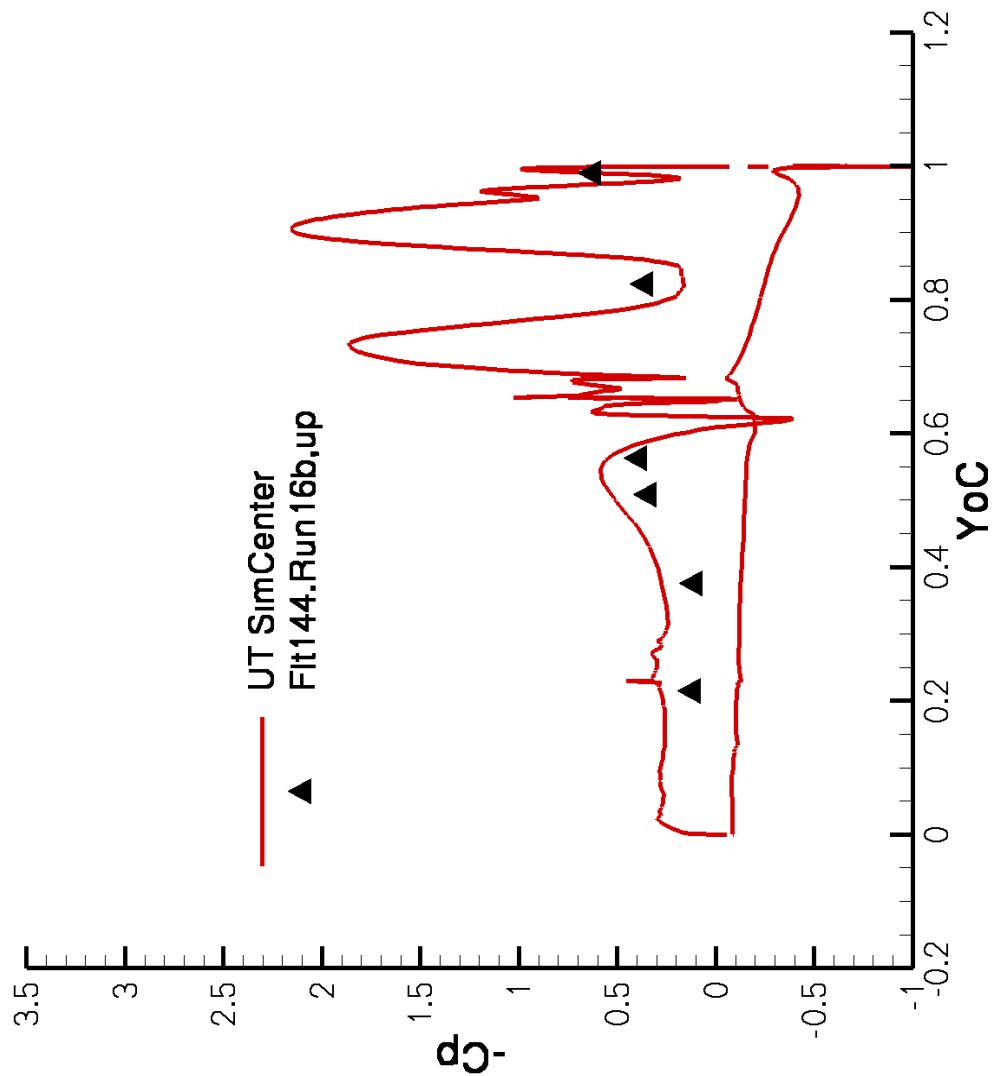


Figure 61: Comparison of Cp along BL55 for Flight Case 70.

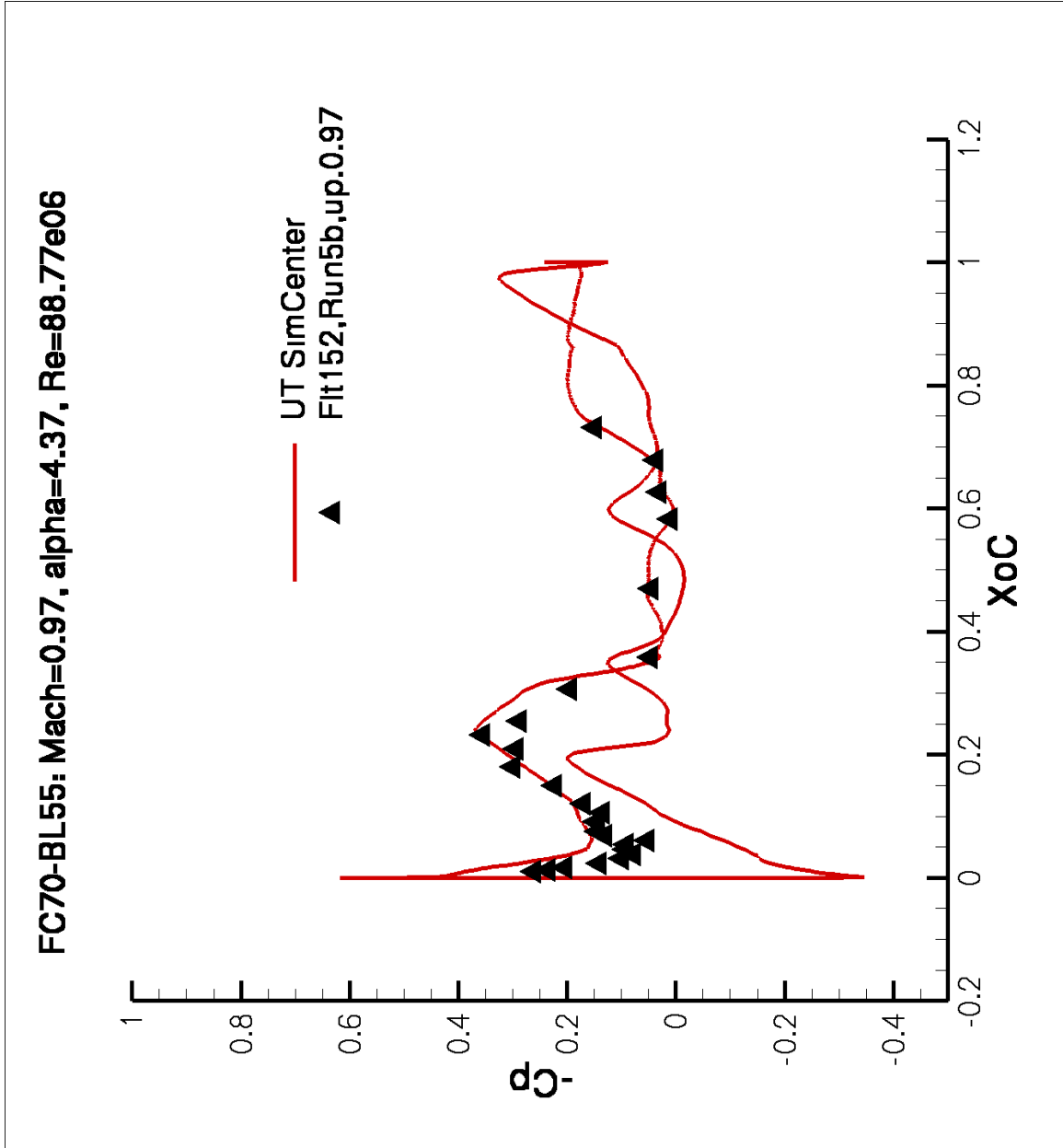


Figure 62: Comparison of Cp along BL70 for Flight Case 70.

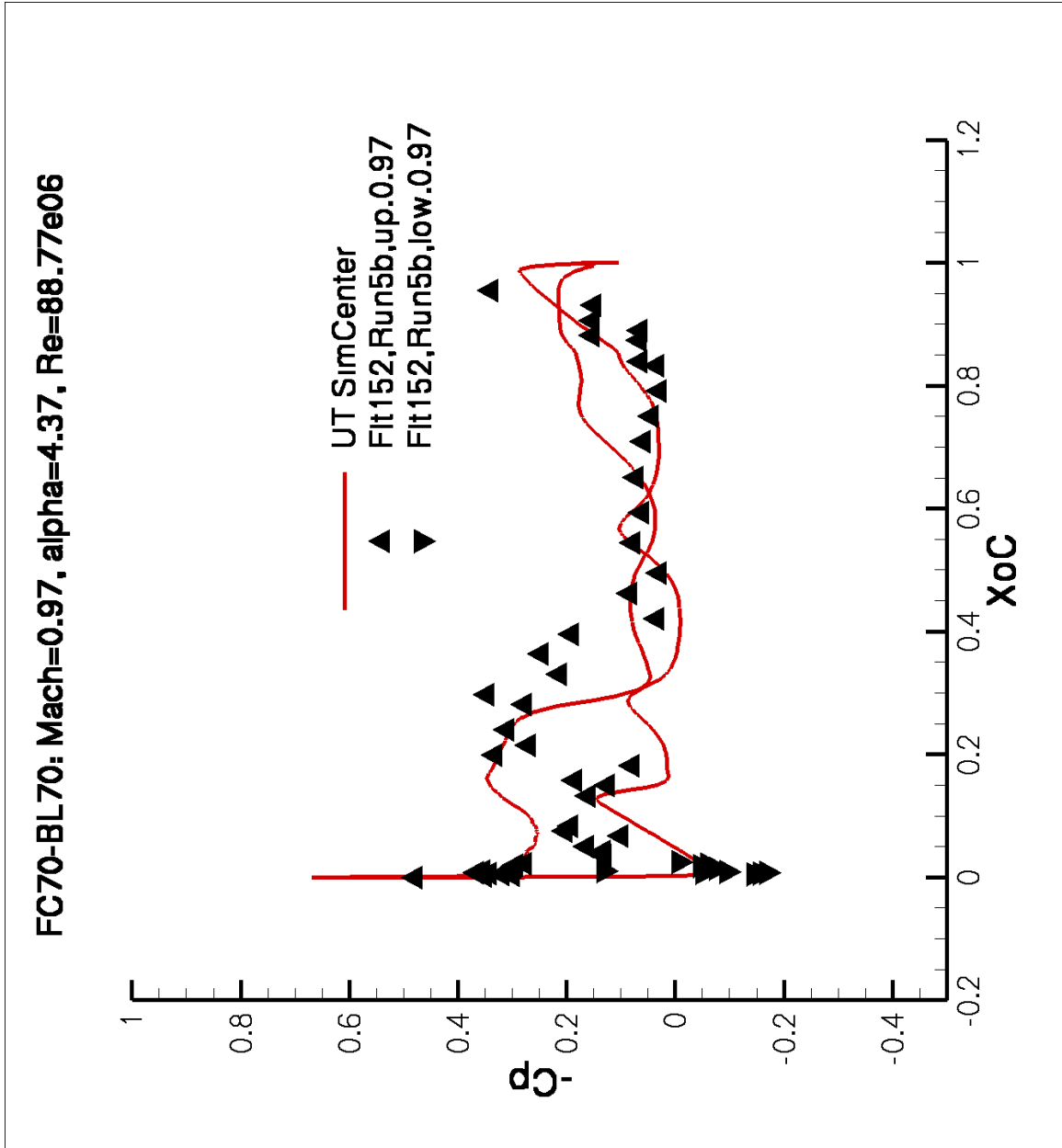


Figure 63: Comparison of Cp along BL80 for Flight Case 70.

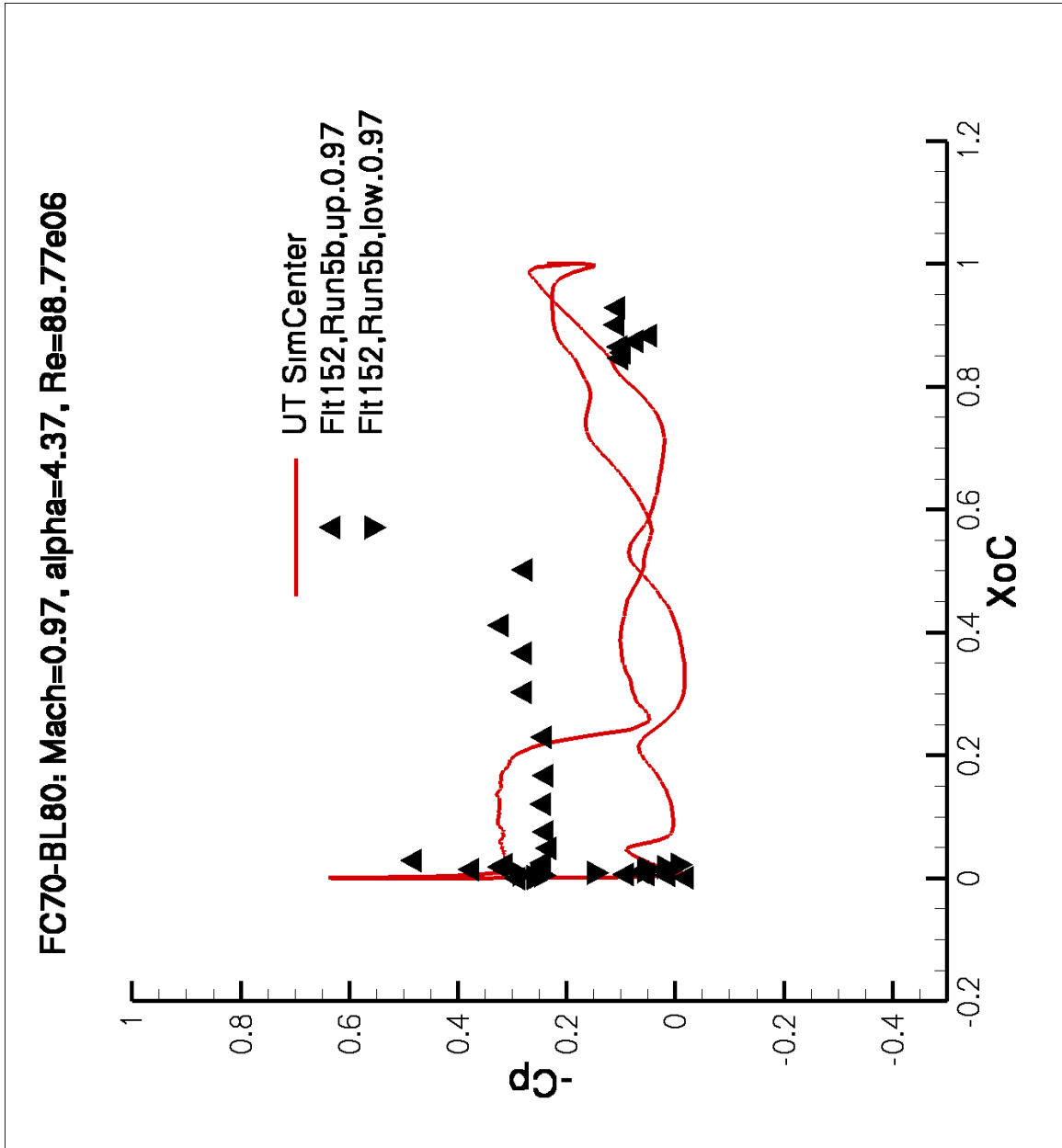


Figure 64: Comparison of Cp along BL95 for Flight Case 70.

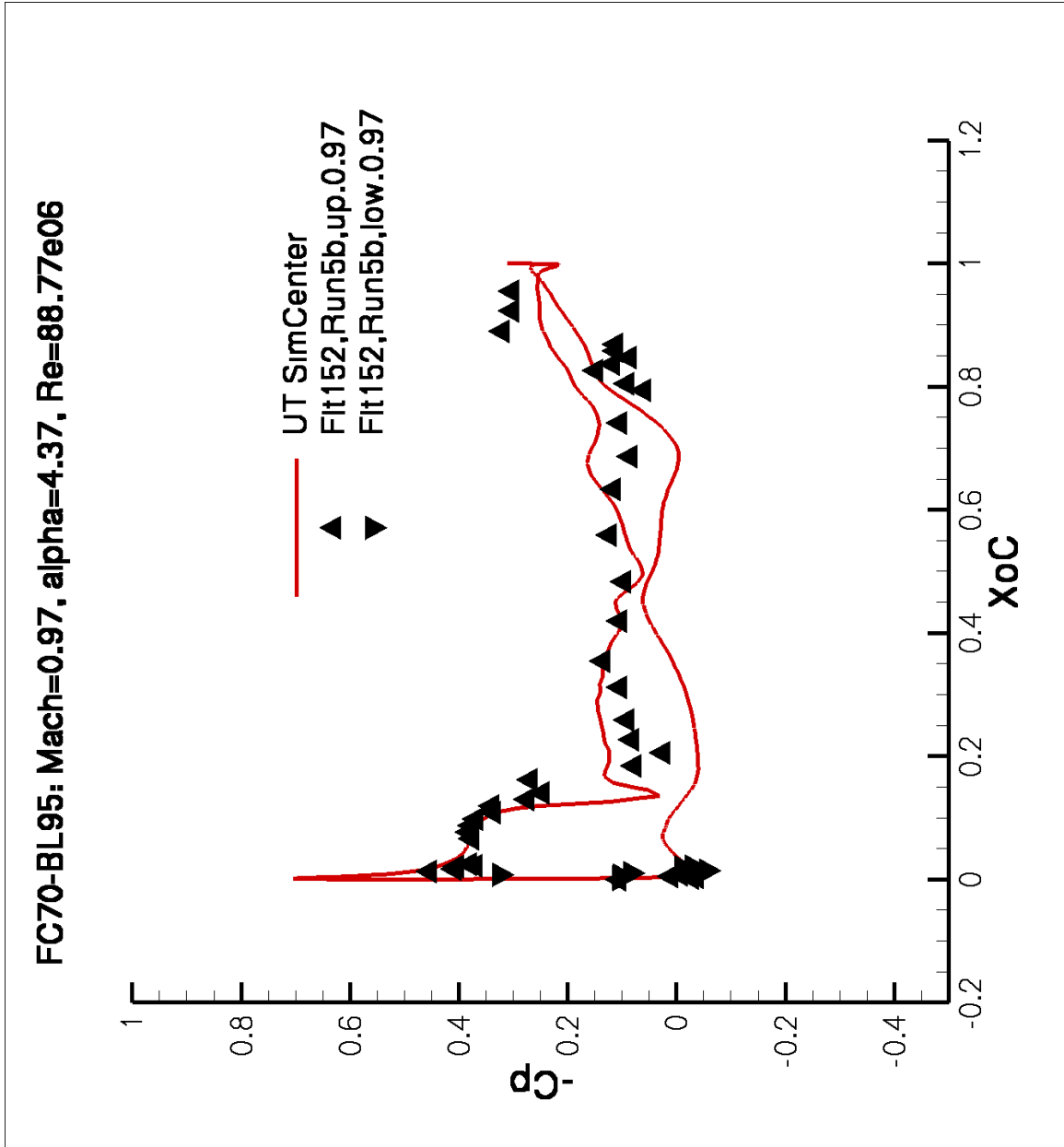


Figure 65: Comparison of Cp along BL153.5 for Flight Case 70.

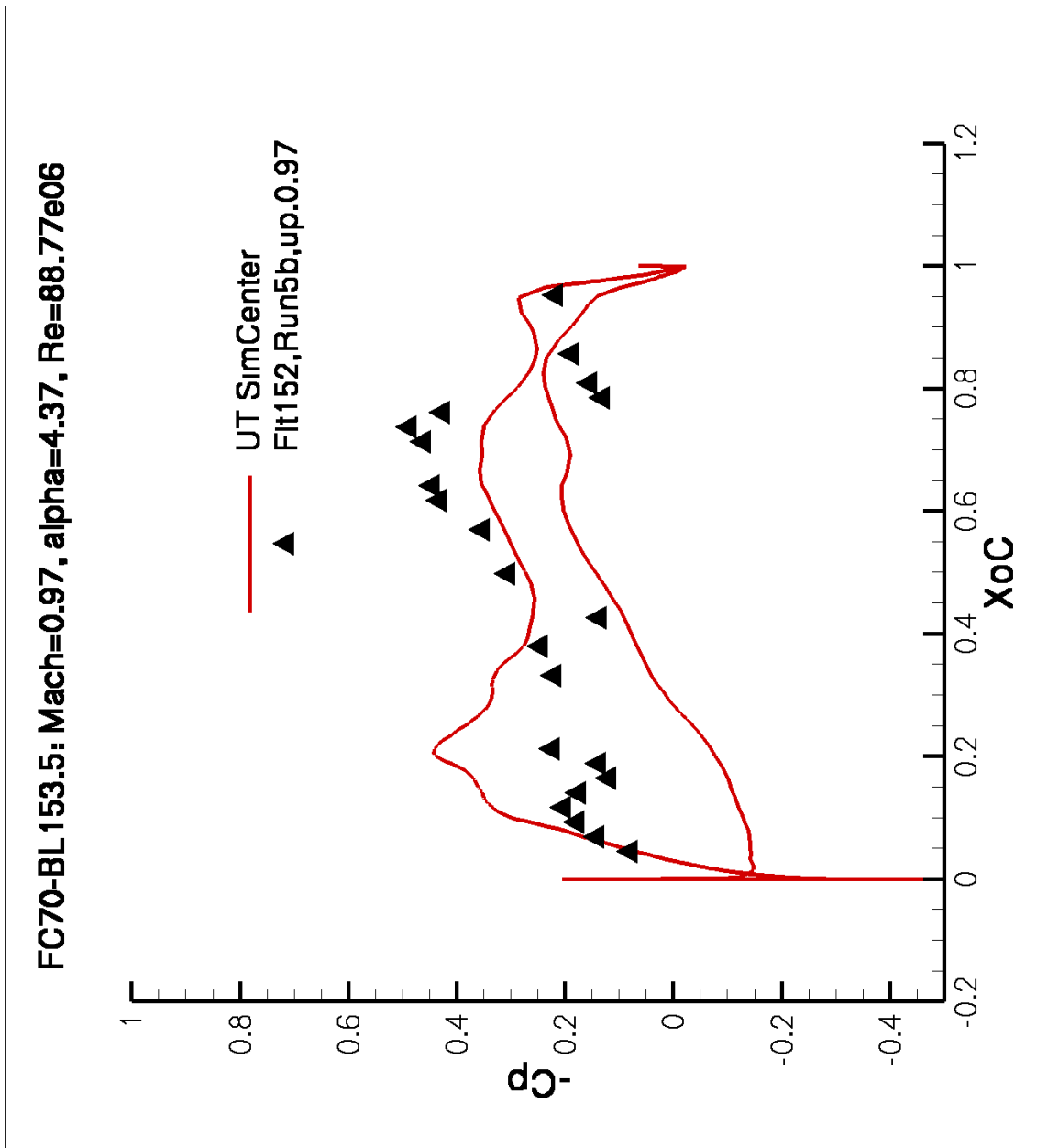


Figure 66: Comparison of Cp along BL184.5 for Flight Case 70.

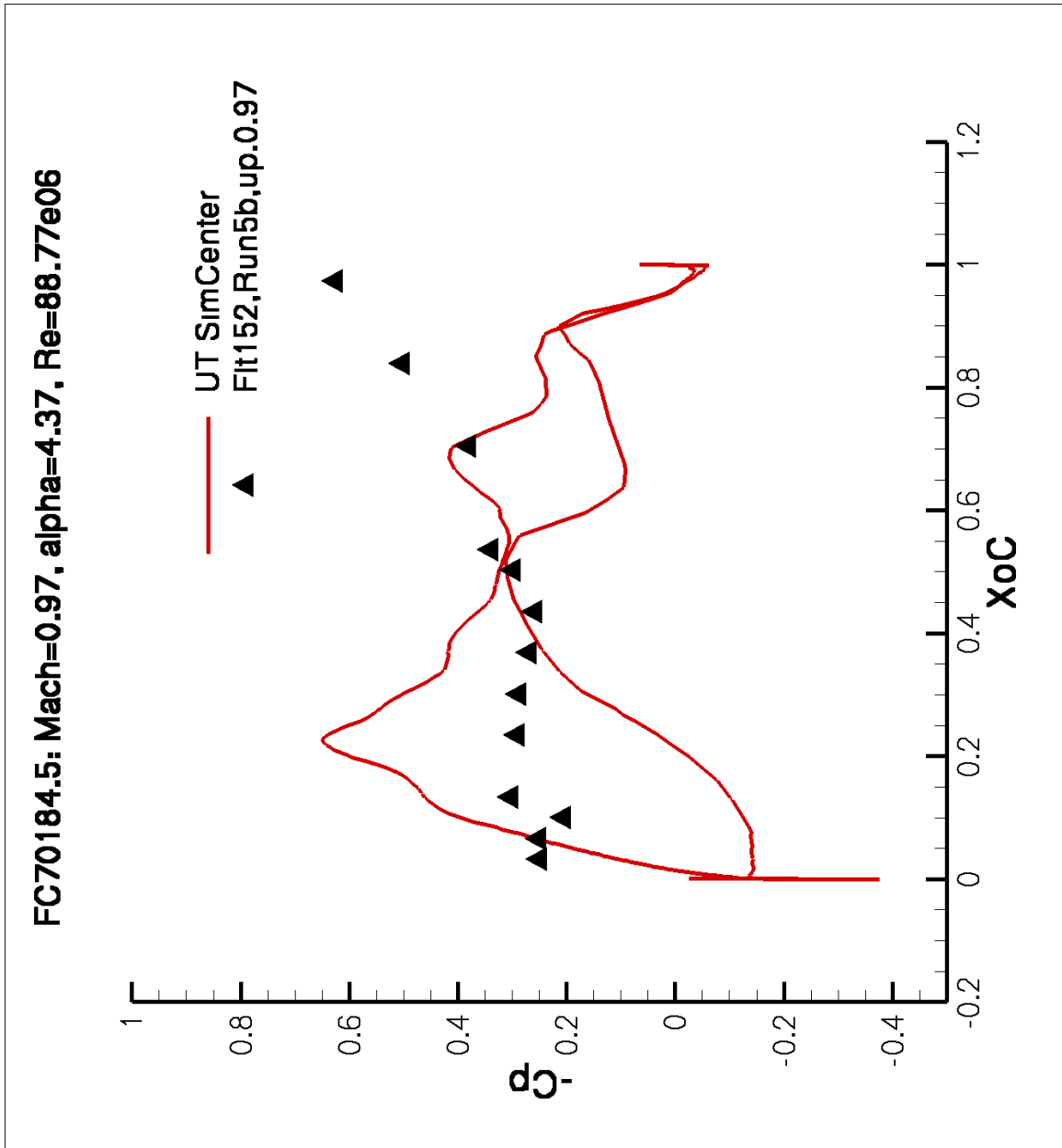


Figure 67: Comparison of Cp along FS300 for Flight Case 70.

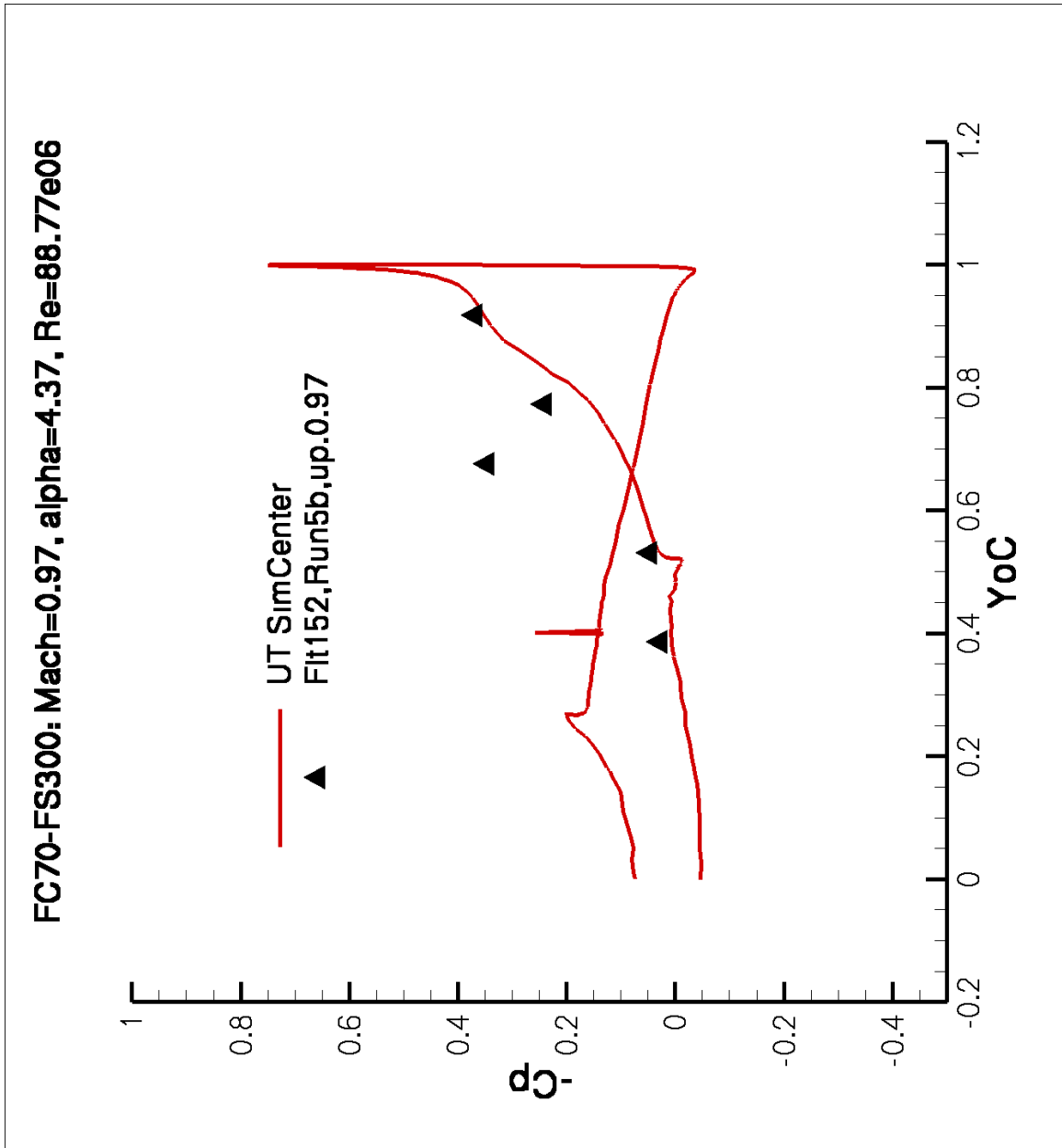


Figure 68: Comparison of C_p along FS337.5 for Flight Case 70.

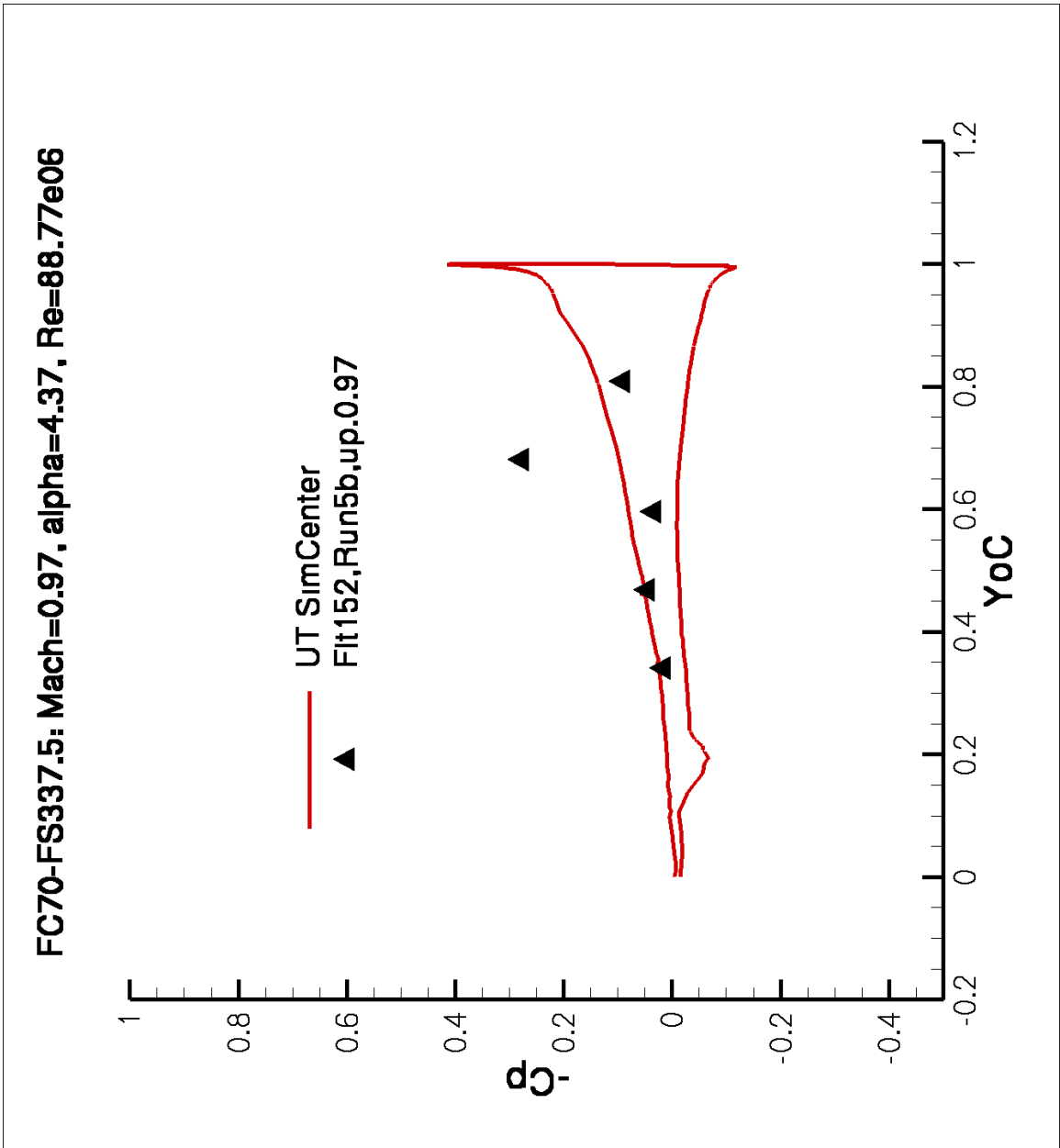


Figure 69: Comparison of Cp along FS375 for Flight Case 70.

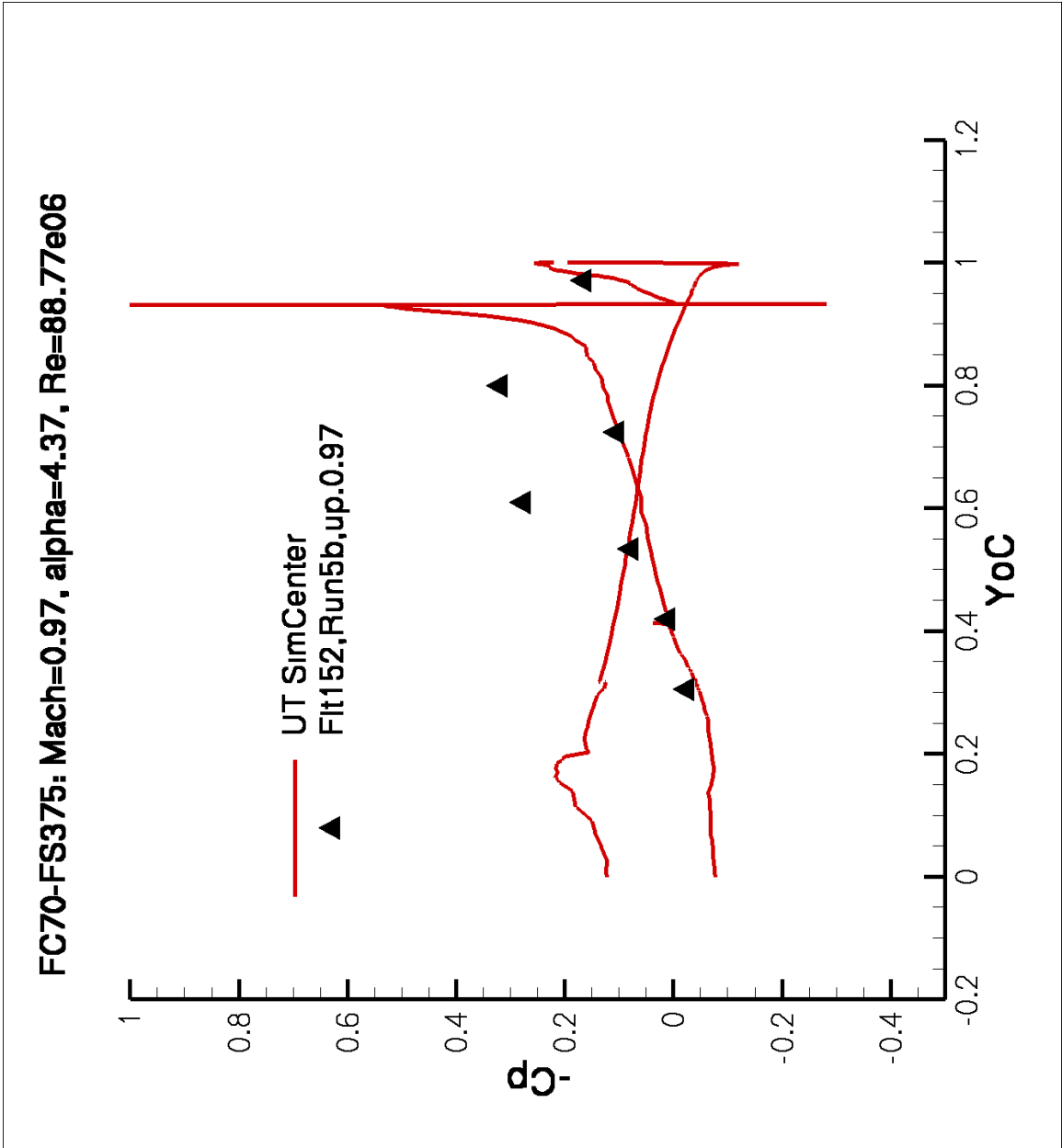


Figure 70: Comparison of C_p along FS407.5 for Flight Case 70.

FC70-FS407.5: Mach=0.97, alpha=4.37, Re=88.77e06

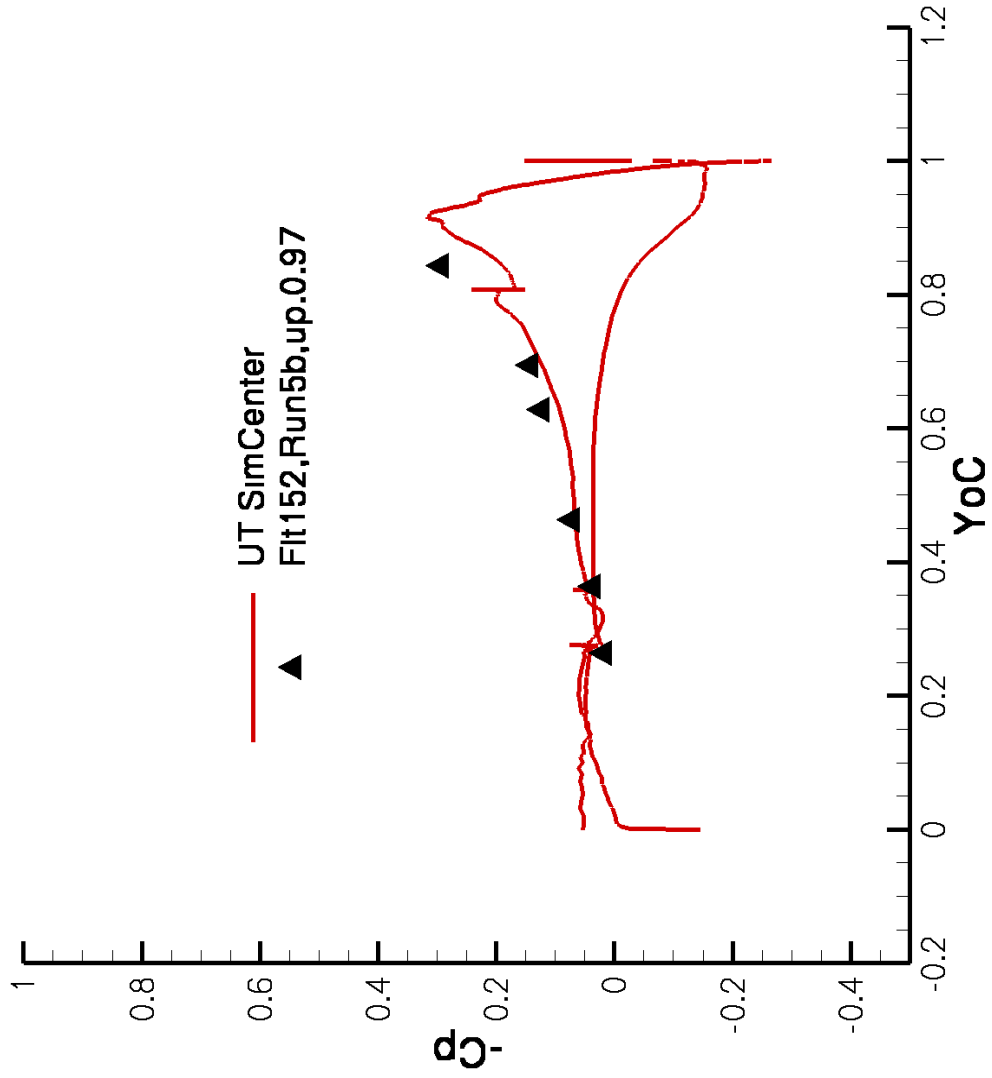


Figure 71: Comparison of C_p along FS450 for Flight Case 70.

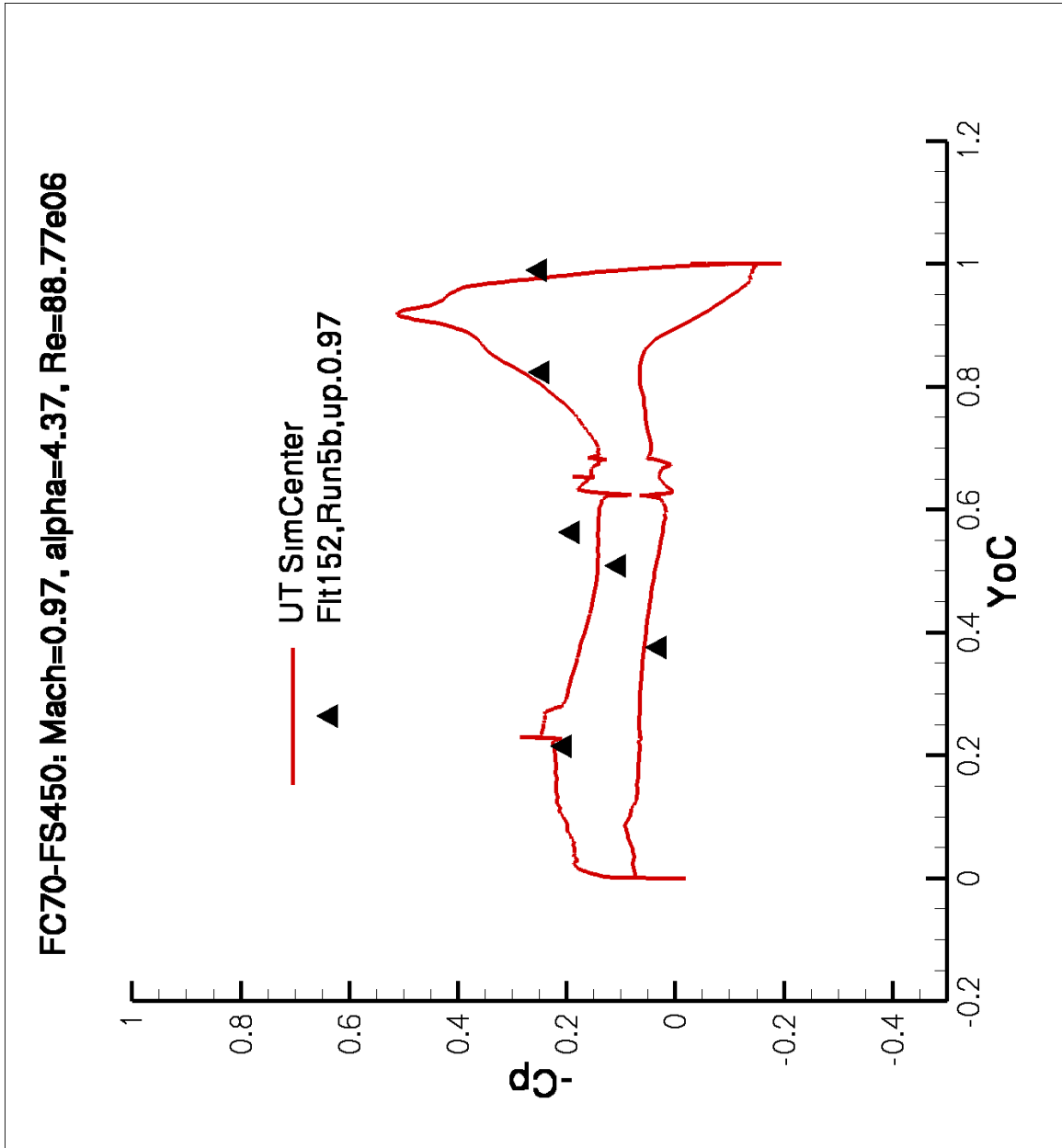


Figure 72: Visualization of Surface C_p for Flight Case O7.

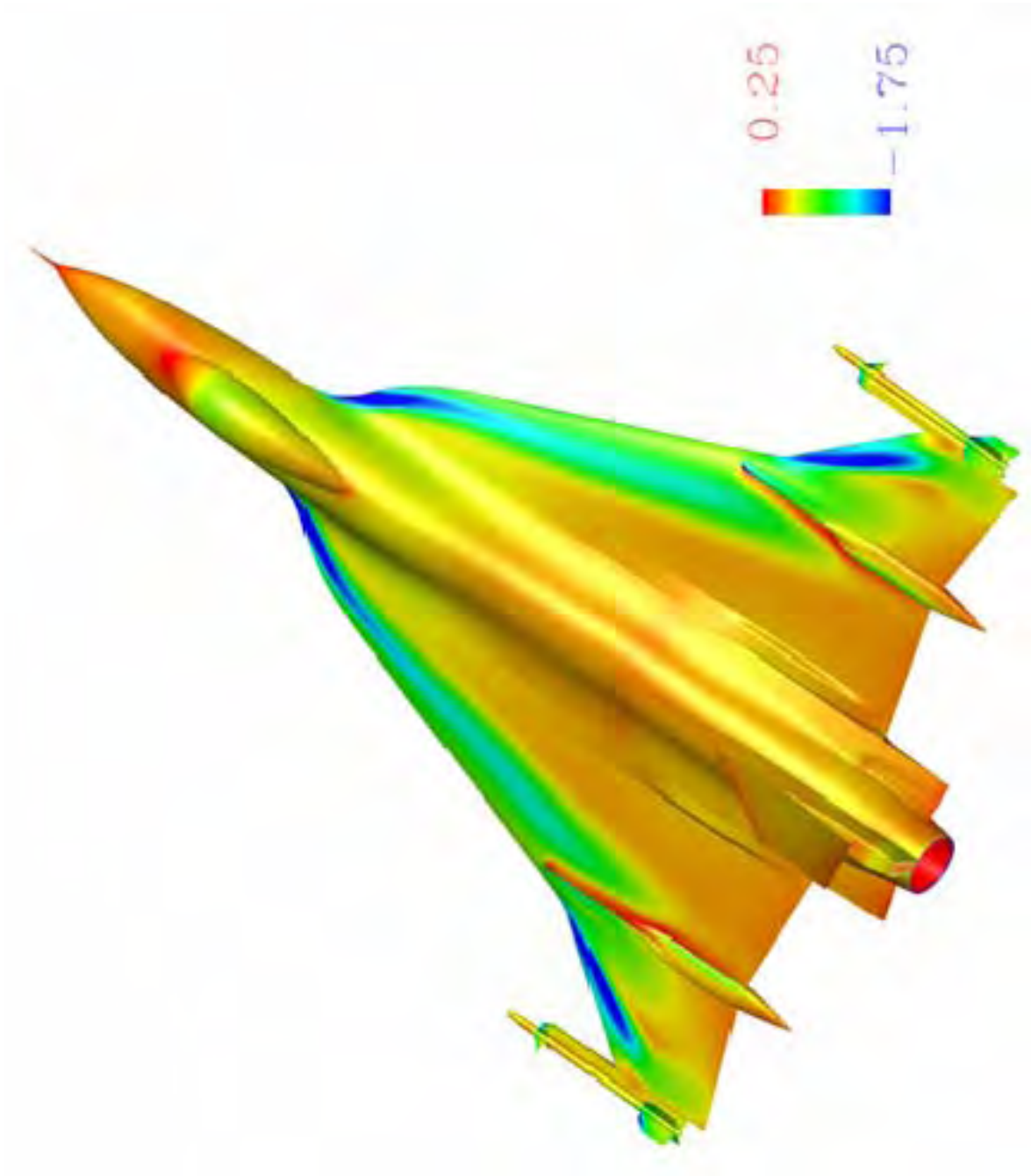


Figure 73: Visualization of Surface C_p for Flight Case 25.

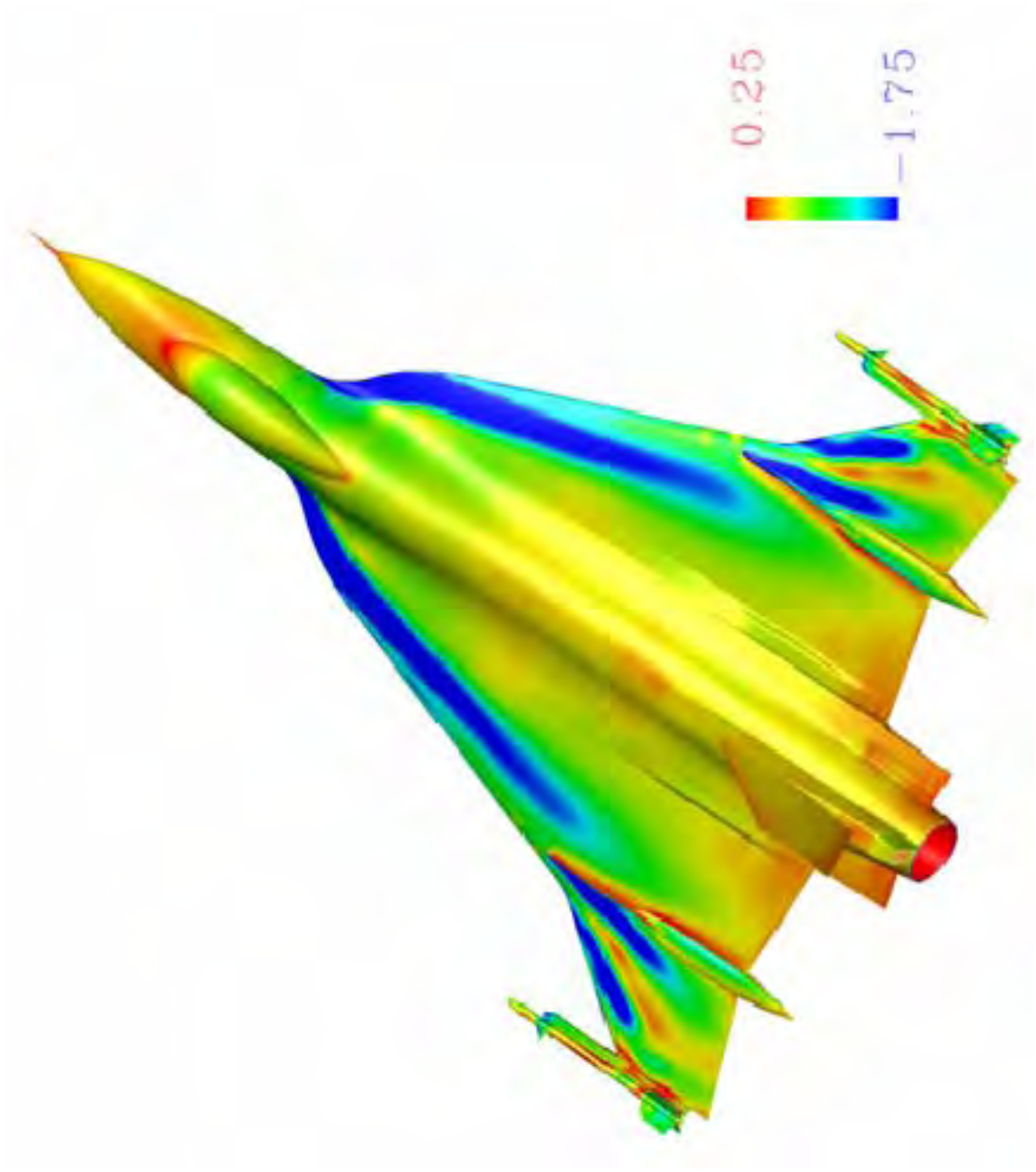


Figure 74: Visualization of Surface Cp for Flight Case 70.

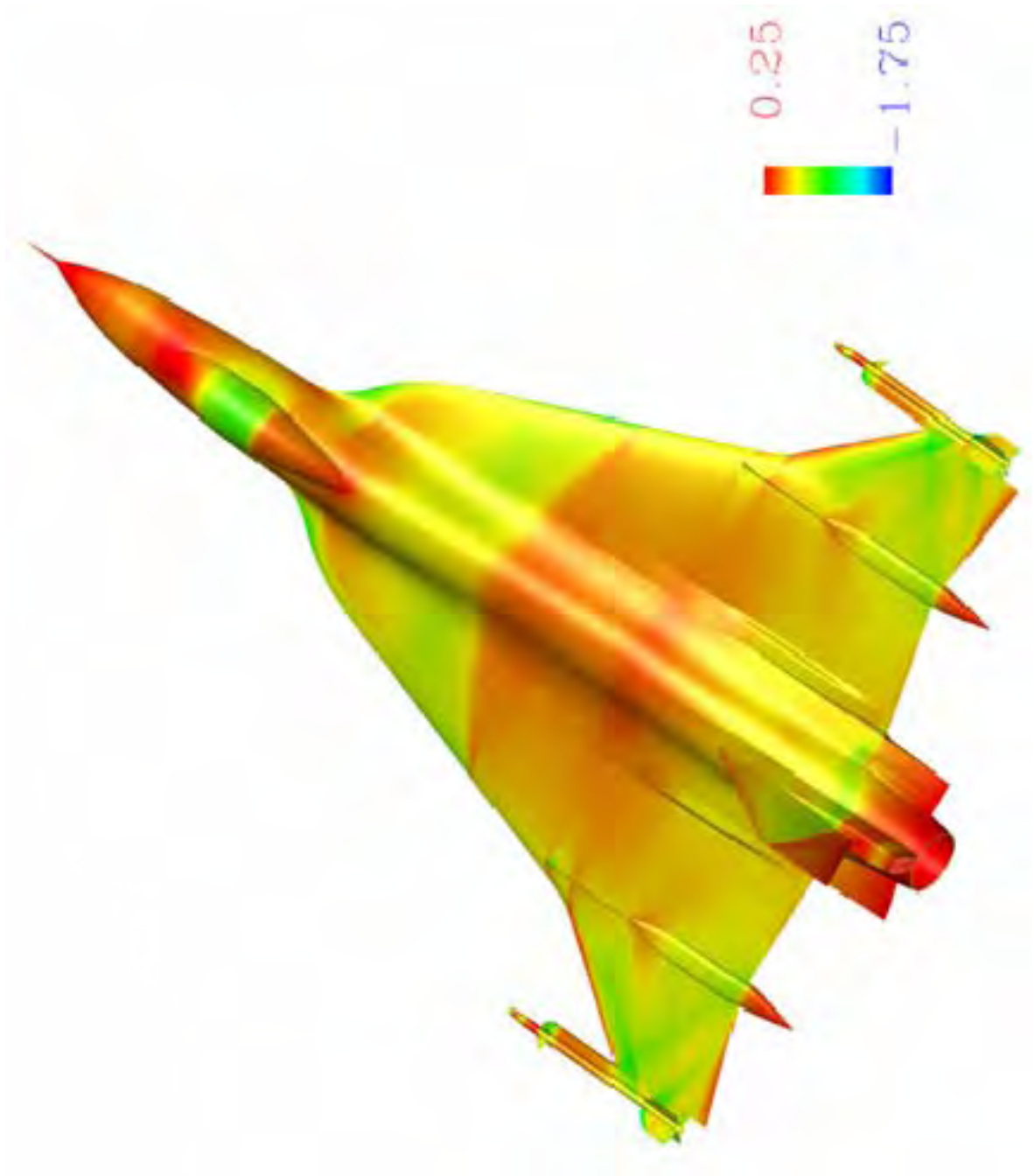


Figure 75: Vorticity Magnitude at Constant Spanwise Cuts for Flight Case O7.

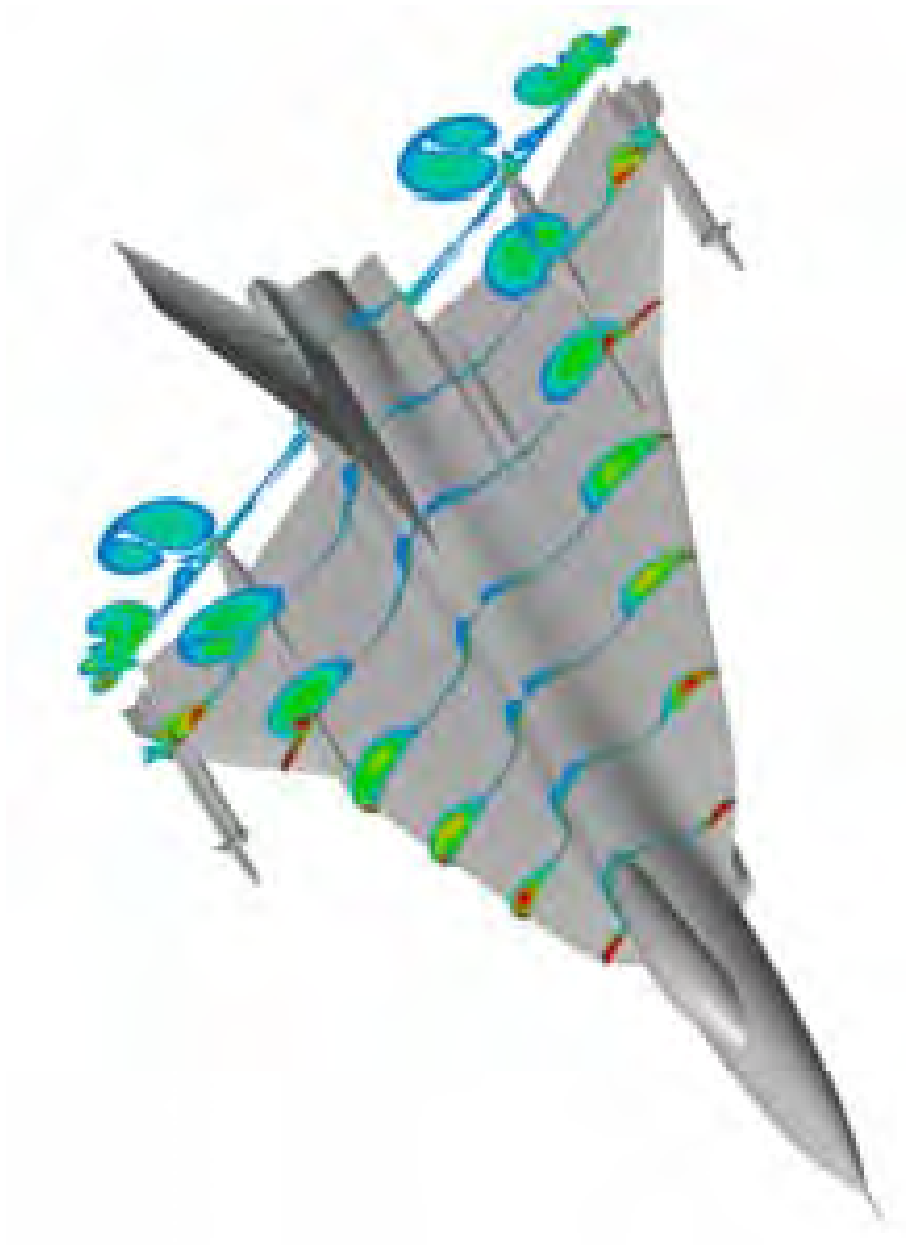


Figure 76: Vorticity Magnitude at Constant Spanwise Cuts for Flight Case 25.

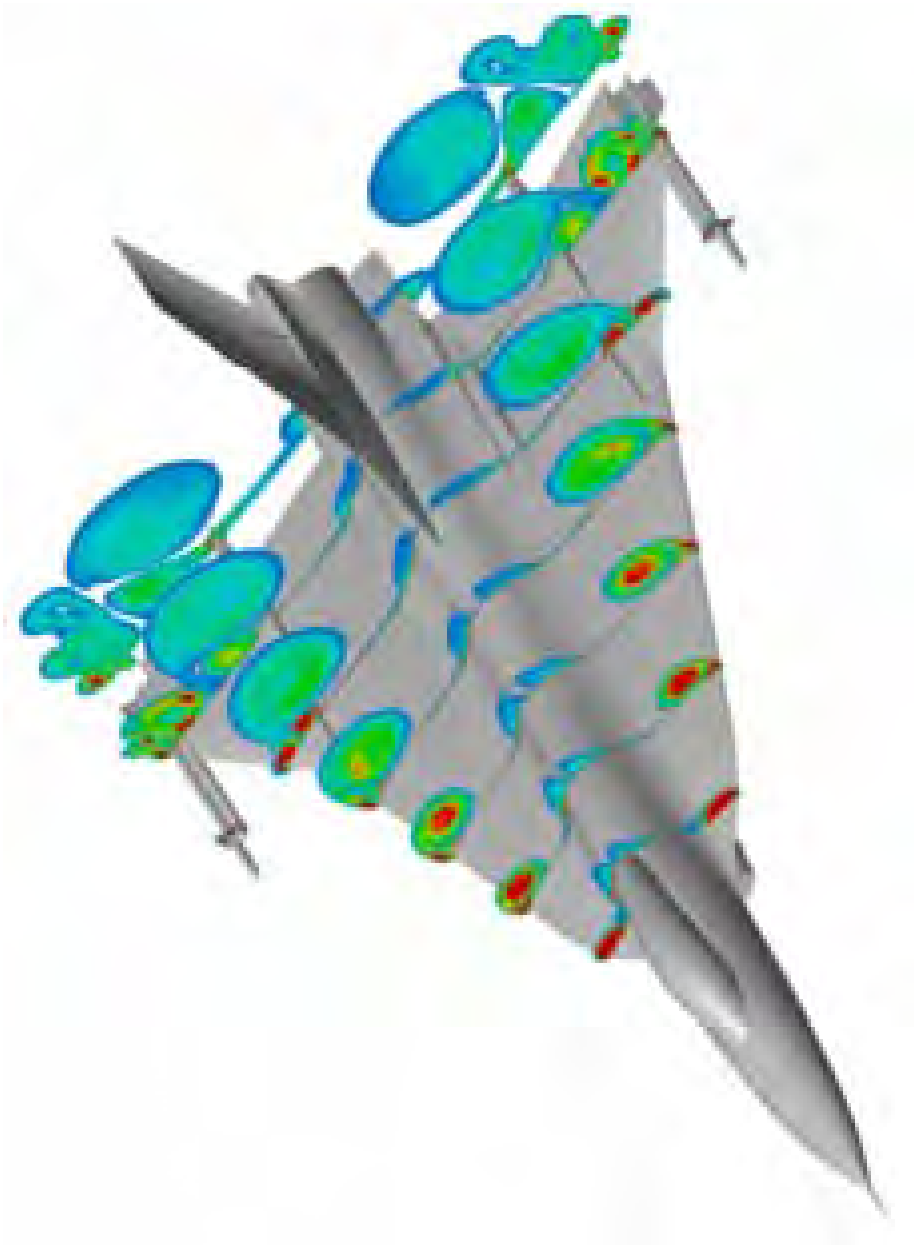


Figure 77: Location of Shock Formation for Flight Case.

